New Optical Sensor Suite
for
Ultrahigh Temperature Fossil Fuel Applications

Topical Report

DOE Award Number: DE-FC26-03NT41922

Reporting Start Date: 1 April 2004

Reporting Period End Date: 30 November 2004

Principal Authors: Russell G. May (Prime Research, LC)
Tony Peng (Prime Research, LC)
Tom Flynn (Babcock & Wilcox Research Center)

Date Report Issued: December 2004

Submitting Organization: Prime Research, LC
1750 Kraft Dr Ste 1000
Blacksburg, VA 24060

Babcock & Wilcox Research Center
1562 Beeson Street
Alliance, OH 44601-2196

DISCLAIMER

This report was prepared as an account of work sponsored by an agency of the United States Government. Neither the United States Government nor in the agency thereof, nor any of their employees, makes any warranty, express or implied, or assumes any legal liability or responsibility for the accuracy, completeness, or usefulness of the information, apparatus, product, or process disclosed, or represents that its use would not infringe privately owned rights. Reference herein to any specific commercial product, process, or service by trade name, trademark, manufacturer, or otherwise does not necessarily constitute or imply its endorsement, recommendation, or favoring by the United States Government were in the agency thereof. The views lists opinions of authors expressed herein do not necessarily state or reflect those of United States Government or any agency thereof.

ABSTRACT

Accomplishments during the Phase I of a program to develop and demonstrate technology for the instrumentation of advanced powerplants are described. Engineers from Prime Research, LC and Babcock and Wilcox Research Center collaborated to generate a list of potential applications for robust photonic sensors in existing and future boiler plants. From that list, three applications were identified as primary candidates for initial development and demonstration of high-temperature sensors in an ultrasupercritical power plant. A matrix of potential fiber optic sensor approaches was derived, and a data set of specifications for high-temperature optical fiber was produced. Several fiber optic sensor configurations, including interferometric (extrinsic and intrinsic Fabry-Perot interferometer), gratings (fiber Bragg gratings and long period gratings), and microbend sensors, were evaluated in the laboratory.

In addition, progress was made in the development of materials and methods to apply high-temperature optical claddings to sapphire fibers, in order to improve their optical waveguiding properties so that they can be used in the design and fabrication of high-temperature sensors. Through refinements in the processing steps, the quality of the interface between core and cladding of the fibers was improved, which is expected to reduce scattering and attenuation in the fibers. Numerical aperture measurements of both clad and unclad sapphire fibers were obtained and used to estimate the reduction in mode volume afforded by the cladding.

High-temperature sensors based on sapphire fibers were also investigated. The fabrication of an intrinsic Fabry-Perot cavity within sapphire fibers was attempted by the bulk diffusion of magnesium oxide into short localized segments of longer sapphire fibers. Fourier analysis of the fringes that resulted when the treated fiber was interrogated by a swept laser spectrometer suggested that an intrinsic cavity had been formed in the fiber. Also, an unclad sapphire fiber was tested as a temperature sensor at moderate temperatures (up to 775° C).

TABLE OF CONTENTS

1 INTRODUCTION

The goal of this project is the research and development of advanced, robust photonic sensors based on improved sapphire optical waveguides, and the identification and demonstration of applications of the new sensors in advanced fossil fuel powerplants, where the new technology will realize improvements in process control and monitoring. The advantages of fiber optic sensors over electronic sensors, particularly in environments where the electronic sensing materials can not withstand the rigors of the harsh conditions, are well known. Typically, advanced power generation systems operate at higher temperatures and pressures than traditional power plants. Traditional sensor technology for measuring temperature, pressure, flow and strain will not survive the harsh conditions anticipated in these plants. Furthermore, these plants will require more extensive process monitoring and condition assessment to maintain optimum performance and minimize maintenance costs. An effective means is required to reduce the complexity and cost of connecting the larger number of sensors to a central data acquisition platform. Therefore, one of the goals of the program is the identification of all potential applications in supercritical boiler plans where photonic sensors can be used for process control and monitoring.

For the ultrahigh-temperature environment found in current and future power generation facilities, new materials for the optical sensors will be required. Previous efforts to utilize sapphire fiber sensors that can theoretically operate above 1650° C (3000° F) have been limited because the fiber itself does not lend itself to incorporation in the known sensor techniques, due to its unclad and multimode construction. Another goal of this program is the development of high-temperature, ceramic claddings for sapphire fibers to improve the waveguiding properties of sapphire fibers and facilitate their use in photonic sensor systems.

Current efforts towards improvement of sapphire fibers focus on creating cladding in sapphire (aluminum oxide single crystal, Al_2O_3) fibers by dip-coating the fibers in a a mixture of magnesium oxide (MgO) powders and magnesium aluminate spinel ($MgAl_2O_4$) powders to form a coating on the sapphire fibers. The technique involves dip coating a sapphire fiber in a suspension of MgO and spinel powders, drying the coating, then firing at elevated temperature to react the MgO powder with the sapphire fiber and to densify the coating. The overall reaction for the process is given by the chemical equation:

$$MgO + Al_2O_3 = MgAl_2O_4$$

which proceeds rapidly at 1750°C (3182° F).

The coated fibers are then fired at high temperatures to facilitate the reaction between the MgO in the coating and the Al_2O_3 in the fibers by ion diffusion, and create a cladding consisting of $MgAl_2O_4$ surrounding the sapphire core. As a result, the diameters of the sapphire fibers are reduced and the number of modes propagating in the sapphire fibers is also reduced.

2 EXECUTIVE SUMMARY

The overall goal for this project is to explore the potential of optical sensors based on modified sapphire fibers for use and advanced fossil fuel power generation systems. Specific program objectives include (1) development of methods to produce high-temperature optical cladding for sapphire fibers to improve their waveguide properties and enable new classes of high temperature sensors; (2) development of new techniques to produce sensor elements within sapphire fibers, including fiber Bragg gratings and/or intrinsic Fabry-Perot interferometers; and (3) demonstration of new, ultrahigh-temperature optical sensors for specific measurements required for advanced powerplant control systems, as identified by powerplant manufacturers/integrators/operators.

The project is organized into two consecutive phases. This report documents the accomplishments during Phase I. The objectives for this phase included (1) identification of all potential sites within the existing/near-term boiler designs and future supercritical boiler designs where novel optical sensors could be used for process monitoring and condition assessment; (2) evaluation of optical sensor designs which successfully address the applications requirements; and (3) extensions of the state-of-the-art in fabrication and processing of custom single-mode and multimode sapphire fiber sensors, specifically focused on the development of new techniques to produce cladding on sapphire waveguides.

Objectives for the next phase include (1) development of a suite of optimized sensor designs for the targeted applications and testing; and (2) demonstration of the feasibility and performance of the sensors for both laboratory in full scale testing such that they are easily integrated into powerplant control systems.

This report emphasizes accomplishments during the last half of the Phase I effort. Discussions of the accomplishments obtained in the first half of the Phase I program may be found in the 1st Semiannual Technical Report for the program.

Under a subcontract to Prime Research, Babcock & Wilcox Research Center convened a team of engineers to consider possible applications of photonic sensors in existing and future boiler plants. In addition, a meeting was held at Alliance, OH between representatives of B&W and Prime Research to discuss the results of the B&W study, and to brainstorm other possible applications where robust sensors could be used to good advantage for controlling or monitoring power plants. Issues that were identified as potential barriers to increased use of instrumentation in advanced plants include limited availability of suitable materials for typical conditions (which include corrosion, corrosion, and reducing atmospheres), very high temperatures due to oxygen firing, need for improved models, difficulty in interfacing with existing control systems, and resistance of customers to pay for sensors and controls.

Four classes of measurements within supercritical boiler plants were identified as desirable for monitoring and controlling the plants. These include temperature measurement for thermal barrier coatings, in-situ strain measurements on superheater

tubes, measurement of steam flow in membrane walls and tube banks, and dynamic pressure measurements for monitoring of combustion dynamics. Three specific locations were identified as primary candidates for sensor development in this program: the furnace water wall, secondary superheater tubes, and burners. Required sensor measurands for these locations include temperature, pressure, and strain.

Babcock & Wilcox also investigated requirements for interface of fiber optic sensors to power plant control systems. Two applications were considered: sensors as input to the plant's distributed control system, and as input to data archiving systems for trending studies and analysis. Specific interface requirements for both of these applications were derived including signal format (0-10V, 4-20mA, etc.), update rates, communications protocols, and platform architecture.

Based on the input from Babcock & Wilcox, a matrix of potential sensing techniques and requirements for high-temperature fiber and cladding were developed.

Tests were performed to evaluate the performance of three sensor classes: interferometric (extrinsic and intrinsic Fabry-Perot interferometer), gratings (fiber Bragg gratings and long period gratings), and microbend sensors. The sensors were configured as temperature or pressure sensors, as appropriate for the sensor method. The sensor performance was characterized in terms of sensor resolution.

Although some success has been achieved by research groups in the demonstration of multimode sapphire optical sensors, optimal function of several important classes of fiber optic sensors, including fiber Bragg gratings (FBGs) and interferometric sensors, requires the use of single-mode waveguides. While it is possible to minimize the multimode-induced problems by exciting only a small number of modes in the multimode fiber, this approach is successful only with straight, inflexible sapphire rods. Bends, splices and connectors in the fiber (necessities for integration in real-world applications) cause a redistribution of power into a larger number of modes, thereby reducing the practicality of such multimode sensors. This limitation is the motivation for the development of high-temperature claddings in order to reduce the mode volume of the sapphire fiber.

Significant progress was made in the development of materials and methods to produce these high-temperature optical claddings on sapphire fibers. Through refinements in the processing steps, the quality of the interface between core and cladding of the fibers was improved, which is expected to reduce scattering and attenuation in the fibers. Numerical aperture measurements of both clad and unclad sapphire fibers were obtained and used to estimate the reduction in mode volume afforded by the new cladding.

Specific studies and improvements investigated in the development of the cladding material included incorporation of nanopowders into the slurry, improved coating density through particle packing studies, separation of powder milling into dispersion milling and binder milling to prevent agglomeration of powders, testing of several dispersants for control agglomeration, and determination of proper binder burnout temperature.

Modification of sapphire fibers by doping with impurities was investigated, with a goal of creating fiber Bragg gratings or intrinsic Fabry Perot interferometer (IFPI) sensor elements in sapphire fibers. Creation of an IFPI cavity in 125 μm diameter sapphire fiber was attempted by bulk diffusion of magnesium oxide into short (less than 1 mm) segments of sapphire fiber. The intent was to locally reduce the refractive index of the fiber, producing two surfaces defined by the distinct change in refractive index. The Fresnel reflections generated by those surfaces will interfere, and the length of the cavity can be determined from the state of interference. Two configurations were attempted: in the first, a magnesium oxide/alumina coating was applied over a few millimeters at the end of a sapphire fiber. After the sample was heated to diffuse the magnesium oxide (MgO) into the fiber, the end of the sapphire fiber was polished down until the section of fiber with diffused MgO was less than 1 mm in length. In this configuration, the polished end serves as one reflector in the Fabry-Perot cavity; the other is formed by the distinct transition between the doped fiber and the pure fiber. To test the sample, a swept laser spectrometer was used to inject light into the sapphire fiber and analyze the reflected spectra for interference fringes. The complex spectrum that resulted showed evidence of four cavities in the fiber: one was clearly due to the entire length of the sapphire fiber, and one was clearly due to the gap between the sapphire fiber and the spectrometer's silica fiber pigtail. Of the two remaining cavities, one could not be correlated with any features in the sapphire fiber, while the other appeared to be associated with the Fabry-Perot cavity resulting from the diffusion of MgO.

The use of a CO_2 laser for creating IFPI cavities in sapphire fibers was also explored. In this approach, a short segment over a length of sapphire fiber is coated with a magnesium oxide/alumina coating. This coating is not fired in a furnace, but instead, a CO_2 laser is focused on a narrow band of the coating. In this way, only a narrow band of magnesium oxide is diffused into the sapphire fiber, limiting the length of the resulting index modulation in the fiber. Development and tests of this approach are still continuing.

An unclad sapphire fiber was tested as a temperature sensor at moderate temperatures (up to 775° C). The sapphire fiber was clamped on one end, and the other end was positioned in close proximity to the end of a single mode silica fiber, so that a small (< 100μm) gap was formed between the fibers. This silica fiber was interned connected to a swept laser spectrometer, so that the fringes resulting from the gap between fibers could be analyzed to measure the length of the gap. As the sapphire fiber was heated, it expanded, reducing the gap length. From the known coefficients of thermal expansion for sapphire fiber, the measured gap length could be correlated with the temperature applied to the fiber.

3 EXPERIMENTAL PROGRESS

3.1 Engineering/Scientific Analysis

3.1.1 Requirements Definition Study

In this section, the limitations of existing sensor technology are discussed. The advantages and disadvantages as well as limitations of thermocouples, pressure transducers and strain gages are discussed. The matrix of sensor type, location and specification is presented. The population of existing ultrasupercritical boilers that would serve as the initial market entry point for newly developed optical sensors is provided.

3.1.1.1State of Art of Traditional Sensor Technology

Thermocouples

The objective of the optical sensor development is to provide a suitable replacement for Type K or B high temperature thermocouples that would be more robust in the high temperature gas atmosphere of a utility boiler. In general, we are not looking for a replacement of the resistance-temperature-detectors (RTD's), thermistors or integrated circuit sensor. The accuracy provided by these types of thermocouples is not required for the specific applications that are identified in the matrix.

Traditional Type K or B thermocouples offer the following advantages[1]:

- Self-powered
- Simple
- Rugged
- Inexpensive
- Wide variety
- Wide range of temperatures

Type C, D, G Tungsten/Rhenium are capable of measuring temperatures up to 2760°C/5000°F but suffer from poor oxidation resistance and should be used in vacuum, hydrogen, or inert atmosphere. The poor oxidation resistance makes them impractical for fossil fuel applications.

[1] Omega Complete Temperature Measurement Handbook and Encyclopedia Vol. 27, Appendix Z. copyright 1989.

The disadvantages of these Type K and B thermocouples are as follows:

- Non-linear
- Low voltage
- Reference required
- Least stable
- Least sensitive

Type K and B thermocouples also suffer from the limitation that they cannot survive the corrosive conditions of alternating oxidizing and reducing atmosphere found in the lower furnace of a large utility boiler that employs staged combustion for NO_x control.

In addition, thermocouples that are used to monitor heat flux on the furnace walls and tubes are embedded directly in the furnace membrane or in the wall of the tube. These thermocouples cannot be protected with heavy metal sheath; and therefore, prone to mechanical failure. The optical temperature sensor being developed by Prime Photonics can use high-temperature, corrosion-resistant materials and therefore can address these disadvantages of Type K thermocouples.

The readings of Type K or B thermocouples are influenced by the following sources of noise.

- Power line (120V or 220V AC)
- Magnetically induced
- Stray capacitance in sensing and signal lines
- Ground loops

Traditional noise rejection techniques for typical thermocouples:

- tree switching – filters out noise due to stray capacitance in individual channels
- normal mode filtering—Analog filter removes broadband noise
- integration—averages noise over a full line cycle thereby eliminating power line related noise and its harmonics.
- guarding—filters out noise due to common mode interference such as 220V AC supply line.
- Twisted pairs extension wires.

Photonic sensors have a reduced sensitivity to electromagnetic interference.

Traditional sources of measurement errors.

- Poor junction connection
- Decalibration of thermocouple wire
- Shunt impedence and galvanic action
- Thermal shunting
- Noise and leakage currents
- Thermocouple specifications
- Documentation

Photonic sensors can be designed to be self-referencing, and therefore, are (with the appropriate design) less susceptible to some of the traditional sources of error associated with poor junction connections, decalibration of thermocouple wiring, etc. The photonic sensors offer the additional advantage that the electronics can be located remotely from the measurement point, thereby avoiding corruption or loss of the signal due to overheating of the electronics.

Pressure Sensors

Traditionally, pressure transducers consist of a pressure sensors (diaphragm and strain gage) coupled with compensation network. Under this project Prime Photonics is developing both components of the pressure transducer. The optical sensor technology provides the means to mount the sensor in a previously inaccessible location due to the rugged design.

Desirable features of pressure sensor[2]

- Interchangeable
- Accurate over a wide temperature range
- Operable at temperature extremes
- Durable within the external environment
- Compatible with various measurands (gases, liquids, slurries, etc.)
- Isolated from the measurand

Traditional pressure sensors consist of one of the following types of construction.

- Piezoresistive (Silicon) Diagphragms – semiconductor strain gages bonded to a silicon diaphragm
- Semiconductor strain gages bonded to a stainless steel diaphragm
- Foil grid strain gages bonded to a stainless steel diaphragm.

As indicated above for the temperature sensors, the optical sensor offers advantages over the existing sensor technology, particularly with respect to robustness at elevated temperatures.

Strain Gages

Primary application is static strain measurements rather than dynamic.

The types of measurements typically mad as follows:

- Static Loads
    - Bending
    - Axial
    - Shear
    - Torsional

[2] Complete Pressure, Strain and Force Measurement Handbook and Encyclopedia, Vol. 29 Appendix Z Omega Engineering, Inc. copyright 1995.

- Derived Quantities
    - Moment -Yes
    - Pressure – Yes
    - Acceleration – No
    - Displacement – Yes
    - Vibration – No

Traditional types of strain gages

- Piezoresistive or semi-conductor gage
- Carbon-resistive gage
- Bonded metallic wire
- Foil resistance gages

Advantages

- low cost
- short gage length
- only moderately affected by temperature
- small physical size
- low mass
- high sensitivity to strain

Factors for gage selection

- operating temperature
- state of strain (gradient, magnitude, time dependence)
- stability

Potential Error Sources

- Damaged sensor
- Electrical noise and interference
- Thermally induced voltages
- Magnetically induced voltages
- Temperature effects

Most strain gages are inherently unstable due to degradation of the bond, as well as temperature sensitivity and hysteresis caused by the thermoelastic strain. The optical sensors offer a superior approach to ensuring the integrity of the bond between the sensor and base material due to the high temperature materials of construction.

On utility boilers, sootblowers are used to keep the heat absorption surface in the boiler and convection pass clean so that steam can be produced with the minimum amount of fuel. Currently, the B&W PowerClean Intelligent Sootblower system uses gas temperatures and steam flows to monitor the heat absorption in the boiler. As heat absorption surface fouls with ash and slag, the PowerClean system directs operation of

the sootblowers to clean the surface. It would be very desireable to have temperature measurements on the surface of boiler tubes. To date this has not been possible because of the difficulty to get thermocouples to survive in the boiler and tube bank. Peak-impact-pressure (PIP) is a measure of the energy delivered to the deposit at a given distance from the sootblower nozzle.[3] The peak-impact-pressure varies as a function of sootblower spacing, media pressure and tube spacing. For utility boilers, the high end of sootblower nozzle pressures would be around 350 psig. Using a nozzle pressure of 350 psig, Diamond Power's high performance nozzle jets will produce up to 180-200 inches Hg Peak Impact Pressure (PIP) measured at a distance of 20" from the jet exit. The rugged sapphire sensors with appropriate cladding can be made to withstand the shock from the sootblower media jet impacting on the tube.

The sapphire and silica also offer superior corrosion resistance. This is especially important for monitoring burner component temperatures. Vanes and mixing devices on coal burners can reach temperatures in excess of 980 °C (1800°F) if recirculating gases are impinging on the burner front. In addition, when the burners are staged the recirculating gases can be alternately oxidizing and reducing. This cycling of gas chemistry can cause accelerated wastage of metal components. This has made it difficult to get thermocouples or strain gages to survive in this environment. Excessive temperatures (>650°C/1200°F) can cause premature failure of the burner components that require expensive repairs during plant outages.

3.1.1.2 Sensor Specifications

Preliminary specifications are established for each of three types of sensors: temperature, pressure and strain. The list of specifications is intended to address two objectives. First, for those cases where specifications are similar between traditional sensors and the optical sensors, establish quantitative values. Second, for those cases where specifications are unique to optical sensors, identify the specifications and establish preliminary quantitative values for the specifications. In many cases, the quantitative value for the specification cannot be established until more is know about the potential application. For example, due to the future availability of the optical sensors it may be possible to make measurements not currently possible with existing sensor technology. As such, a detailed error analysis would have to be performed for the intended use to determine required level of accuracy and stability. These aspects of the sensor application would be determined as part of Phase II of the project to establish final instrument specifications.

[3] Steam: its generation and use. 40th ed. Babcock & Wilcox copyright 1992 Pg 23-2.

Table 3-1. Draft Requirements for Temperature Sensors

Temperature Specification Description Specifications	Units	Value	Comments
Range	°C/°F	1700/3000	Basis Type B Thermocouple (Platinum/Rhodium);Suitable for oxidizing or inert atmosphere but not reducing, cannot be inserted into metal tubes so poor for measuring heat flux, Contaminated by hydrogen, carbon and many metal vapors (Na, K), Measure temperatures up to 1800C/3270F.
Gas	°C/°F	1700/3000	Flue Gas
Metal-Burner	°C/°F	1100/2000	Burner parts
Metal-Steam Tubes	°C/°F	870/1600	Reheater and Secondary Superheater
Output	microvolts/°C	A desireable output would be between 0.1 and 1 mv/^{o}F	Equivalent Seebeck coefficient; Type S thermocouple is 7 μV/°C at 20°C; larger number is better. Type K = 40.
Performance			
Accuracy	%	0.50%	ANSI Limits of Error
Response Time (Time Constant)	ms	1	Time required to reach 63.2% of an instantaneous temperature change
DVM Sensitivity	microvolts for 0.1°C	between 0.1 and 1 mv/^{o}C	Larger number is better.
Linearity	% full scale output	TBD	
Noise		TBD	
Stability over 1 year	% full scale output	TBD	
Media Compatibility			Most TC's are encased in a sheath and compatability depends on the sheath material
Atmosphere:			
Oxidizing			Oxidizing (CO, SO_2, O_2, CO_2, NO_x,N_2, HCl, NaO, CaO, SiO);
Reducing			Reducing (H_2S, CO, SO_2, O_2, CO_2, NO_x, COS, HCN, N_2, HCl)
Liquid			
Water			pH 9-11, 3500 psi
Steam			3500 psi, 1050°F

Table 3-2. Draft Requirements for Pressure Sensors

Pressure Sensors **Specification Description**	**Units**	**Sensor Value**	**Comments**
Specifications[4]			Transducer Value
Excitation	V dc	12 to 40 VDC	
Rangeability or turndown		~ 10:1	can vary from 2:1 to 100:1
Upper Range Limit (URL)	psi	0-5000	Ranges can extend from about 0 to 30 in. Hg to 0 to 5000 psi.
Output	mV	4-20 ma	Typical analog output
Performance			
Accuracy	% full scale output	± 0.25% of range	typical, depends somewhat on the span turndown
Linearity	% full scale output	TBD	included in accuracy spec
Hysteresis	% full scale output	TBD	included in accuracy spec
Stability	% full scale output	±0.25% of URL	over a 6 month time period
Vibration		0.1% per g, 0 to 200 Hz	
Humidity Limits	(%)	0 to 100% R.H.	
Operating Temperature Range	°C	-40 to 85	
Compensated Temperature Range	°C	-30 to 85	
Thermal Zero Effect	%	0.5% per 100 F	
Thermal Span Effect	%	0.5% per 100 F	
Burst Pressure		10,000 psi	
Response time (Dynamic Response)	ms (Hz)	1 ms/ (1000 Hz)	
Frequency response	dB at kHz		
Media Compatibility		Wetted parts typically 316 SS or Hastelloy C with Viton O-rings	
Atmosphere			
Oxidizing			CO, SO_2, O_2, CO_2, NO_x,N_2, HCl, NaO, CaO, SiO);
Reducing			H_2S, CO, SO_2, O_2, CO_2, NO_x, COS, HCN, N_2, HCl)
Liquid			
Water			pH 9-11, 3500 psi
Steam			3500 psi, 1050°F

[4] Rosemount Comprehensive Product Catalog 2002-2003 edition Emerson Process Management

Table 3-3. Draft Requirements for Strain Gages

Strain Gages Specification Description	Units	Sensor Value	Comments
Specifications			
Range	%	0.1-1.0	
Output	με @ 10 V Excitation	20	
Sensitivity	mV/V @ 1000με	2	
Gage factor (strain sensitivity, k)		2.0	
Gage factor tolerance		1.00%	
Gage factor temperature coefficient	%/°C	TBD	
Reference temperature	°C	23	Calibration at room temperature
Performance			
Service temperature range			
Static		TBD	
Dynamic		TBD	
Dynamic Response	kHz	TBD	
Mechanical Properties			
Maximum Strain	με	10,000	This is based on the 1% range needed
Hysteresis		Negligible	
Fatigue (at ±1500με))	cycles	10,000,000	
Smallest bend radius		TBD	
Media Compatibility			
Atmosphere			
Oxidizing			CO, SO_2, O_2, CO_2, NO_x,N_2, HCl, NaO, CaO, SiO
Reducing			H_2S, CO, SO_2, O_2, CO_2, NO_x, COS, HCN, N_2, HCl
Liquid			
Steam			pH 9-11, 3500 psi
Water			3500 psi, 1050°F

3.1.2 Sensor Applications

Numerous optical techniques can be used in the design of fiber optic sensors. In addition, different techniques are required for different measurands and multiplexing requirements. The optical electronics, signal conditioning, and acquisition equipment required for the various sensing techniques vary greatly. In some cases, the techniques do not lend themselves to implementation and a deliverable system. All sensor types must be evaluated to determine which concepts offer the greatest promise for development and application for power plant monitoring.

Table 3-4 presents a matrix evaluating nine common optical sensing techniques for several evaluation criteria. The evaluation process was based upon the experience of engineers at Prime Research, as well as that of other investigators as reported in the literature.

	Complexity of Manufacturing	Applicability for Pressure Measurement	Applicability for Temperature Measurement	Applicability for Strain Measurement	Cost of Development	Multiplexability	Resolution	Limitations
FBG	low	poor	good	good	low	very good	very good	limited to <200°C
LPG	low	moderate	good	moderate	moderate	moderate	moderate	limited to <200°C
IFPI	low	poor	good	good	moderate	moderate	very good	limited to <200°C
EFPI	low	good	good	very good	low	moderate	very good	
microbend	low	good	moderate	moderate	low	poor	poor	
OFDR	high	poor	good	good	high	very good	good	limited to short distances
DTS	moderate	not applicable	very good	not applicable	moderate	very good	very good	limited to <250° C
polarimetric	high	moderate	good	good	high	poor	moderate	requires special fibers
blackbody radiation	moderate	not applicable	very good	not applicable	moderate	poor	moderate	

PPE= periodic photoelasticity sensor
IFPI = intrinsic Fabry-Perot interferometer
FBG = fiber Bragg grating
OFDR = optical frequency domain reflectometer
DTS = distributed temperature sensor
EFPI = extrinsic Fabry-Perot interferometer

Table 3-4. Sensor Evaluation Table

3.1.3 Control System Interface Requirements

Requirements for interface of the high-temperature optical sensors with power plant control systems were investigated by Babcock & Wilcox engineers; results of their studies are reported in this section.

3.1.3.1 Control System Applications

Power plant control systems typically consist of two components—a distributed control system (DCS) which is used to control the operation of the system, and a data archiving system which is used to store operating data in a database for trending and analysis.

Conceivably, the Prime Photonics sensors can be incorporated into the plant instrumentation in two ways. First, the sensors can serve as input to the DCS for control purposes. Second, the sensors can serve as input to the data archiving system for monitoring and performance assessment. [B&W recommends that the sensors be used primarily for the second purpose. For high-temperature processes the primary concern will be mechanical integrity of components.]

Sophisticated power generation systems may employ neural net control. Multiple inputs from the DCS or data archiving systems will be sent to the neural net processor. The neural net will then attempt to optimize boiler control in either an advisory mode or a closed loop mode.

3.1.3.1.1 Sootblower and Waterwall Blower Control

The operation of individual subsystems on a power plant can be optimized by using better sensing techniques. For example, the sootblower system can be optimized by monitoring heat absorption on individual tubes and steam production throughout heat zone of the convection bank. Monitoring and control systems like B&W's Powerclean™ acquire temperature data and using proprietary convection bank performance codes, determine optimum sootblowing sequences. This has the effect of maximizing steam production while minimizing loss of steam through the sootblowers.

The heat flux in the furnace can be monitored with surface thermocouples on the membrane walls. Variations in heat flux from optimal can be used to control waterwall blowers or to adjust the operation of the combustion system (i.e., burners and over-fire air ports).

3.1.3.1.2 Burner and Overfire Air Control

Conceivably, an array of temperature sensors mounted at the inlet to the pendent section of the convection bank can be used to guide adjustments to the combustion system i.e., burners and overfire air ports. A non-uniform temperature distribution at the furnace exit

can be a sign that coal and air flow to the burners or air flow to the overfire air ports is not optimal. The individual temperature measurements could be processed by a neural net. The neural net could be used to optimize coal bias and air bias to the mills or air flow to each over fire air port.

3.1.3.1.3 Burner Air Bias and Vane Adjustment

Temperature sensors mounted on burner mixing devices or vanes could be used to monitor metal temperatures to avoid overheating the burner elements. Overheating can cause warping and premature failure of these components. Warping can cause vanes to seize which could prevent the vanes from being adjusted properly. The vane position needs to be optimized to minimize NO_x, CO and unburned carbon emissions. When high temperatures are observed the operator can adjust air bias to the burner to cool the burner elements. High temperatures may also be an indication of deposits on the burner which are disrupting the flow profile out of the burner. This can cause hot recirculation gases to impinge on burner elements.

3.1.3.2 Interface Requirements

3.1.3.2.1 Distributed Control System (DCS)

If the sensor is to be connected to the plant DCS as an input to the control system, then the output of the sensor needs to be in a form compatible with existing control systems, such as 1-5 Volts, 4-20 ma, 0-10 V etc. Temperature output could be in mV similar to existing thermocouple technology. The update rate of the sensor output must be fast enough to serve an input to a control system PID loop. The use of the Prime Photonics sensors for this application is probably somewhat limited since existing instrumentation is adequate for most control applications in a boiler. However, it is possible that due to the availability of a high temperature sensor, new control strategies could be conceived that previously were not considered due to the lack of a suitable sensor that could withstand the conditions where it was installed.

3.1.3.2.2 Data Archiving

For data archiving, the same approach as the DCS application could be followed or the Prime Photonics sensor scheme could be packaged as a standalone system that communicates process values via an OPC protocol. This would provide flexibility to set up the system independent of the specific installation. OPC protocol is a well-established standard. With Prime Photonics multiplex architecture the OPC protocol may provide the best interfacing option. B&W has applied this approach successfully to our Flame Doctor® and Powerclean products.

Prime Photonics sensor processing unit is well suited for a standalone system. The unit is interchangeable with various Prime Photonic sensors including simultaneous P-T and P-T-Strain. It provides high accuracy, resolution and reliability since it can be located remotely from the hostile environment of the sensor location. It can accommodate multiple channels. The output of the sensing processor unit is in digital format which is compatible with the plant DCS and data archiving systems.

In addition, the Prime Photonics architecture allows for an array of sensors to be inexpensively installed where previously it would have been cost prohibitive. For example, an array of temperature sensors could be installed on a boiler wall to map heat flux over the entire surface of the wall. This information could be used to direct the operation of wall blowers. An array of strain sensors could be mounted on convection bank tubes to perform on-line condition assessment and assist with planning repairs during an upcoming outage.

3.1.3.2.3 Communication Architecture

In the event that Prime Photonics were to supply a stand alone system with its sensor processing unit acquiring the signals from the individual sensors via the multiplexed acquisition system and generating outputs for each sensor, a protocol for communicating the information to the plant DCS or data archiving system would be required. It is recommended that the commonly used OLE for Process Control (OPC) protocol be used. An OPC server enables communication between the OPC Client (Prime Photonics sensor processing unit) and the plant DCS or data archiving system. The OPC protocol defines the format of data that is passed between the sensor processing unit and the plant's data acquisition and control systems. B&W has successfully employed this communication interface for its Powerclean™ and Flame Doctor® burner diagnostics products.

3.1.3.2.4 Platform Architecture

The move in instrumentation and control is clearly from analog to digital technology. Standards are being developed to connect analog devices to digital networks. Smart instrumentation provides not only the process value being sensed (primary variable), but also secondary variables such as device identification, device diagnostics, and status information.

Fieldbus, Profibus-PA or Highway Addressable Remote Transducer (HART) technology interfaces are available. These platforms provide easy access to information and control function. Fieldbus is a digital, two-way communications link among intelligent field-level instruments and control devices using a multi-drop network topology. HART

supports two-way digital communications for process measurement and control devices implementing a point-to-point arrangement.[5] .

The fieldbus protocol when fully implemented would replace the 4-20 ma standard. The fieldbus is 100% digital. Several advantages are realized when the control at a field device level can be achieved with the fieldbus technology. The two-way communication means that a value (such as process variable) can not only be read from the end device, but it would also be possible to write to this device (such as calibration parameters). Currently the transmission speed of the information on the fieldbus platform is 31.25 kb/s, which is fast enough to enable closed loop control. Standards for high-speed Ethernet communication have been developed that will allow transmission speeds up to 100 Mb/s. The multi-drop capability will result in a significant cost savings since it allows multiple sensors in the same general area to be connected to the control system with a single cable rather than running individual cables for each device. Wiring cost savings of 80-90% over conventional installations have been realized. This multiplexing of signals is consistent with Prime Photonics multiplexed sensor processing technology. Problems with individual sensors or control devices can be diagnosed remotely. Moving control functions from a central control room out to the end device results in more reliable control as well as a simpler central control system.

Fieldbus was developed using Instrument Society of America (ISA) and International Electrotechnical Commission (IEC) standards. The fieldbus devices and protocols are designed to meet the stringent requirements of the process industry. Foundation™ fieldbus is the most comprehensive of all fieldbus technologies currently available. Foundation fielbus has developed standard function blocks, such as analog input, digital input, PID control, analog output and digital output that provide universal interoperability between different manufacturer's devices. Unfortunately, due to the large population of analog devices currently in service, Foundation fieldbus technology will be implemented slowly over time. The best immediate application would be at a new plant.

Profibus-PA is widely used in process automation applications. Profibus-PA is an adaptation of Profibus-DP which is used for factory automation. Profibus-PA shares the same communication method as Foundation fieldbus. Profibus-PA can be configured to interface with both analog and digital devices.

The HART protocol is a hybrid that bridges the gap between analog and digital. In the HART system, the traditional 4-20 mA signal is used to represent the process variable or control output signal to or from an end device. A digital value is superimposed on top of the analog value for exchanging additional information with the device. Therefore the HART protocol is backward compatible with the installed base of instrumentation. This provides the possibility of a broader application since much of the existing instrumentation in utility power plants is still analog. FF is more readily implemented in a new installation. The HART system runs at 1200 b/s. The transmitter or control device

[5] *D'Aquino, R and Greene, R, "Forays in Smart Instrumentation" Chemical Engineering Progress Magazine, May 2003.

is interrogated with a stand alone communicator device. HART-based technology is more widespread.

In addition to the HART protocol a new IEEE standard entitled "Standard for a Smart Transducer Interface for Sensors and Actuators—Mixed mode Communication Protocols and Transducer Electronic Sheet (TEDS) Formats" (Standard 1451.4) will provide a way to enable analog sensors to connect with digital protocols.

DCS/PLC system suppliers such as Rockwell Automation, Honeywell, Siemens and ABB have all developed control system technology that can interface with HART technology. Device suppliers such as Emerson Process Management and Yokogawa have developed I/O system enhancements to allow their smart sensors to interface with the control systems. HART-enabled instrumentation is available to monitor and control temperature, pressure, level and flow.

In conclusion, Prime Photonics should develop both analog and digital outputs for the sensors being developed under this project. The analog output will be compatible with many existing installation and if necessary can be converted to a digital format. The digital output will be more compatible with future platforms that are currently being developed. Smart instrumentation provides the potential to move from corrective maintenance to preventative maintenance which will reduce down time and outage costs.

3.2 Preliminary Testing

In this section, laboratory testing and evaluation of various classes of fiber optic sensors, as well as development of high-temperature optical cladding for sapphire fibers and high temperature sapphire sensors, are described.

3.2.1 Sensor Evaluation

Tests were performed to evaluate the performance of three classes of sensor: interferometric (extrinsic and intrinsic Fabry-Perot interferometer), gratings (fiber Bragg gratings and long period gratings), and microbend sensors. The sensors were configured as temperature or pressure sensors, as appropriate for the sensor method. The sensor performance was characterized in terms of sensor resolution.

3.2.1.1 Interferometric Sensors

In the Fabry-Perot fiber sensor, two reflecting surfaces are set up within the sensor fiber itself, producing local interference, the magnitude of which is related to the optical distance between the two reflectors. The two reflectors are often made from the flat ends of optical fibers, using the normal Fresnel reflections from the surfaces, as illustrated in Figure 3-1 (a). This is called an 'extrinsic' Fabry-Perot interferometer, or EFPI. The optical interference between the two reflected light waves sets up interference at the detector, which varies sinusoidally with the distance between the reflectors. These

sinusoidal ‘fringes’ can be decoded to very accurately measure the distance between the fiber ends (the ‘gap’). By attaching the two fibers to a structure, any movement in the structure can be used to indirectly calculate the strain, or related parameters such as acoustic pressure.

Alternately, a Fabry-Perot cavity can be formed an optical fiber by modifying the refractive index of the core over some short length of the fiber (< 100μm). If the transition between the core's natural refractive index and the modified refractive index is distinct over a plane perpendicular to the axis of the fiber, then Fresnel reflections will be generated from the two transition zones as shown in Figure 3-1 (b), and interference can occur. This configuration of interferometer is termed an intrinsic Fabry-Perot interferometer (IFPI).

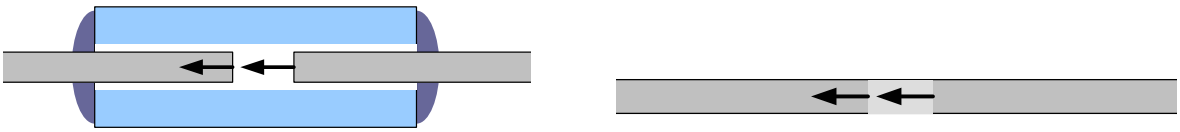

(a) (b)

Figure 3-1. Extrinsic (a) and intrinsic (b) Fabry-Perot interferometric sensors.

3.2.1.1.1 Extrinsic Fabry-Perot Interferometer (EFPI)

An alternate fiber optic sensor design incorporates an air gap between the end of an optical fiber and an extra reflector; the fiber end and the reflector form a Fabry-Perot interferometric cavity, which is generally termed an extrinsic Fabry-Perot interferometer EFPI). If some measurand induces a change in the separation between the fiber in and the reflector, the interference signal between the two reflections is modulated, and can be related to the applied measurand. For the test performed here, a variation of the EFPS sensor called the Epoxy-free Fabry-Perot Sensor (EFPS) was used. The EFPS sensor uses the same components as an EFPI to create a Fabry-Perot cavity; however, the attachment method of the fiber and diaphragm is much different as shown in Figure 3-2. The diaphragm is made of fused silica and is laser welded to the fused silica tube around the circumference of the diaphragm. In addition, the fiber is laser welded to the inside wall of the tube. Thus, the entire assembly is made of fused silica.

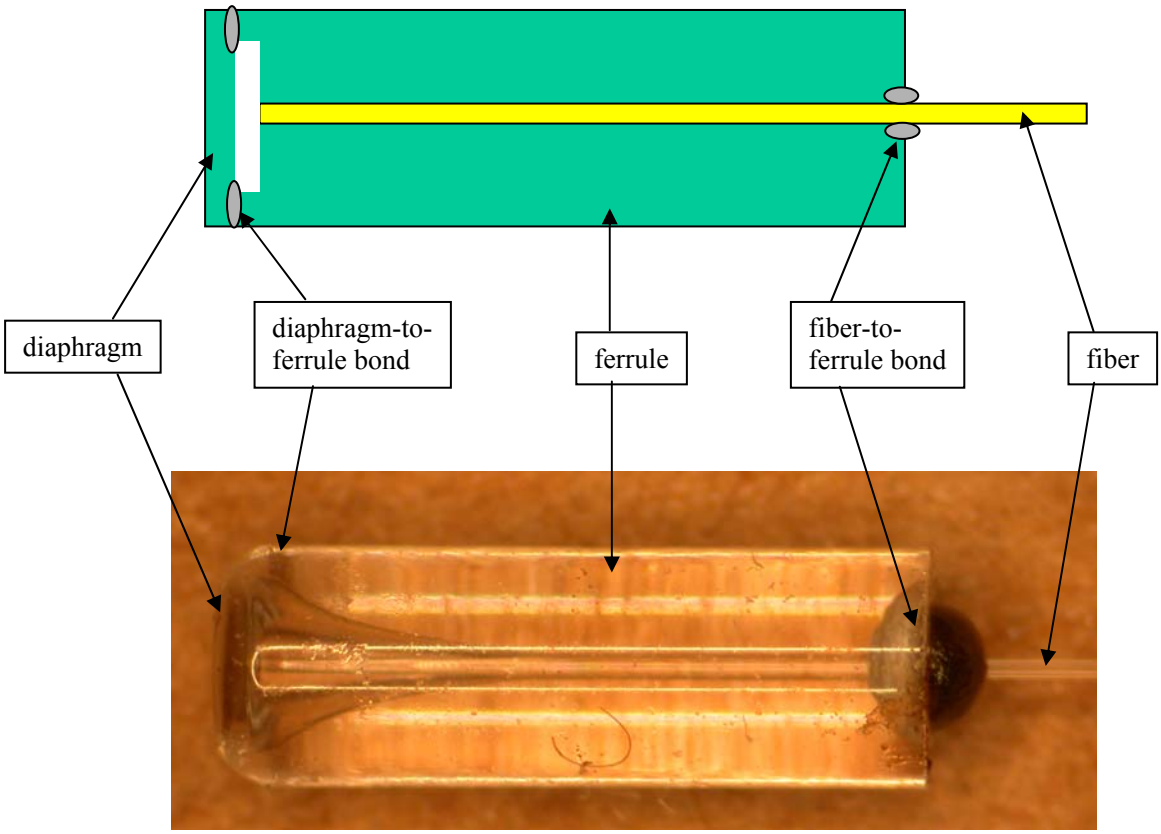

Figure 3-2. Schematic and photomicrograph of EFPS sensor.

An EFPS sensor constructed according to the schematic above was tested as a temperature sensor. The test utilized a Micron Optics si720 Component Test System (CTS) tunable laser spectrometer for interrogation. By measuring the spectral (wavelength) response of the Fabry-Perot cavity by the spectrometer, the cavity length of the sensor can be determined; more exactly, by monitoring the spectral response of the sensor, a change in the phase of the interferometric signal resulting from an applied measurand can be measured.

For this test, the EFPS sensor was placed in a furnace, and the temperature was taken from 50° C to 200° C in steps of 50° C, then allowed to cool back to 50° C and held at this temperature until conclusion of the test. It can be seen that the sensor responded to the 150° C temperature increase with a change in phase of 1.2 radians. The noise amplitude is seen to be approximately 0.02 radians. The stability of the system can be observed for the portion of the test where the temperature was maintained at 50° C, shown in the figure. During this constant temperature the phase does not have any noticeable drift. These results indicate a resolution of approximately 2.5° C.

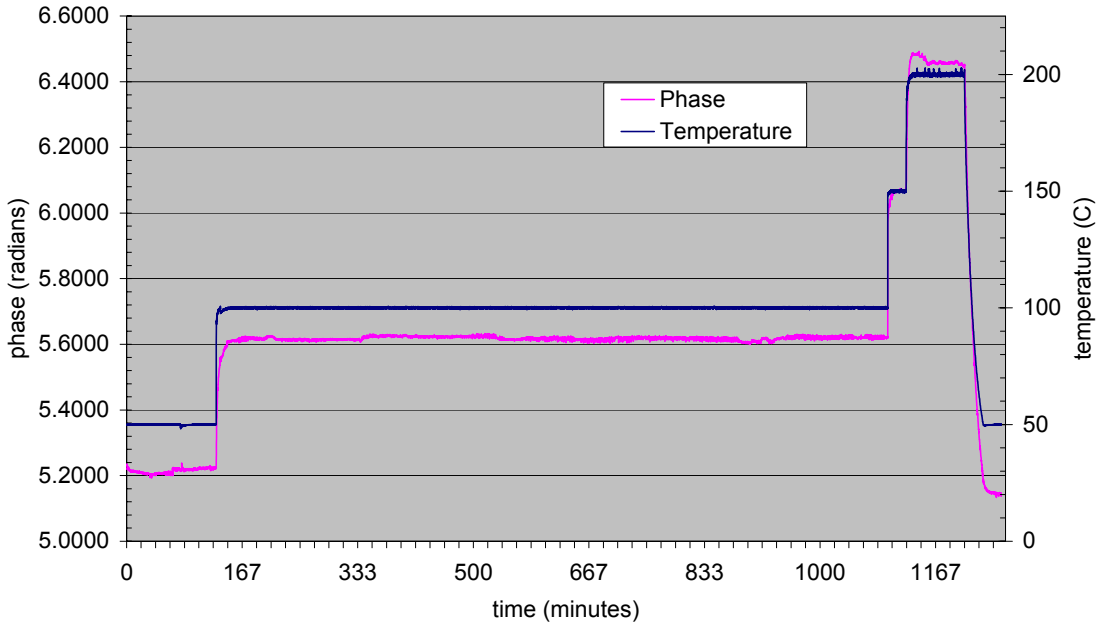

Figure 3-3. CTS interrogation of an EFPS temperature sensor. The plot shows the sensor response (phase) and the oven temperature as a function of time.

3.2.1.1.2 Intrinsic Fabry-Perot Interferometer (IFPI)

The sensor element is an intrinsic Fabry-Perot interferometer (IFPI) cavity in an optical fiber, as shown in Figure 3-1(b). In general, Fabry-Perot interferometers are formed by placing two parallel partially reflecting planar surfaces into the light path such that they are normal to the direction of light travel. While partially reflective surfaces can be constructed in a number of ways, the Center for Photonics Technology at Virginia Tech invented a unique way to place these surfaces within the existing fiber structure (hence, "intrinsic") such that there are no parts to assemble. The two planar surfaces are formed by exposing a section of photo-sensitive fiber to ultraviolet laser light. As the section of fiber is exposed to the laser light, the index of the fiber core changes such that it is different than that of the unexposed fiber. This index change creates partially reflecting surfaces at the two ends of the exposed section of fiber. This is very similar to the process used to create Fiber Bragg Gratings (FBG) in fiber; however, instead of creating a periodic pattern (many closely spaced small cavities) in the fiber as is done with FBGs, only one cavity, albeit longer in length, is written in the fiber.

To test the use of an IFPI cavity as a temperature sensor, the sensor was fabricated in Nufern GF1 single-mode fiber. This fiber is a commercially available single-mode silica fiber, with a high germanium content in the core to enhance photosensitivity. The output of a GSI Lumonics krypton fluoride excimer laser was collimated using a beam expander, and the fiber was positioned so that the laser beam was incident on the fiber perpendicular to the axis of the fiber. Approximately one inch of the polymer jacket was

stripped from the fiber to expose the glass to the beam. Two metal plates were set up in front of the fiber in order to mask off the laser output. One plate was mounted to a micropositioners, so that the gap between the plates could be adjusted. This gap defines the cavity length after exposure of the fiber.

One IFPI cavity fabricated in this fashion was tested in a small furnace as a temperature sensor. Since the color centers responsible for the refractive index modulation can be erased to high temperature annealing, the test was limited to temperatures below 300° C. During fabrication, the gap between the mask plates was set to approximately 0.5 mm. After exposing the fiber to the excimer laser output, the fiber was connected to a Micron Optics si720 CTS spectrometer. The output spectrum in Figure 3-4 was obtained, and from these fringes, it was calculated that the physical cavity length of the IFPI was 387 μm.

The fiber was then placed in a small furnace, with any Type K thermocouple to monitor the temperature. A laboratory data acquisition system was used to log the output of the CTS spectrometer during the test. The furnace was heated and after the temperature stabilized at 300° C, data logging commenced. After soaking at 300° C. for 21 hours, the temperature was decreased to 250° C for approximately four hours, after which it was increased to 300° C. for the remainder of the test. The output phase of the sensor and the applied temperatures are shown in Figure 3-5.

The temperature and phase variations over a six-hour portion of the test, over which time the temperature was held steady at 300° C, is reproduced in Figure 3-6. From these data, the temperature resolution of the sensor, after subtracting the variations in applied temperature, was calculated to be 1.1° C, based on a 2σ definition for resolution.

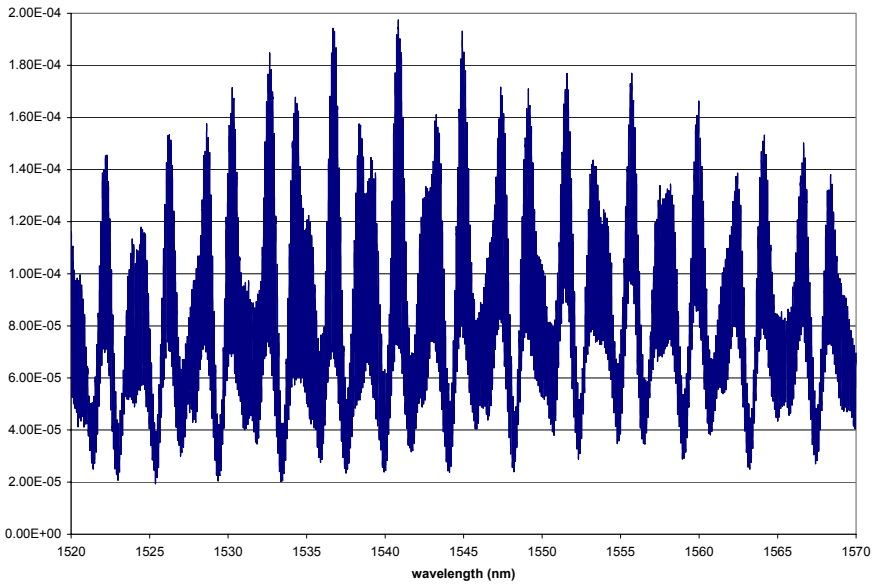

Figure 3-4. Output spectrum of IFPI sensor as measured on Micron Optics si720 CTS spectrometer.

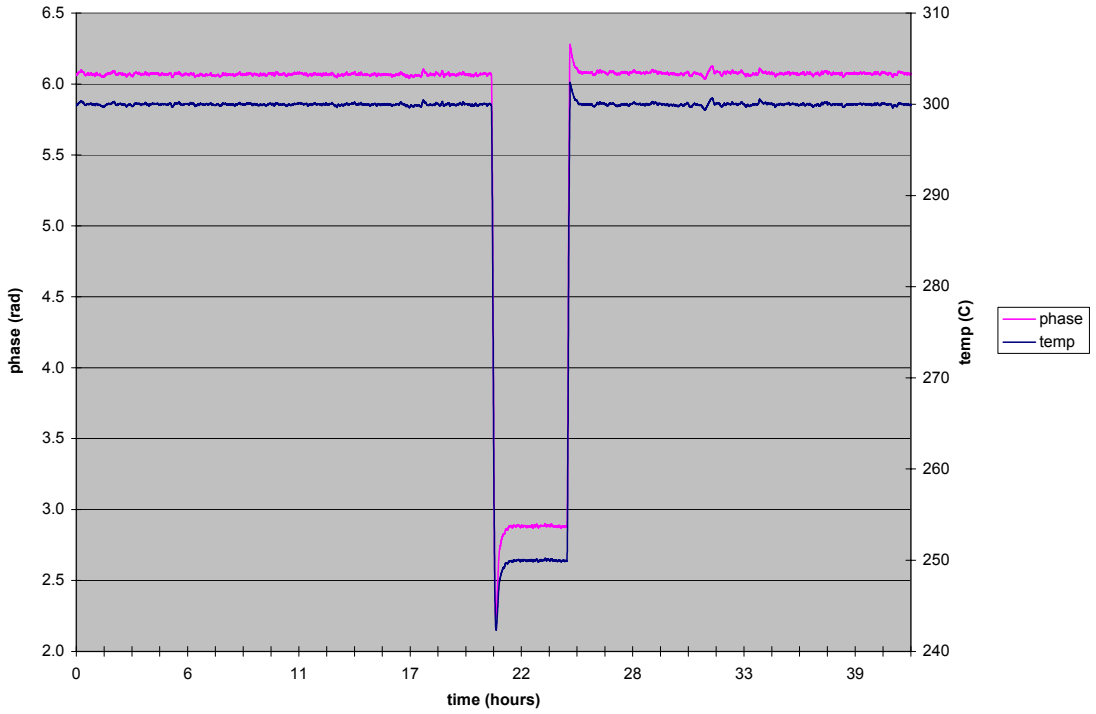

Figure 3-5. Output phase of IFPI sensor as temperature is switched from 298° C to 250° C and back.

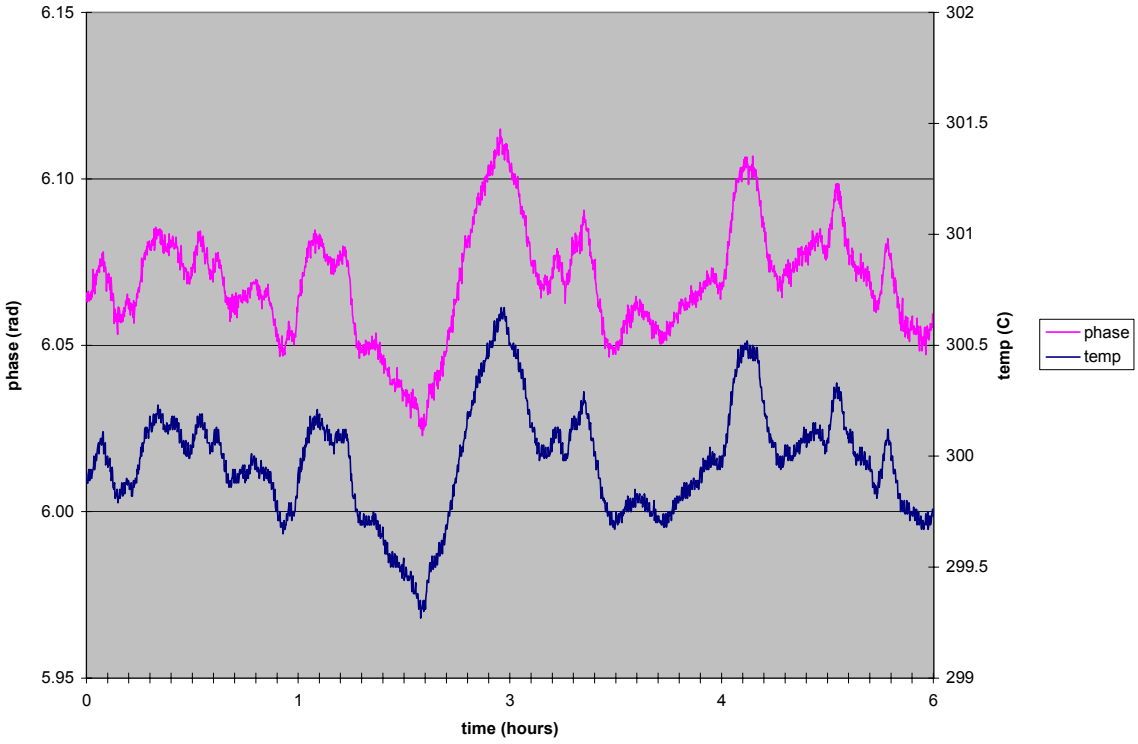

Figure 3-6. IFPI phase output and applied temperature variations over six-hour test.

3.2.1.2 Grating-based Sensors

Fiber gratings are formed when a periodic modulation of the refractive index is applied to the core of an optical fiber. If the spatial period of the modulation approximately equals half of the wavelength of the light propagating in the fiber, then the grating is classified as a fiber Bragg grating (FBG). For that structure, the FBG will reflect light with a wavelength exactly equal to the product of one half of the wavelength and the refractive index of the fiber core. In terms of fiber propagation analysis, a forward propagating LP01 mode is coupled (phase matched) by the FBG to a reverse propagating LP01 mode. Since the wavelength of the reflected light depends upon the spatial period of the grating, changes in that period due to longitudinal strain in the fiber results in a wavelength shift of the reflected light. Therefore, by designing a sensor so that the measurand induces a strain in a fiber with an FBG in the core, the magnitude of the measurand may be monitored by measuring the spectral shift of the reflected light.

If the spatial period of the refractive index modulation is on the order of 50 to 500 μm, then the grating is classified as a long period grating. In that case, the forward propagating LP01 mode is coupled by the LPG to modes that are guided by the fiber cladding. Since the evanescent electromagnetic field of the cladding modes extend slightly outside the fiber cladding, those modes interact with the media outside the fiber; in particular, the conditions for coupling from core modes to cladding modes depends upon the refractive index of the medium surrounding the fiber in the vicinity of the LPG. If the refractive index of the surrounding medium changes, then the conditions for coupling also change, and the wavelength of the light coupled into the cladding shifts. Therefore, LPGs are very effective for monitoring the refractive index of a liquid into which they are immersed. Similarly, the sensor can be engineered to monitor other measurands that can be made to result in a refractive index change of the surrounding medium. For example, LPG-based temperature sensor could be designed by surrounding the fiber with a medium whose refractive index is a known function of temperature.

In this program, FBG and LPG sensors were evaluated in laboratory tests. The LPG was a variant in which the refractive index modulation is created through application of pressure at equally spaced points along the fiber.

3.2.1.2.1 Fiber Bragg Grating Sensors

A Fiber Bragg Grating (FBG), written in silica fiber, was tested in order to determine its temperature resolution. The FBG was obtained from Lambda Instruments. At room temperature it demonstrates a moderate strength reflection with the center wavelength at approximately 1545 nm, with a small side lobe on the short wavelength side. The fabricators indicated the grating to have a length of approximately 1 mm, localized within a three inch region of the fiber.

The fiber containing the FBG was fusion spliced to a standard SMF-28 pigtail and interrogated with a Micron Optics si720 Component Test System (CTS) system. The

baseline mechanism of interrogation is to acquire a full spectrum (20,000 points resolution over the wavelength span of 1520 to 1570 nm) for post experimental analysis. The fiber was inserted into a furnace, taking care that no portion of the fiber within the furnace still possessed any polymeric coating. Once a room temperature baseline was acquired (22°C), the furnace was heated. Over a period of approximately 3.5 hours the furnace was heated 495°C (the upper limit of this particular furnace.) Scans were taken regularly (24 in total) during this temperature increase.

The data was analyzed in MatLab™. After importing the data, the data was lightly smoothed to ensure accurate peak detection. A plot of the raw data (over a reduced portion of the spectrum, to highlight the salient characteristics) can be seen in Figure 3-7. The red circles indicated the locations of the peaks. In Figure 3-8, one can see the wavelength shift as a function of temperature applied to the grating. In Figure 3-9, the inverse data is illustrated, representing the temperature as a function of wavelength shift. Given the VL200 has a wavelength resolution of 1 picometer (pm) the temperature resolution of such a system is given by the slope of this curve. In this case, a temperature resolution of 0.168°C is shown. This is likely to be improved by use of a higher quality (narrower bandwidth) FBG.

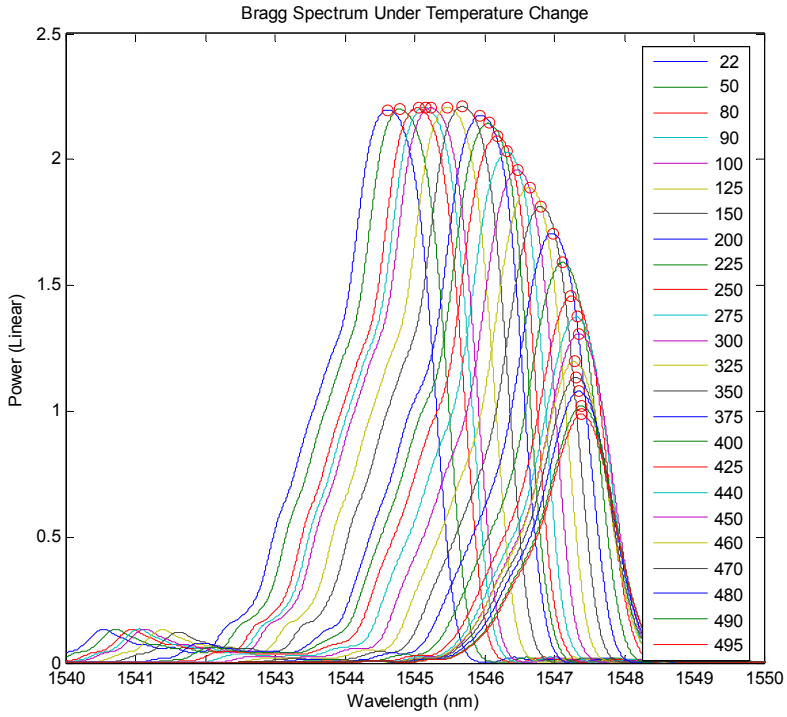

Figure 3-7. Spectral response of Bragg Grating

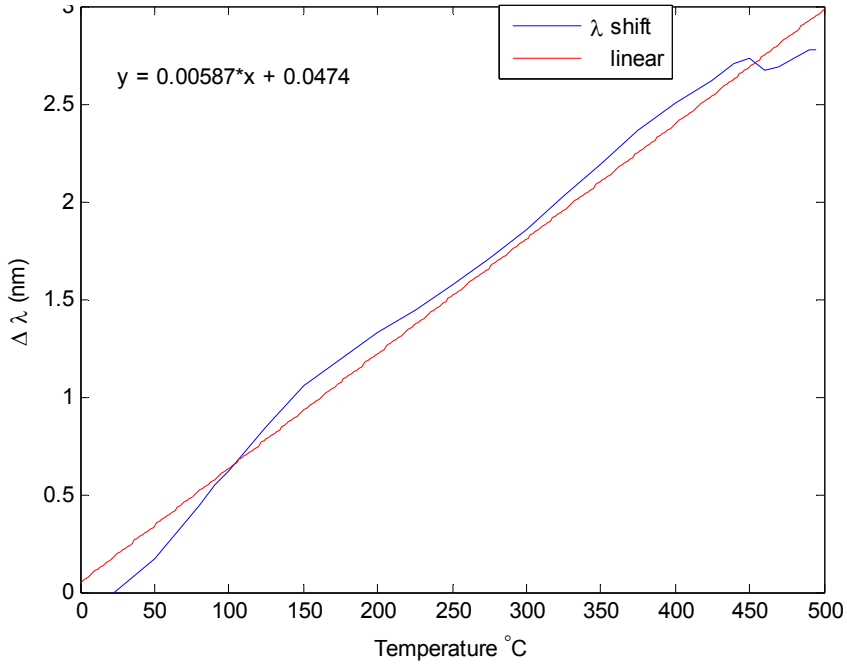

Figure 3-8: Wavelength shift as a function of temperature

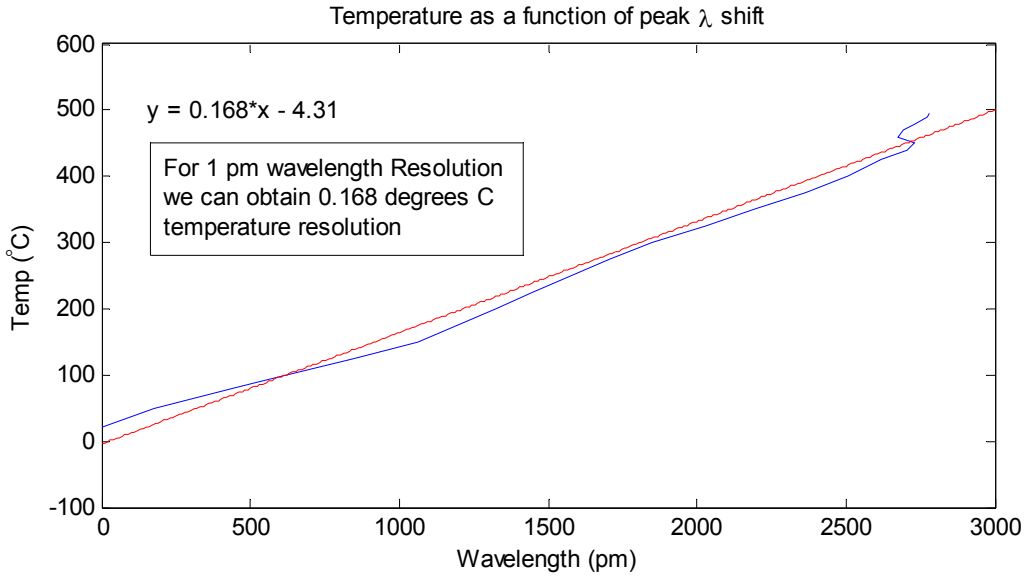

Figure 3-9: Temperature resolved as a function of wavelength

3.2.1.2.2 Long Period Grating tests

Most commonly, long period grating sensors are used to measure the change in refractive index of the medium surrounding the fiber. This is most useful for sensing chemical or biological elements in the immediate environment of the grating, but the coatings needed to accomplish this will generally not withstand the harsh conditions of the steam boiler or other power plant applications. However, a variation of the LPG sensor can be used to measure hydrostatic pressure. In this approach, periodic perturbations of the refractive index of the core of an optical fiber, induced by applied hydrostatic pressure, promotes coupling of guided electromagnetic modes to lossy cladding modes. As Figure 3-10 shows, a single mode fiber is positioned to rest on top of the plate with machined periodic grooves. A pressure plate is used to press the fiber against the groove plate. Through photoelasticity, the refractive index of the fiber will increase slightly in those sections were the fiber contacts the groove plate. The fiber refractive index is unchanged where the fiber rests above a groove in the bottom plate. By monitoring the transmission spectra of the fiber, losses in certain spectral bands can be correlated with the pressure amplitude. Here, the center wavelengths of the loss bands are dictated by the period of the machined grooves, and the amplitude of the loss peaks are related to the magnitude of the pressure applied to the plates.

The emphasis of the research presented here has been the demonstration of that correlation between pressure and loss.

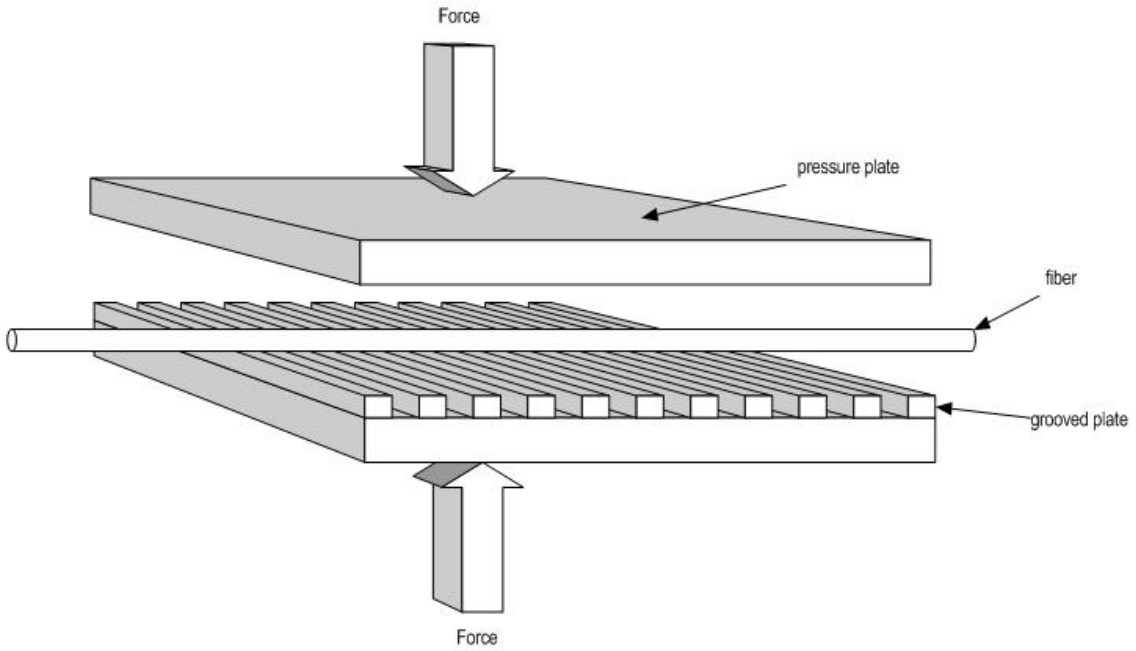

Figure 3-10. LPG sensor for measurement of pressure through periodic photoelasticity.

To demonstrate the correlation, a sensor was constructed using a 'sandwich' structure, in which a length of gold-coated optical fiber was sandwiched between two metal strips. One of the metal strips has periodic teeth machined in the surface, as shown in Figure 3-10. Metal strips with varying periodicities were tested. Room-temperature curing epoxy was used to fix the fiber to both ends of the metal strips. The whole sandwiched structure was covered tightly by a soft elastomer, with the ends sealed by epoxy.

The sensor was installed inside a pressure chamber with fiber optic pressure feedthroughs used to permit access of the fibers to the outside. A Pressure Systems Inc. pressure calibrator was used to apply hydrostatic pressure to the sensor. The working fluid was purified gaseous nitrogen. White light was injected into one end of the optical fiber, and an Anritsu optical spectrum analyzer was used to measure the transmission spectrum of the optical fiber (Figure 3-11).

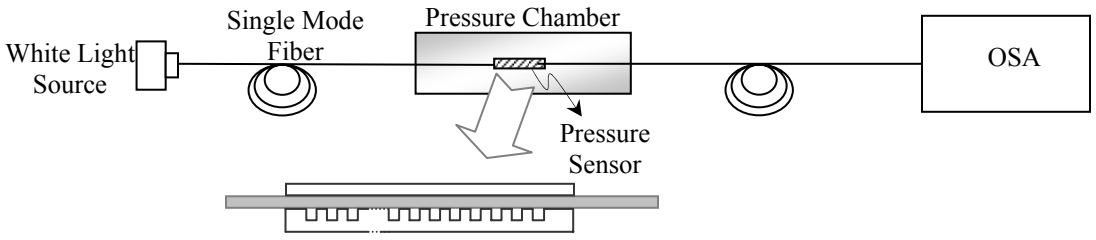

Figure 3-11. Experimental set-up to characterize pressure-induced LPG.

In the first experiment, pressure was applied to the sensor at discrete values of 40, 50, 60, 70 and 80 psi. The corresponding spectra are shown in Figure 3-12.

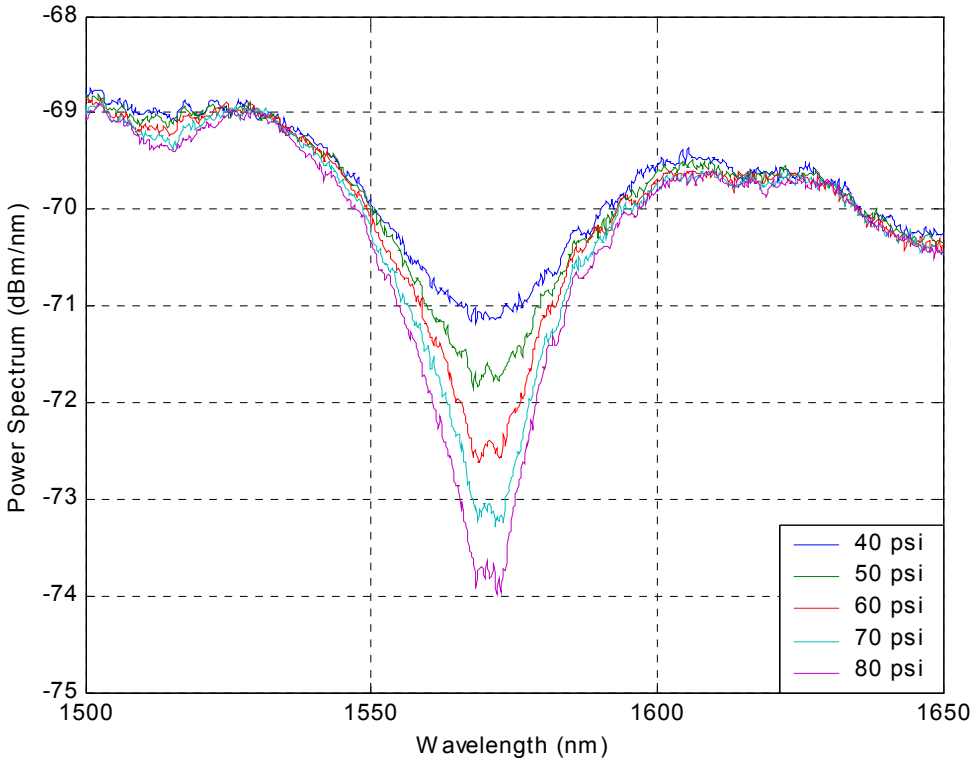

Figure 3-12. Transmission spectra of pressure-induced LPG sensor for discrete applied pressures.

In order to convert the change in transmission spectra to a single-valued parameter that could be correlated with pressure, the peak loss of the loss band in the transmission spectrum was calculated. Since the spectra are not smooth at the peaks, the average transmitted spectrum power P_1 (dBm) over the wavelength range from 1560nm to 1580nm was numerically calculated. As a baseline to determine the loss caused by mode coupling, the average power P_2 (dBm) over the wavelength range from 1515nm to 1535nm, which is far removed from the peak wavelength, was calculated. Then the loss can be determined as

$$\text{Loss (dB)} = P_2 \text{ (dBm)} - P_1 \text{ (dBm)}$$

The results are shown in Figure 3-13, which uses a logarithmic plot to express the result, and Figure 3-14, which employs a linear scale. Alternate approaches to determine peak loss in the spectra could employ fitting polynomials to the data, and determining the local maximum of the polynomial.

The stated loss accuracy of the Anritsu spectrometer is ±0.1 dB. From the slope of Figure 3-14, this implies a minimum resolvable pressure of 4.4 psi for this sensor, using the Anritsu OSA to interrogate the sensor.

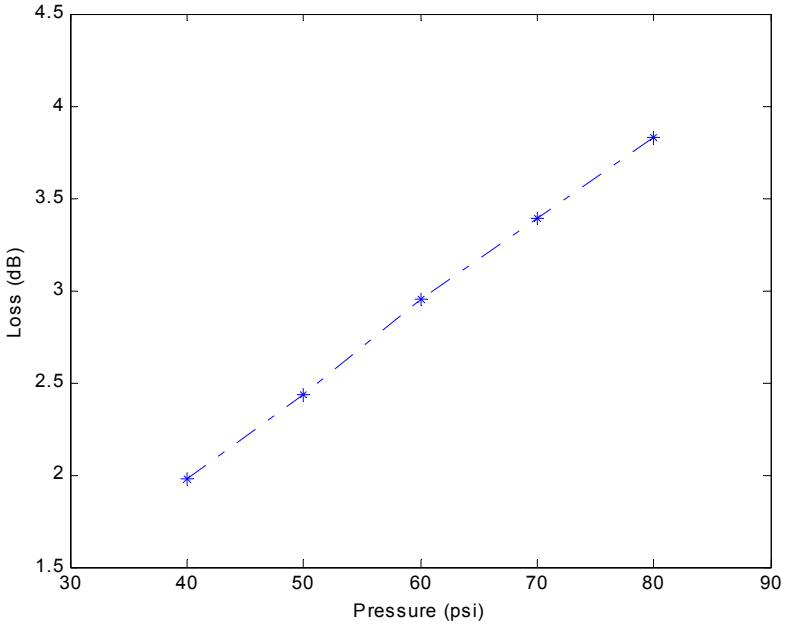

Figure 3-13. Loss vs. pressure (logarithmic scale)

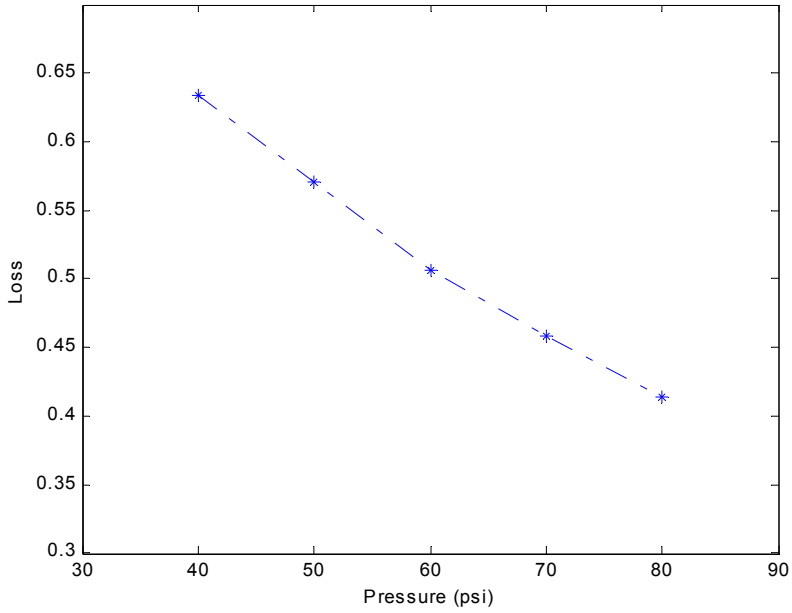

Figure 3-14. Pressure vs. normalized transmitted power (linear scale)

The repeatability of the sensor was tested by measuring the transmission spectrum at 80 psi three times. The results are plotted in Figure 3-15. The tests show a decrease in the peak loss for each successive test. The reason for this behavior is not clear at this time, but may be related to viscoelastic (time-dependent) relaxation in the epoxy used to fix the fiber to the plates. The results of the limited experiments presented here confirm that periodic variations of the refractive index of an optical fiber core induced by photoelasticity can be used to relate changes in the transmission spectrum of the optical fiber to pressure applied to the structure encapsulating the fiber.

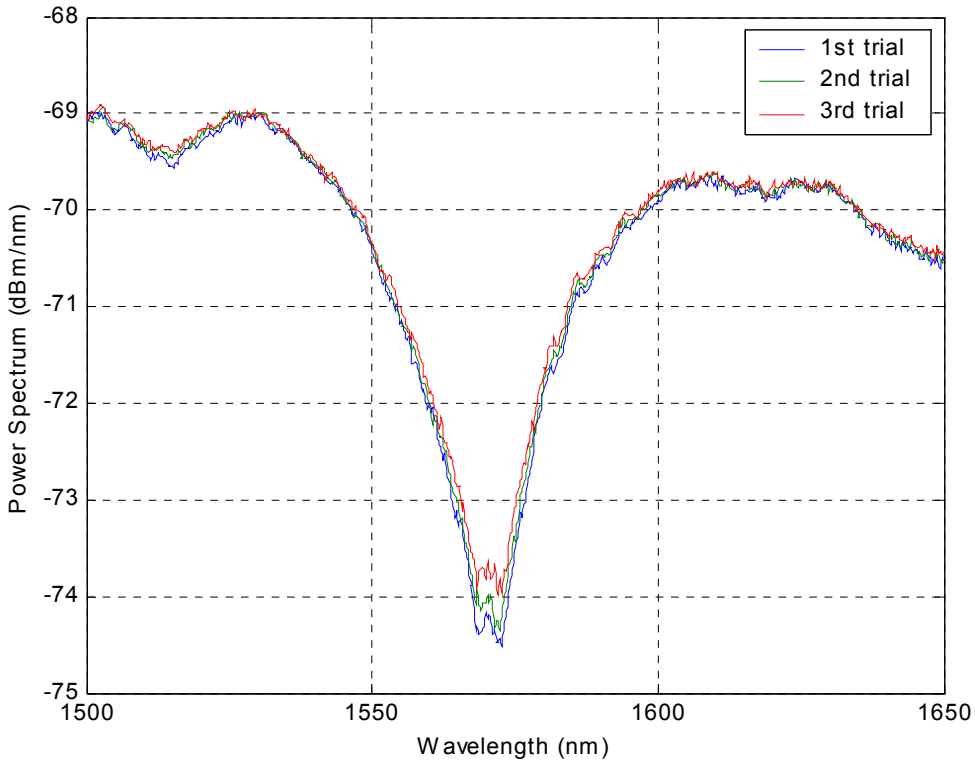

Figure 3-15. Transmission spectrum for 80 psi repeated three times.

3.2.1.3 Microbend Sensors

Microbend displacement sensors are based on the optical loss in an optical fiber induced by small bends in the fiber by some measurand. When a fiber is subjected to microbends (small periodic deformations), light rays propagating in the fiber can exceed the critical angle required for total internal reflection; in that case, the array is no longer guided and is coupled into the cladding, word is usually absorbed by the lossy polymer jacket. Intensity based sensors generally have lower resolution and dynamic range than interferometric based sensors due to their sensitivity to noise. However, they do not require complex signal processing techniques and are much less expensive. Microbend

sensors have been configured for the measurement of many different parameters including strain, temperature and pressure.

Under this Phase I program, tests were conducted to estimate the resolution of a microbend displacement sensor based on single mode fiber (core size 9.5um).

3.2.1.3.1 The sensor configuration

One type of microbend sensor uses multimode fibers with core size of 60 um or larger, which support the propagation of several thousand electromagnetic modes of light. In the process of microbending, the number of guided modes and the power carried by them changes. In our approach, we used the single mode fiber as the sensor element and a distributed feedback (DFB) laser diode as the source of light.

The general configuration of the sensor system is presented in Figure 3-16. The output from a laser diode with peak wavelength of 1545 nm is coupled into a single mode fiber. An attenuated was used to reduce the intensity of the laser output, so that the photodetector is not saturated. After attenuation, the laser light propagates through the fiber under a mechanical deformer. The deformer, used to microbend the optical fiber, consists of a pair of metal plates, each with periodic flat ridges on one side (see Figure 3-17). The period of the ridges is 1.6 mm, and the total length of the deformer is 100 mm.

The output of the fiber (after the deformer) is coupled to a photodetector, which converts the optical signal to electrical signal. A PCI-DAS6070 data acquisition card, with the digitization rate of 1000 ksamples/s, was used to digitize the electrical signal. Graphical interface software written in Borland C++ allowed us to observe the signal and calculate its standard deviation in real time.

As shown in Figure 3-17, the fiber, in its plastic jacket, passes between the two deformer plates. A static displacement of the upper plate was induced by manually adjusting a screw contacting the top of the plate; this produced quasi-square distortions of the fiber. The lower plate of the deformer was fixed in all tests.

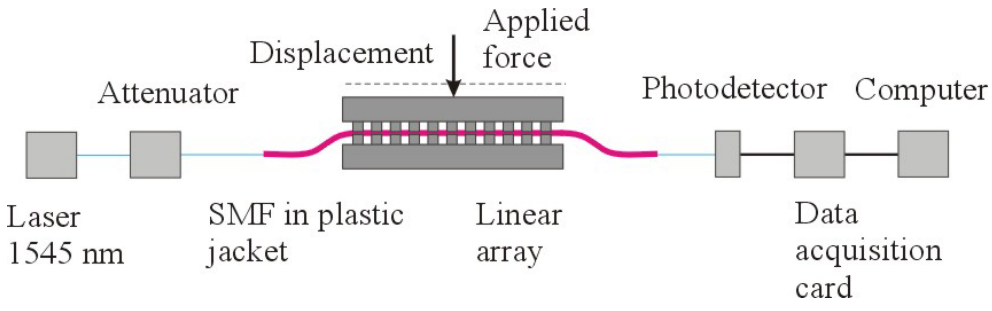

Figure 3-16. Schematic for the microbend sensor tests

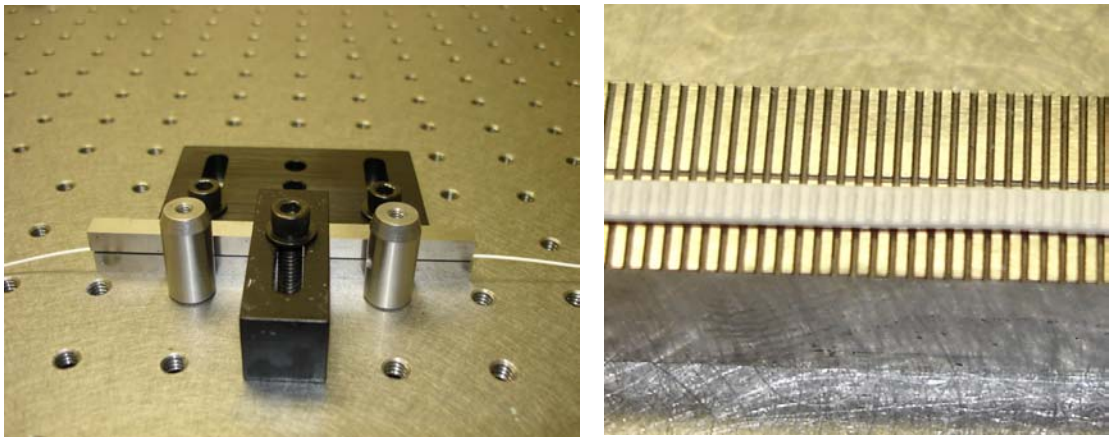

(a) (b)

Figure 3-17. Microbend sensor design (a- mechanical deformer, b- linear deformer and optical fiber in plastic jacket)

The zero displacement position was defined as the upper plate position at which output light power started to change. Due to the viscoelastic mechanical behavior of the plastic coating, some drift was observed at the beginning of the test. However, the repeatability of the sensor was significantly improved after periodically applying high and low pressure to fiber with the objective of reducing the plastic jacket deformation memory.

3.2.1.3.2 Microbend sensor dynamic range and resolution

The microbend sensor dynamic range was limited by the following reasons: for small fiber deformations, the optical losses were small and the sensor had low sensitivity. Large deformations saturated the attenuation in the fiber.
In the test, the deformer displacement was increased in steps of 16.1 um. For each displacement step, the data acquisition system collected 250 samples from the photodetector in a time interval of 10 s. Then a mean value of the signal was calculated according to the formula

$$< x >= \frac{1}{N}\sum_{i=1}^{N} x_i$$

Equation 1

where x_i is the ith measurements of x, the photodetector output.

The standard deviation σ was calculated according to

$$\sigma = \sqrt{\frac{1}{N-1}\sum_{i=1}^{N}(x_i - < x >)^2} \ .$$

Equation 2

The mean value of the optical power transmitted through fiber as a function of deformer displacement is shown in Figure 3-18. In general, the curve is nonlinear for the range of displacement from 0 μm to 145μm. The linear part of the curve is limited from 70 μm to 95 μm.

The sensor displacement resolution η was calculated by formula

$$\eta = \Delta_{displacement}\left(\frac{2\sigma}{\Delta_{power}}\right),$$

Equation 3

the $\Delta_{displacement} = 16.1\,um$ is the change in displacement, and $\Delta_{power} = P_1 - P_2$ is the difference in optical power corresponding to the displacement.

Figure 3-19 shows the dependence of the sensor resolution as a function of the deformer displacement. According to the curve, the sensor resolution is variable and depends upon displacement. The minimum resolution of ~0.05 um corresponds to the interval of displacement from 70um to 95um. On Figure 3-18, the same interval corresponded to the linear part of the curve. Beyond the linear range of the curve, the sensor resolution increases rapidly and reaches a value 0.6 um.

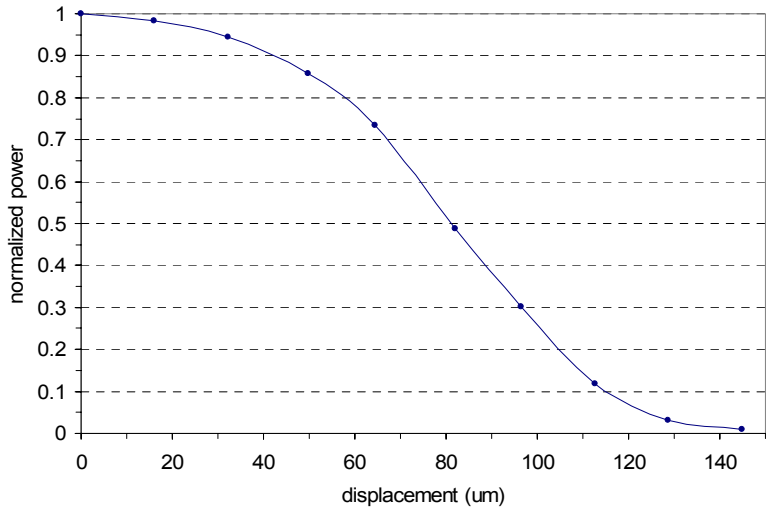

Figure 3-18. Measured attenuation of the optical power as a function of the displacement.

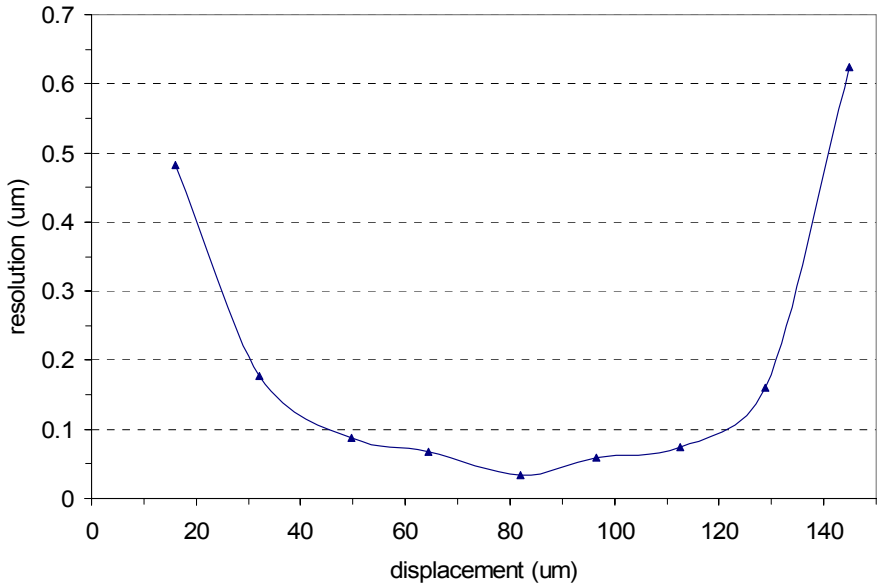

Figure 3-19. Displacement resolution of the microbend sensor

3.2.2 Clad Sapphire Fiber Development

Progress was made in the development of materials and methods to apply high-temperature optical claddings to sapphire fibers, in order to improve their optical waveguiding properties and reduce their mode volume. Through refinements in the processing steps, the quality of the interface between core and cladding of the fibers was improved, which is expected to reduce scattering and attenuation in the fibers. Numerical aperture measurements of both clad and unclad sapphire fibers were obtained in, and used to estimate the reduction in mode volume afforded by the cladding.

The progress reported here emphasizes progress in cladding development during the last half of the Phase I effort. Discussions of the achievements obtained in the first half of the Phase I program may be found in the 1st Semiannual Technical Report for the program.

3.2.2.1 Samples Prepared Using Nanopowders

The goal to incorporate MgO nanopowders is to examine their effects on the spinel cladding properties. In general, in the sintering of ceramic body, the smaller the particle size, the larger is the driving force for sintering. This implies that powders with finer sizes can be sintered at lower temperatures and in a shorter period of time. However, the driving force for grain growth is also larger for finer grain powders. In the sintering of

nanopowders, the competition between densification and grain growth greatly diminishes the chance of achieving dense ceramic body with nanometer-scale structures.[6] Another goal for using nanopowders is to increase the mechanical strength of the converted spinel cladding.

In contrast to the sintering of consolidated ceramic body described above, in the current project, the slurry consisting of MgO and $MgAl_2O_4$ powders is dip-coated on the surface of a sapphire fiber. After drying and binder burnout, the ceramic powders in the coating pack less densely in comparison to, say, the packing density of a ceramic body consolidated using isostatic pressure. As the temperature increases, the MgO in the coating starts to diffuse into the sapphire, and reacts with Al_2O_3 by converting it to $MgAl_2O_4$. At the same time, the Al_2O_3 in the fiber also diffuses outwardly into the coating, although to a lesser extent.[7] In addition, the sparse coating structure consolidates when the temperature rises.

3.2.2.1.1 Recapitulation of Previous Results

Samples prepared using μm-range powders that possesses that most promising properties will be discussed first. The sample is prepared using MgO powders from EM Science and spinel powders from Baikalox . The powders were hand ground using pestle and mortar followed by ball milling. During these grinding and milling stages 2-propanol was added as a solvent, and the slurry was heated on a hot plate at the end to remove 2-proponal. To prepare the slurry batch, 2- propanol (solvent 1), 1-ethoxy-2-peopanol (solvent 2), polyvinylpyrrolidone (binder), and polyethylene glycol (plasticizer) were mixed in a beaker, and then the powders were added into the beaker. The constituents of the slurry are listed in Table 3-5. The slurry was then further ball milled. Before fiber dipping, the slurry was constantly stirred using a magnetic stirring bar in a beaker. Since an unknown amount of 2-propanol evaporated from the slurry, the weight % of 2-propanol at the moment of dipping was likely smaller than the number shown in Figure 3-20. The drying, binder burnout, and sintering profiles are shown in Figure 1. The sample, 14(17)s, was dipped in this slurry. The polished cross section of sample 14(17)s is shown in Figure 3-21.

[6] I.-Wel Chen & X.-H. Wang, "Sintering dense nanocrystalline ceramics without final-stage grain growth", Nature, Vol 404, 9 March 2000, p.168.

[7] Ronald C. Rossi and Richard M. Fulrath, "Epitaxial of Spinel by Reaction in the Solid Stae", Journal of the American Ceramic Society, v. 46, n. 3, March, 1963, pp.145-49.

Table 3-5: Components of slurry batch "Fine Powders" (sample 14(17)s)

Sample Name: 14(17)s Slurry Batch: Fine Powders			
	Component	Weight (g)	Weight %
Solvent 1	2-propanol	37.43	91.1
Solvent 2	1-ethoxy-2-peopanol	3.06	7.4
Binder	PVP (m.w.: 1.3 M.)	0.45	1.1
Plasticizer	Polyethylene glycol	0.15	0.4
Powders	MgO (EM Science,)	3.85	Total: 5.14
	$MgAl_2O_4$ (Baikalox,)	1.28	
Solid Loading = 5.14/(5.14+37.43)=12.1%			

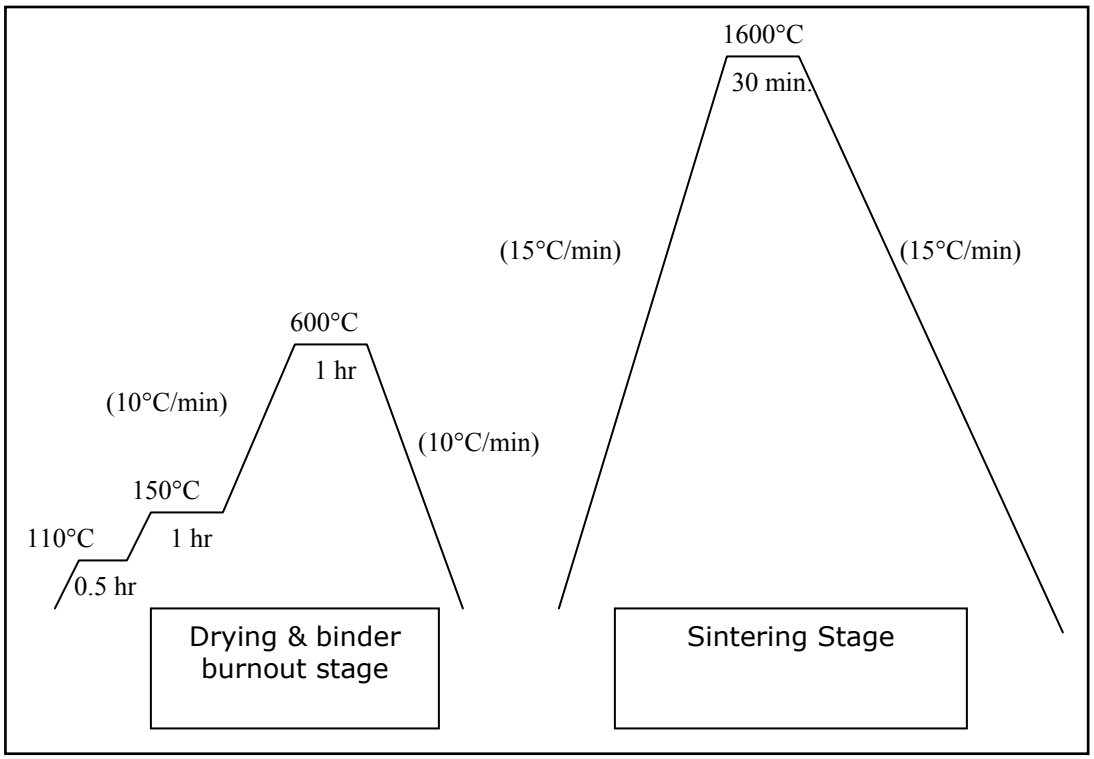

Figure 3-20. The firing Profile of sample 14(17)s

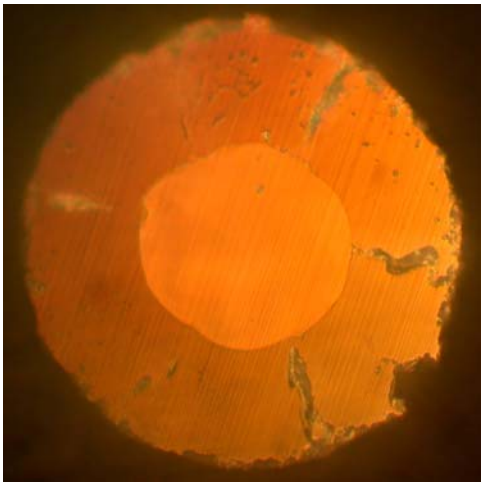

Figure 3-21. Sample 14(17)s

The cladding thickness is relatively uniform; however, there are large cracks. The core/cladding interface is not perfectly concentric, but the interface is very smooth. Very little residuals exist on the cladding surface.

3.2.2.1.2 The First Attempt on Samples Prepared Using Nanopowders

The first batch of nanopowder slurry was prepared using MgO nanopowders from Aldrich (130 m^2/g,) and spinel powders from Alfa Aesar (10 m^2/g,). The constituents of the slurry are listed in Table 3-6. The slurry was ball milled after mixing. There was a delay of several days between the slurry preparation and the actual fiber dipping, so the weight % of 2-propanol at the moment of dipping may be smaller than the number shown in Table 3-6, due to the evaporation of 2-propanol during processing and storage. A fiber, sample 34x, was coated using this slurry. The drying, binder burnout, and sintering profile are shown in Figure 3-22. Based on the assumption that nanopowders have a greater driving force for sintering, the dwelling time at 1600°C was chosen to be much less than for sample 14(17)s. The polished cross section of sample 34x is shown in Figure 3-23. The fiber is still imbedded in the matrix used in polishing. It can be seen in Figure 3-23 that there is a significant amount of slurry coating surrounding the cladding not fully reacted. It is clear that the dwelling time at 1600°C was not enough to fully react the entire slurry coating. The same sample was fired again at 1600°C for a longer time to examine whether the residuals can further react and disappear. The polished cross section after the section firing is shown in Figure 3-24. Here the cladding thickness is much larger compared to that before the second firing, and the degree of residuals on the surface of cladding is greatly reduced. This indicates that during the second firing, the remaining residuals diffuse inward and reacted with the sapphire core. Furthermore, large

cracks start to appear, presumably due to the huge increase in volume, i.e., 50%, originating from the phase transformation between sapphire and spinel.[8]

The core/cladding interface here is rougher and more irregular. There are two possible causes for this interface roughness. First, the powder packing in the coating is not uniform, denser in some regions and sparser in others. A sparse and inhomogeneous powder packing results in a porous structure with large voids in the coating after consolidation. These voids can impede the local diffusion rate of molecules in the coating towards the sapphire fiber, thus reduce the reaction rate of the converted spinel cladding. After diffusion and interaction with the sapphire fiber, this tenuous structure in the coating regenerates itself at the core/cladding interface. Packing density and uniformity of the slurry coating also influence the amount of residuals not fully reacted after firing: the better the powder packing, the less are the residuals after firing. Another cause for the irregular interface might be the excessive grain growth of the spinel grains at core/cladding interface due to over-firing. In order to achieve the largest possible packing density and its uniformity in the coating, the powder sizes, their distributions, and the perfect dispersion of the powders in the slurry are critically important.

Table 3-6. Components of slurry batch Nano-1.0 (sample 34x)

Sample Name: 34x Slurry Batch: Nano-1.0			
	Component	Weight (g)	Weight %
Solvent 1	2-propanol	28.62	92.0
Solvent 2	1-ethoxy-2-peopanol	2.04	6.6
Binder	PVP (1.3M m.w.)	0.32	1.0
Plasticizer	Polyethylene glycol	0.14	0.4
Powders	MgO (Aldrich,)	2.76	Total: 3.68
	$MgAl_2O_4$ (Alfa Aesar)	0.92	
Solid Loading = 3.68/(3.68+28.62)=11.4%			

[8] Louis Navias, "Preparation and properties of spinel made by vapor transport and diffusion in the system $MgO\text{-}Al_2O_3$", Journal of the American Ceramic Society, v. 44, n. 9, September 1961, pp.434-46.

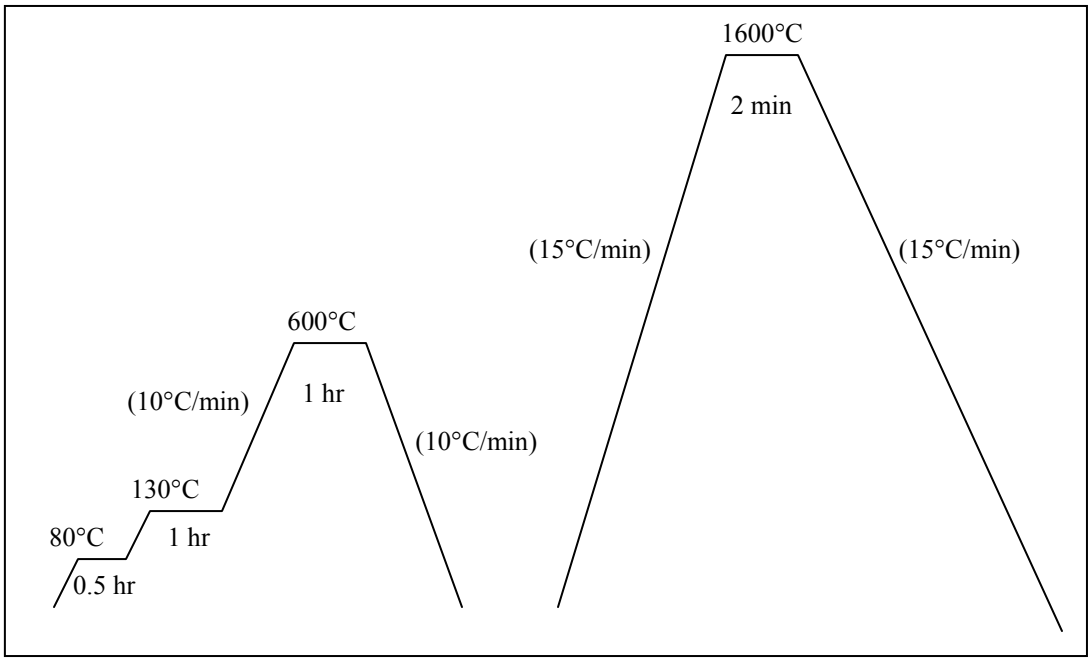

Figure 3-22. The firing profile of sample 34x

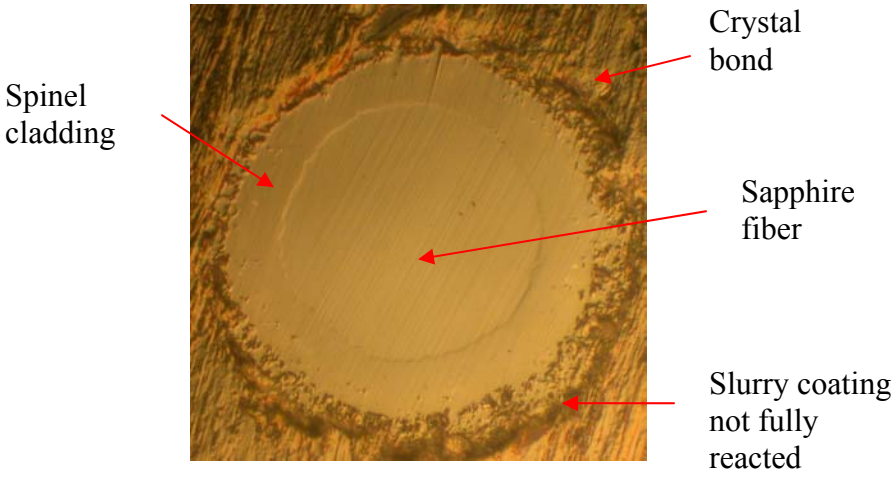

Figure 3-23. Sample 34x

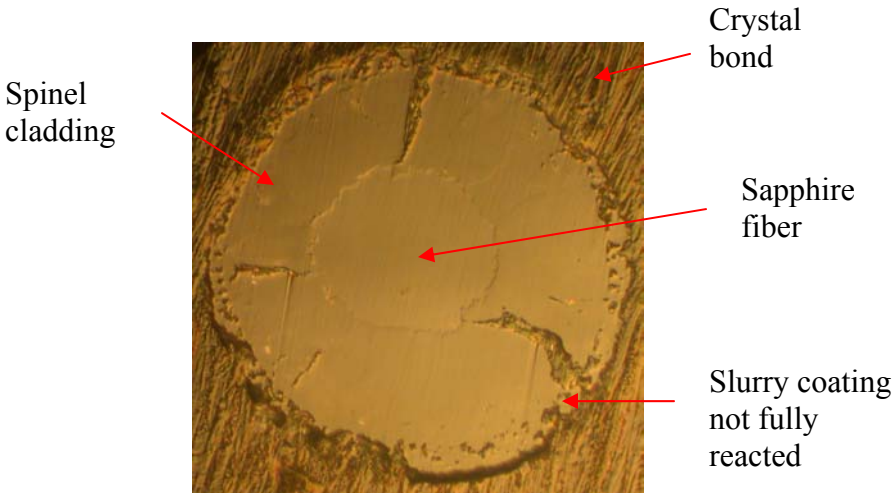

Figure 3-24. Sample 34x after the second firing

Sample 34x prepared using nanopowders has two rounds of firing at 1600°C for a total of 32 minutes, while the sample using μm-range powders, i.e. sample 14(17)s, has one round of firing at 1600°C for 30 minutes. The drying and binder burnout stages are almost the same for these two samples. The firing profiles and slurry compositions of the two samples are quite similar. As shown in Figure 3-21 and Figure 3-24, sample 14(17)s does not have as much residuals as in sample 34x, which indicate that the powder packing in sample 34x may be less dense and lea uniform than those of sample 14(17)s. This tenuous coating structure in the coating prepared by nanopowders impedes the molecular diffusion into the fiber, thus increases the amount of residuals. It shows that the particle sizes and their distributions and the degree of powder dispersion in the nanopowder slurry are inferior. On the other hand, the core/interface of sample 14(17)s is smoother than that of sample 34x, which points out that the single firing stage at 1600°C for 30 minutes is optimal to achieve a smooth interface for sample 14(17)s, while the two rounds of firing at 1600°C for a total of for 32 minutes is excessive for sample 34x. It is also possible that the rough interface in sample 34x is a direct regeneration of its tenuous coating, as discussed the previous paragraph.

After the second firing, the slurry was ball milled again, and then it was stirred constantly in a beaker for until it was used to dip another fiber, sample 24z. Sample 24z was fired at 1600°C for 30 minutes, as illustrated in Figure 3-25. It has the same drying and binder burnout profiles as those of sample 34x. The 30°C per minute rapid cooling from 1600°C is designed to reduce the chance of excessive grain growth at high temperatures, and the slow cooling from 1100°C to room temperature is for reducing the degree of cracking in the cladding. It was expected that this firing profile should creates samples similar to sample 34x, in which there is only a negligible amount of residuals. The polished cross section of sample 24z after firing is shown in Figure 3-26. It shows huge amounts of residuals, much more than sample 34x. The features in sample 34x can not be repeated

using the same batch of slurry that has been stirred in a beaker for a period of 15 days. It is suspected that the degree of agglomeration of powders in the slurry may be slowly increasing, thus resulting in even poorer packing density after drying.

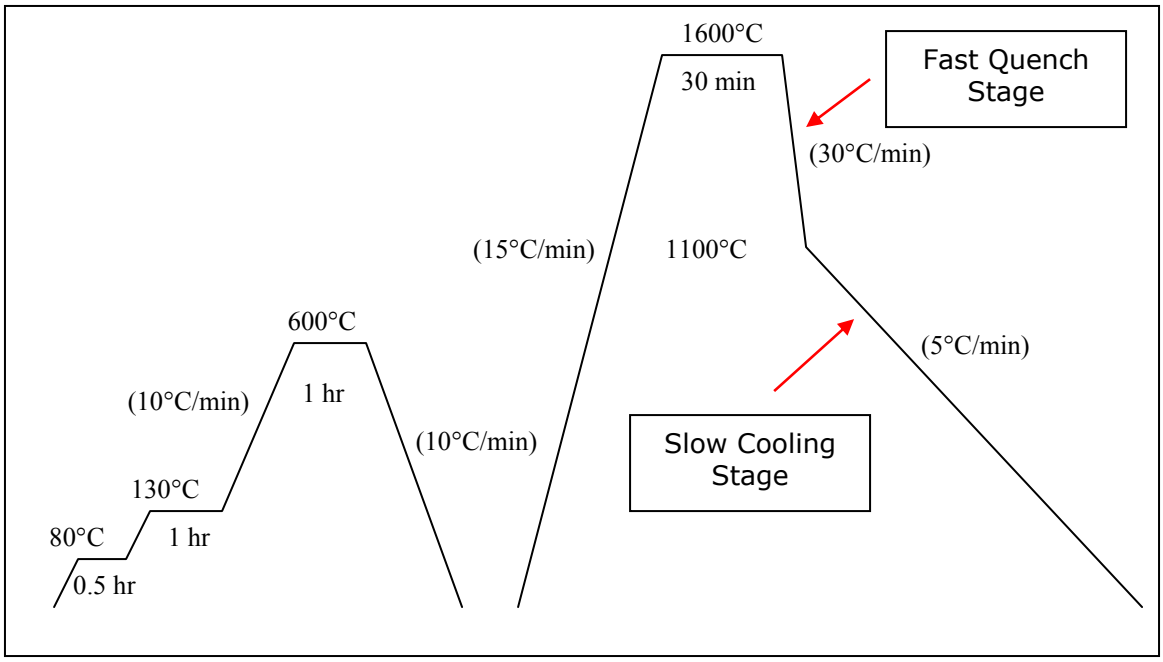

Figure 3-25. The firing profile of sample 24z

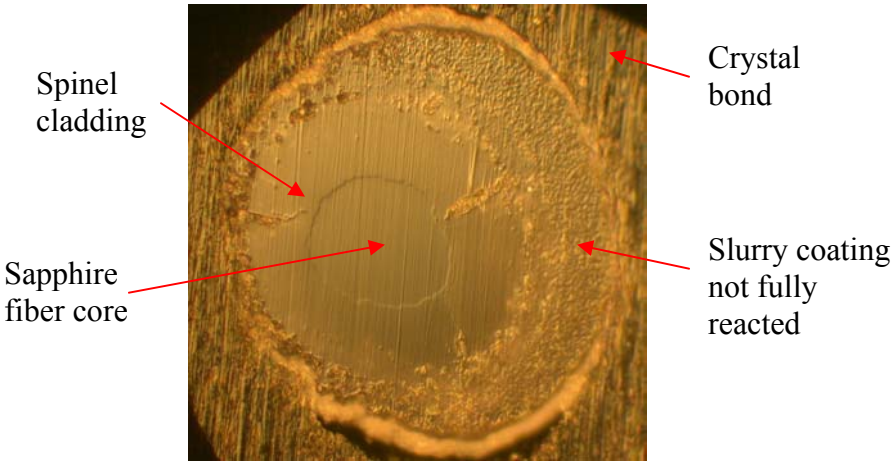

Figure 3-26. Sample 24z

To examine whether prolonged firing can further react the residuals, the same sample was fired again at 1600°C for additional 60 minutes. The heating and cooling rates are both 30°C per minute. The outcome of the second firing is shown in Figure 3-27. With a total of 90 minutes of sintering, the residuals left in sample 24z after the first firing seem mostly disappeared, but the core/cladding interface turns rougher. It is interesting to note that a detailed look at the core/cladding interface in Figure 3-27 reveals that the lower-

right portion of the interface, where the cladding is the thickest and is formed most recently after the second firing, is smoother than the interface at the upper-left portion. This portion of the interface has the thinnest cladding and was formed earlier in the first firing, and the second firing ruins the relatively smooth interface at this portion of the interface. This evidence enforces the assumption that rough core/cladding interface is caused by over-firing.

By comparing sample 14(17)s (Figure 3-21), 34x (Figure 3-23 and Figure 3-24), 24z (Figure 3-26 and Figure 3-27), in general, the degree of cracking in the samples prepared by nanopowders is less severe than that in the sample prepare by µm-sized powders.

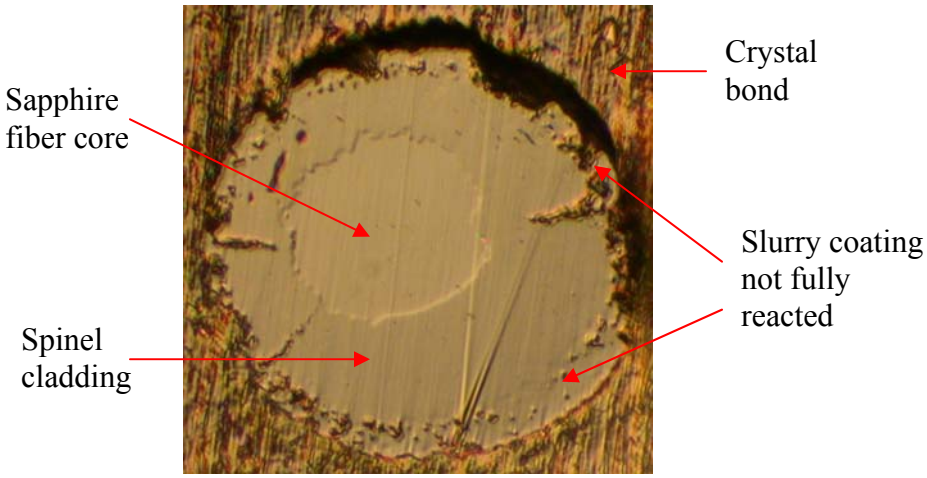

Figure 3-27. Sample 24 z after the second firing

3.2.2.1.3 The Second Attempt on Samples Prepared Using Nanopowders

A new type of nanopowders was used to prepare the following samples. The powders, NanoActive MgO Plus, from NanoScale have very large surface areas of 600 m^2/g and a very small crystalline size of 4 nm. However, the mean aggregate size is large, 12 µm, and there are visible carbon black contaminate particles in the powders. Both the MgO powders from NanoScale and the spinel powders from Alfa-Aesar were hand-ground for before use. The constituents of the slurry are listed in Table 3-7. The –solvents, binder, and plasticizer contents in this slurry batch, Nano-2.0, are very similar to those of sample 34x (Table 3-6), but the solid loading here is much larger, 19.3% verses 11.3%. The slurry was ball milled before being used to dip a fiber. Figure 3-28 illustrates the firing profile of this sample.

Table 3-7. Components of slurry batch Nano-2.0 (sample 30G)

Sample Name: 30G Slurry Batch: Nano-2.0			
	Components	Weight (g)	Weight %
Solvent 1	2-propanol	24.94	91.0
Solvent 2	1-ethoxy-2-peopanol	2.02	7.4
Binder	PVP (1.3M m.w.)	0.29	1.1
Plasticizer	Polyethylene glycol	0.14	0.5
Powders	MgO (NanoScale crystalline)	4.48	Total: 5.96
	$MgAl_2O_4$ (Alfa Aesar)	1.48	
Solid Loading = 5.96/(5.96+24.94)=19.3%			

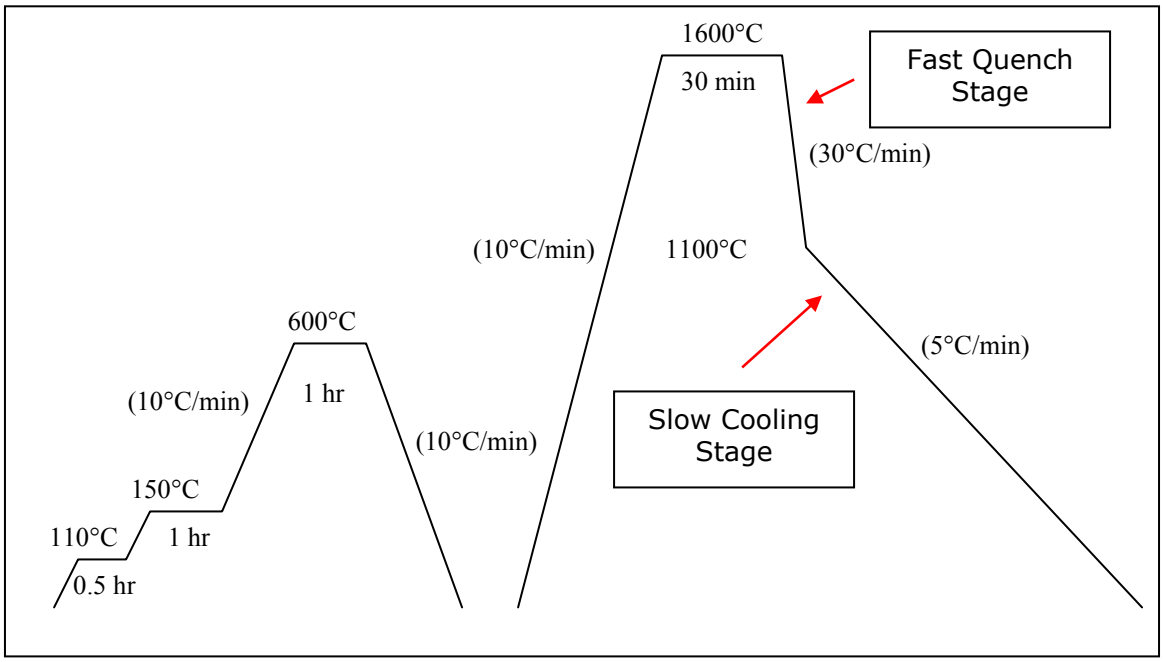

Figure 3-28. The firing profile of sample 30G

The heating rate to 1600°C was changed from 15°C per minutes to 10°C per minutes. The cross sections after fracture and after polishing and annealed are shown in Figure 3-29 and Figure 3-30 respectively. The sample was annealed at 1200°C for 3 hours. Sample 30G has a relatively smooth core/cladding interface and a relatively small amount of residuals not fully reacted. This hints that the heating profile illustrated in Figure 3-28 is close to what is needed to both fully react the slurry coating and to create a smooth core/cladding interface. But the clad fiber is quite fragile, and its surface on its sides is rough and uneven as shown in Figure 3-31. From now on the surfaces as well as the cross

sections morphologies are monitored. This roughness hints that the amounts of constituents in the slurry as tabulated in Table 3-7 are not optimized. Most likely the amount of binder is too little to hold the coating together in one uniform piece after drying. The fragility is caused by the significant amount of cracking in the cladding.

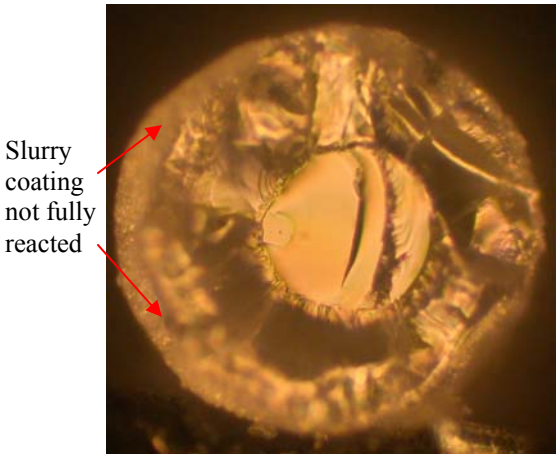

Figure 3-29. The fractured surface of cross section of sample 30G

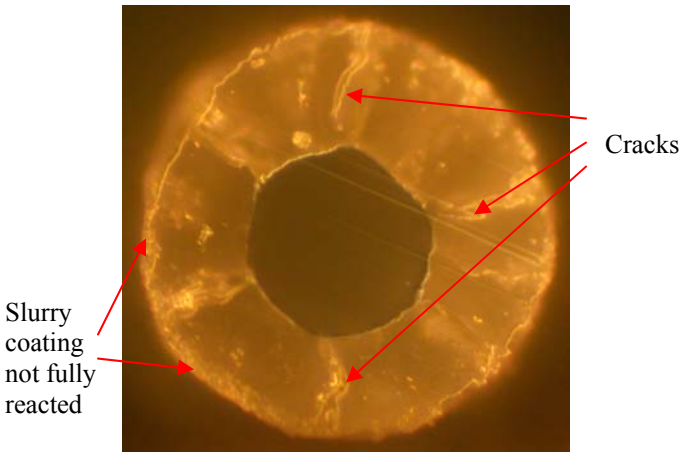

Figure 3-30. The polished and annealed sample 30G

Figure 3-31. The surface on the sides of sample 30G

Table 3-8. Components of slurry batch MgO-1.0 (sample 10H-4)

Sample Name: 10H-4 Slurry Batch: MgO-1.0			
	Components	Weight (g)	Weight %
Solvent 1	2-propanol	12.7	91.1
Solvent 2	1-ethoxy-2-peopanol	1.03	7.4
Binder	PVP (1.3M m.w.)	0.15	1.1
Plasticizer	Polyethylene glycol	0.06	0.4
Powders	MgO (NanoScale, crystalline)	2.47	Total: 2.47
Solid Loading = 2.47/(2.47+12.7)=16.3%			

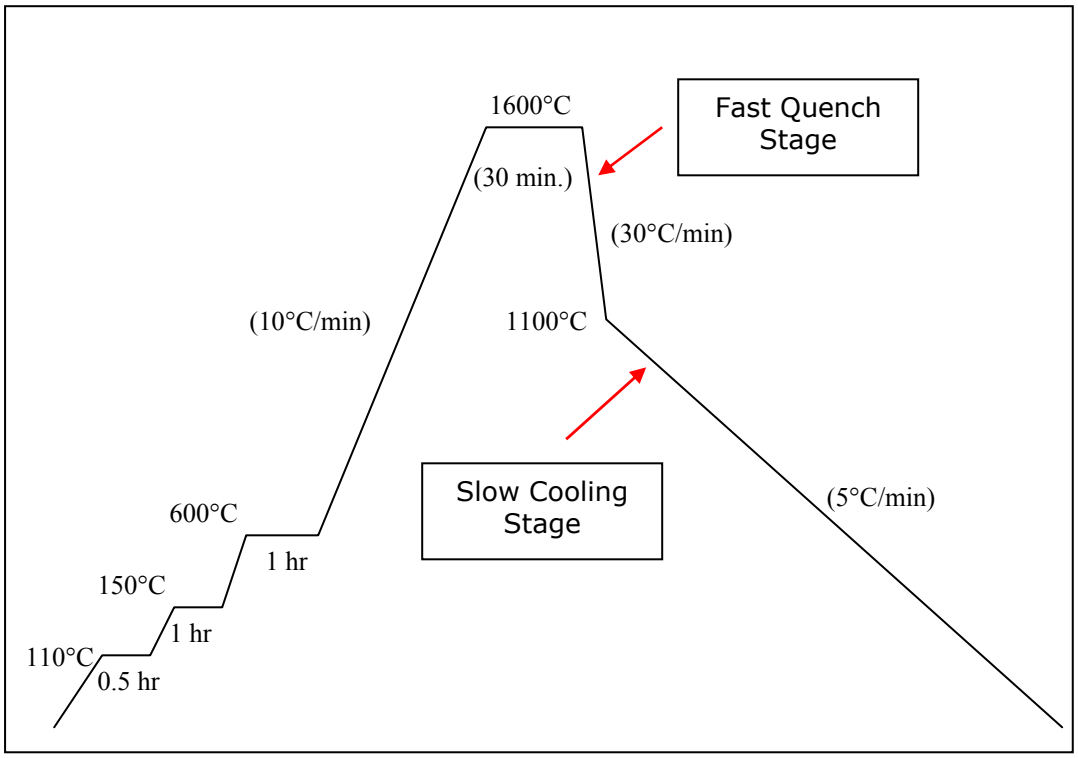

Figure 3-32. The firing profile of sample 10H-4

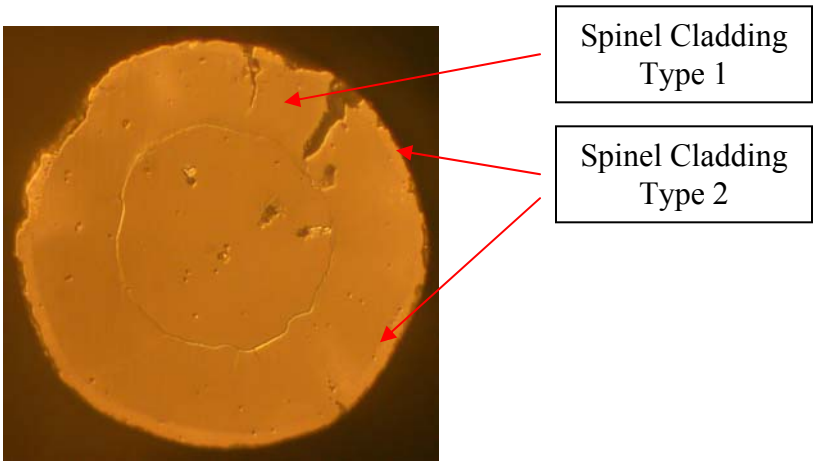

Figure 3-33. The polished and annealed cross section of sample 10H-4

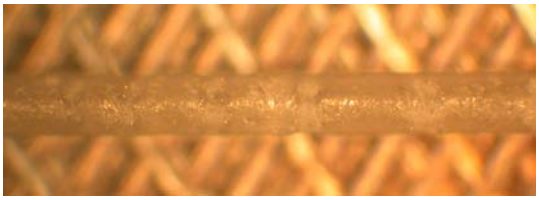

Figure 3-34. The surface on the sides of sample 10H-4

All the slurries used to dip the fibers up till now are prepared using a weight ratio of 3 to 1 between MgO and spinel powders. The spinel powders serve as nucleation centers to assist the nucleation of spinel grains when MgO interacts with the Al_2O_3 of sapphire fibers. It is suspected that, during firing, while the MgO powders in the coating diffuse towards the sapphire fiber, the spinel powders in the coating do not have as large a driving force to diffuse to the sapphire fiber as do the MgO powders, consequently resulting in residuals on fibers after firing. If the only role of spinel powders is to serve as nucleation centers, the powders should be required only at the coating/fiber interface, not within the bulk of the coating, since as long as the spinel grains are nucleated at the core/cladding interface, they can grow towards the center of fiber like columns without assistance of spinel powders in the bulk of the coating. To verify this assumption, an experiment was designed to use two batches of slurries to dip one single fiber. The first batch is the regular slurry consisting of both MgO and spinel powders, and the second batch has MgO powders only. The fiber was dipped using the first batch first, and then followed by the second batch. Only coating close to the core/cladding interface has spinel, not in the bulk of the coating. The constituents of the
MgO only slurry is listed in Table 3-8. The MgO powders were hand ground before mixing. The regular batch with both MgO and spinel powders is the same batch used to dip sample 30G, and the constituents of this batch, Nano-2.0, are listed in Table 3-7. The fiber, sample 10H-4, was dipped first with the regular slurry, and followed by the MgO only slurry. The firing profile is illustrated in Figure 3-32. An attempt was made to

combine the drying and binder burnout stage with the high temperature sintering stage. One concern is that usually binder needs oxygen for its burnout, and it is not sure at this moment whether PVP, the binder used in our experiments, can be successfully burned out. The polished and annealed cross section of sample 10H-4 is shown in Figure 3-33. The surfaces of the clad fiber on its sides are shown in Figure 3-34. As revealed by Figure 3-33, first, there are almost no residuals left on the surfaces of the clad fiber, and second, the cracking in the cladding is limited to only one large crack and one small crack in the upper-right portion of the cladding, and third, although the core/cladding interface is not perfectly concentric, it is quite clean and smooth. Furthermore, there are two types of distinctive cladding structures; the first type, Type 1 shown in Figure 3-33, occupies more than 90% of the cladding, and the second type, Type 1 in Figure 3-33, locates only at the surface of cladding, and is only 1/8 of the thickness of the first type. It is believed that the Type 1 cladding is formed by the inward diffusion of MgO from coating into fiber, while Type 2 cladding is formed by the outward diffusion of Al_2O_3 from fiber towards coating. It seems that the incorporation of all MgO coating can minimize the amount of residuals and the cracking in the cladding. The non-concentricity of the core/cladding interface may be caused by the non-uniformity of the MgO plus spinel coating thickness around the fiber or the non-uniformity of the powder packing density in the slurry.

The surfaces of sample 10H-4 on its sides are still rough, but they are much better than those of sample 30G shown in Figure 3-31. It is to be noted that one sign of an excessive amount of residuals is that the surface of the clad fiber looks white, in contrast to a fiber fully reacted that looks translucent. These results show promise of using this 2-batch dipping method to reduce residuals, cracking, and promote a smooth core/cladding interface.

3.2.2.1.4 Summary of the results of the samples prepared using nanopowders

1. With similar slurry compositions and firing profiles, the samples prepared by nanopowders have more residuals on the fiber after firing, and the core/cladding interfaces of these samples are rougher and more irregular than those of the samples prepared using μm-range powders. It is suspected that the slurry composition, which is optimal for the μm-range powders, is not feasible for nanopowders.
2. In order to achieve the largest possible packing density and its uniformity in the coating, the powder sizes, their distributions, and the perfect dispersion of the powders in slurry are critically important.
3. The nanopowder slurry prepared using the existing composition is not stable as a function of time, even when the slurry is stirred constantly after preparation. The samples prepared using aged slurry have a lot of residuals not fully reacted after firing. It is suspected that the degree of agglomeration of powders in the slurry may be slowly increasing, thus resulting in even poorer packing density after drying.

4. Rough core/cladding interface may be caused by either over-firing or sparse and tenuous coating structures.
5. The degree of cracking in the samples prepared by nanopowders seems to be less severe than that in the sample prepare by μm-sized powders.
6. Judging from the rough and uneven surface morphology in some of the samples, the current amount of binder may not be enough to hold the coating together in one uniform piece after drying.
7. Slurry coating consisting of an undercoat made of MgO and spinel to help spinel nucleation at the core/cladding interface, and of MgO only topcoat, shown promise of reducing residuals, cracking, and promote a smooth core/cladding interface after firing.

3.2.2.2 The use of powders with different sizes to improve packing density

When spheres of different sizes are mixed together, the packing density depends on the size distributions of the spheres and their weight fractions. The greatest possible packing density of spheres with the optimized size distributions and weight fractions can be calculated according to the model of mixed solid spheres. The results are shown in Table 3-9. With spheres of only one size, the calculated packing density is 60.5%. The introduction of spheres 8.3 times smaller with a weight fraction of 27.4% can increase the packing density to 84.8%. The further introduction of spheres 5.5 times smaller than the ones just introduced, with a weight fraction of 20.9%, can boost the packing density further to 95.2%. Attempts were made to blend 4 types of powders, MgO (EM Science), spinel (Baikalox), spinel (Alfa Aesar), and MgO (Aldrich) in the slurry to improve the clad fiber properties. Different techniques have been used to measure the particle sizes of the above powders. The results will be discussed later.

Table 3-9. Packing density of mixed spheres of different sizes[9]

Diameter (cm) (weight fraction of spheres)				Packing Density (%)	
1.28	0.155	0.028	0.004	Calculated	Experimental
1.000	—	—	—	60.5	58.0
0.726	0.274	—	—	84.8	80.0
0.647	0.244	0.109	—	95.2	89.8
0.607	0.230	0.102	0.061	97.5	95.1

Source: R.K. McGeary, *J. Am. Ceram. Soc.* **44**(10), 513–522 (1961).
Size ratio 320/39/7/1.

[9] R. K. Mcgeary, J. Am. Ceram. Soc., 44(10), 1962. p.513-522.

3.2.2.3 The Implementation of Two Stage Milling: Dispersion Milling and Binder Milling

For all the slurries prepared to this point, the solvents, binder, plasticizer, and the powders were all mixed and milled simultaneously. It was discovered from the literature that it is difficult to achieve the highest degree of powder dispersion in the slurry this way. The slurry should be prepared in two stages: dispersion milling stage and binder milling stage.[10] In dispersion milling only the solvent(s), powders, and a dispersant/deflocculant are added, but not binder. Binder competes with dispersant in occupying the surface sites of powders, thus reducing the effectiveness of the dispersants added. Only after thorough powder dispersion after dispersion milling is binder added in order to hold the green body together. The two-step milling will be implemented in all slurry preparation from now on.

3.2.2.4 Use of polyethylene glycol as the dispersant

In all the slurries prepared so far, polyethylene glycol is identified as plasticizer, which makes the coating plastic and deformable after drying by shortening or partially dissolving the polymer chains of the binder. The current binder used in our experiments is PVP with a molecular weight of 1,300,000. From Table 3-10, polyethylene glycol can also be used as dispersant. With the introduction of dispersion milling stage, a proper dispersant is needed in our slurry system. According to Table 3-10, polyethylene glycol will be used as the dispersant in the following samples.

Table 3-10. Some reported dispersants/deflocculants[11]

Some Reported Dispersants/Deflocculants used for Tape Casting	
Polyisobutylene[48]	pH adjustments
Linoleic acid[48]	Sodium silicate
Oleic acid	Dibutyl amine
Citric acid	Substituted imidazolines[47]
Stearic acid	Sulfanates
Lanolin fatty acids[47]	Aliphatic hydrocarbons[47]
Salts of polyacrylic acids	2-amino-2-methyl-1-propanol[47]
Salts of methacrylic acids	Polyethylene glycol[47]
Blown menhaden fish oil	Polyvinyl butyral[47]
Corn oil	Sodium sulfosuccinates[47]
Safflower oil	Ethoxylate[47]
Linseed oil	Phosphate ester[47]
Glycerol trioleate	Glycerol tristearate
Synthetic waxy esters	Many proprietary chemicals

[10] Richard E. Mistler and Eric R. Twiname, "Tape Casting, Theory and Practice", The American Ceramic Society, Westerville, OH, 2000, p.27.

3.2.2.5 Samples prepared using four types of powders and polyethylene glycol as dispersant

Four types of powders were used to prepare the slurry: MgO (EM Science), spinel (Baikalox), spinel (Alfa Aesar), and MgO (Aldrich). All powders, except MgO from Aldrich, were hand-ground in 2-propanol followed by ball milling. The dispersant, polyethylene glycol, was mixed with the solvent, 2-propanol to prevent solvent evaporation. The finest powder, MgO from Aldrich, were first added into the beaker, followed by the spinel from Alfa Aesar, the spinel from Baikalox, and finally by the MgO from EM Science. Between each powder addition step, the bottle is hand-shaken to disperse the powders in the slurry. The dispersant slurry was then ball milled in the bottle.

The PVP binder can have different molecular weight depending on its chain length. Besides the 1,300,000 molecular weight PVP that has been used so far, the 10,000 molecular weight PVP was also available for evaluation at this moment. After dispersion milling binders were added to the slurry in the sequence listed in Table 3-11. The viscosity of slurry was significantly smaller after 0.33g 10k binder was added compared to the slurries where the 1.3m binder was used. More binders were added to increase slurry viscosity. The reason for separating the addition of binders is to prevent them from sticking together as a lump in the slurry. The rationale for increasing the viscosity is to increase the coating thickness after each dipping, thus reducing the number of dips needed to obtain a certain spinel coating thickness; for slurry in the Newtonian region, the coating thickness from each dipping is proportional to both slurry viscosity and dipping speed.[11]

Table 3-11. Binder addition sequence for sample 80Q

Sequence of addition	binder	Molecular weight (g)	Weigh added (g)	Ball milling time after binder addition (hour)
1	PVP	10k	0.33	1.3
2	PVP	10k	1.84	1.25
3	PVP	10k	0.10	1.0
		1.3m	2.40	

Because of the different binder burnout temperatures for binders with different molecular weights, it is common to mix these binders together to reduce the impact of binder burnout on the green body structure. The final constituents of the slurry are shown in Table 3-12. Polyethylene glycol is used here as both dispersant and plasticizer. The

[11] Huang, Yuhong; Zheng, Haixing; and Forsyth, Ian, "Application of Functional Ceramic and Hybrid Nanostructure Coating Fabrication via Sol-Gel Processes," Fine, Ultrafine and Nano Powders 2000, Oct. 29-31, 2000, Montreal, Canada.

weight fraction of each powder was determined roughly according to the mixed sphere models illustrated in Table 3-9. The reason for not being able to determine the exact weight fractions at this moment is that the accurate particle sizes of each powder have not been independently measured. Furthermore, the weight ratio between MgO and spinel powders has to be 3 to 1, and this limits the ability to exactly follow the guideline listed in Table 3-9. Even with the huge amount of binder added, 6.3 w. % 10k binder and 6.9 w. % 1.3m binder, the viscosity was still relatively small.

This small viscosity implies that two-stage milling is critically important in the thorough dispersion of powders. When powders in a solution are badly dispersed, the powders form large agglomerates with large voids among them filled with solvents. These large agglomerates are difficult to pass one another when the slurry flows, thus increasing the slurry viscosity. On the other hand, if the powders are finely dispersed, it is easier for them to pass each other in the slurry, resulting in small viscosity. Another factor influencing viscosity is solid loading: in general, the larger the solid loading, the larger is the viscosity. After taking into account the solid loading of sample 80Q, 14.2%, and those of the previous samples discussed earlier, 12.1% for sample 14(17)s, 11.4% for sample 34x, 19.3% for sample 30G, 16.3% for sample 10H-4, it is still very impressive that the viscosity of the slurry for sample 80Q is significantly smaller than those of all other samples.

A fiber, sample 80Q, was dipped using this slurry. The firing profiles are illustrated in Figure 3-35. There are two minor adjustments on the firing profiles. First, the heating and cooling rates in the drying and binder burnout were reduced from 10°C per minute to 5°C per minute. The purpose for this change is to improve the structural integrity of the coating by decreasing the water and binder removal rates from coating. Second, the rapid quenching from 1600°C to 1100°C was changed to from 1600°C to 1200°C. From the previous results stated in the first semiannual report, a prolonged annealing at 1200°C has no detrimental effects on the core/cladding smoothness of sample 14(17)s. Therefore, it is harmless to start the slow cooling stage from 1200°C instead of 1100°C. The intention here is to lower the temperature drop in the fast quench stage from 500°C to 400°C, in order to minimize the thermal stresses developed due to the different thermal expansion coefficients of sapphire and spinel.

Table 3-12. Constituents of slurry batch Blend-2.0 (sample 80Q)

Sample Name: 80Q Slurry Batch: Blend-2.0			
	Components	Weight (g)	Weight %
Solvent 1	2-propanol	27.33	78.6
Solvent 2	1-ethoxy-2-peopanol	2.56	7.4
Dispersant	Polyethylene glycol	0.12	0.3
Binder	PVP (10k m.w.)	2.27	6.5
	PVP (1.3m m.w.)	2.4	6.9
			13.4
Plasticizer	Polyethylene glycol	0.11	0.3
Powders (Total: 4.54)	MgO (EM Science)	2.72	59.9
	MgO (Aldrich)	0.64	14.1
	Spinel (Baikalox)	1.09	24.0
	Spinel (Alfa Aesar)	0.09	2.0
Solid Loading = 4.54/(27.33+4.54)=14.2%			

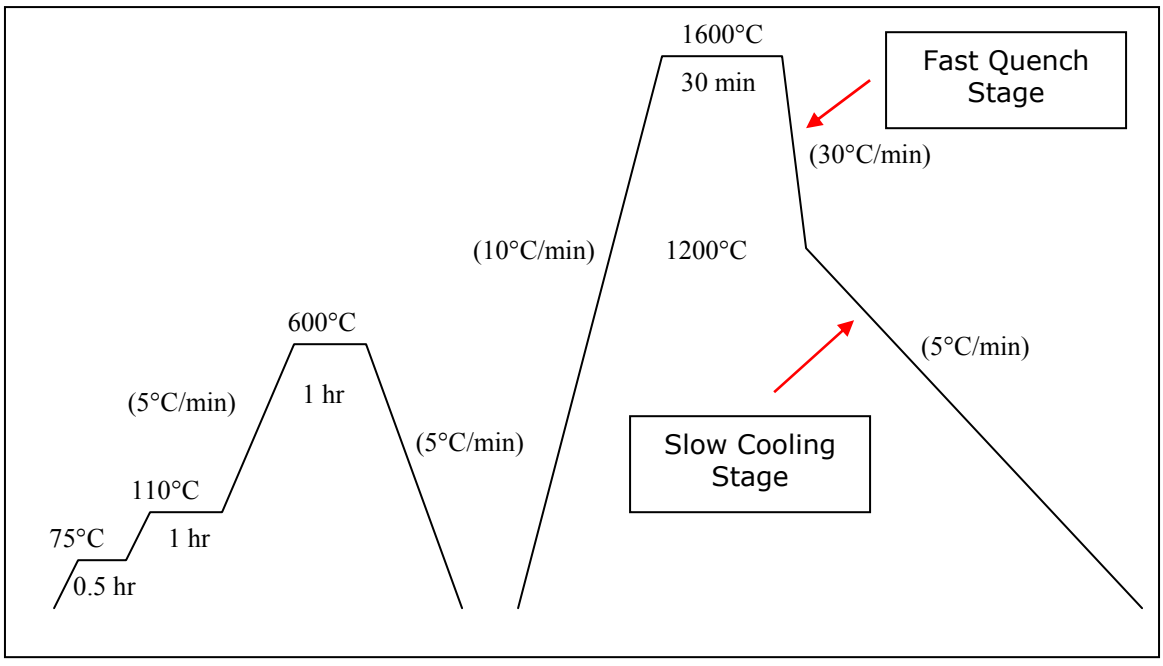

Figure 3-35. The firing Profile of sample 80Q

The annealed cross section of sample 80Q is shown in Figure 3-36, and the surfaces of the sample on its sides are shown in Figure 3-37. The spinel cladding is still thin, because of the small slurry viscosity compared to those of previous slurries. The cladding thickness is relatively uniform with some cracks in it. The core/cladding interface seems to consists of small and shinny grains that thicken the interface. There is only a very thin layer of residuals on the cladding surface. The surfaces on the sides of the sample look quite smooth and uniform without steps and cracks, possible owing to the profound amounts of binders added that are capable of holding the coating together after drying.

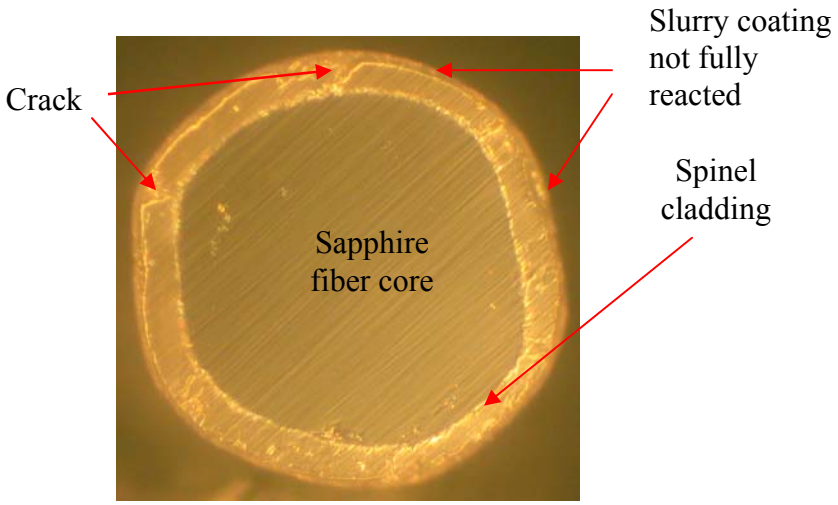

Figure 3-36. The annealed cross section of sample 80Q

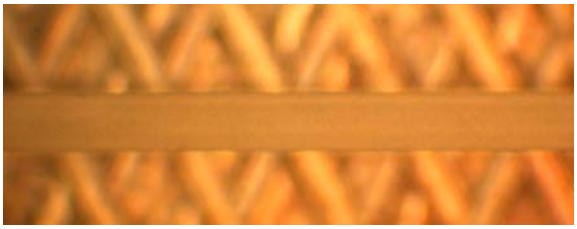

Figure 3-37. The surfaces on the sides of sample 80Q

To examine further the effect of binder, 0.16 g of 1.3m PVP was added to the slurry, followed by ball milling, and then a fiber, 100R, was dipped. The dipping was performed one day after the firing of sample 80Q. The constituents of the slurry are listed in Table 3-13. Here the amount of 1.3m PVP binder is 0.4 w. % more than that of sample 80Q. The firing profiles of sample 100R were exactly the same as those of sample 80Q. The annealed cross section of sample 80Q is shown in Figure 3-38, and the surfaces of the sample on its sides in Figure 3-39. As can be seen in Figure 3-38, the cladding thickness is extremely not uniform, and the interface is wavy and out of concentricity. But the amount of residuals on cladding is also small. There are some cracks in the cladding, yet their widths are very small, which indicates superior mechanical strength of the cladding.

The surfaces on the sides of the fiber are not as smooth and as uniform compared to those of sample 80Q. It is suspected that the high molecular weight binder was not dissolved thoroughly and homogeneously in the slurry, thus resulting in large cladding thickness variation and roughness on the fiber surface. It is also believed that it is not a good practice to add high molecular weight binder sequentially in larger amounts, because the binders are difficult to dissolve this ways.

Table 3-13. Constituents of the slurry batch Blend-2.1 (sample 100R)

Sample Name: 100R Slurry Batch: Blend-2.1				
	Components	Weight (g)	Weight %	
Solvent 1	2-propanol	27.33	78.2	
Solvent 2	1-ethoxy-2-peopanol	2.56	7.3	
Dispersant	Polyethylene glycol	0.12	0.3	
Binder	PVP (10k m.w.)	2.27	6.5	13.8
	PVP (1.3m m.w.)	2.56	7.3	
Plasticizer	Polyethylene glycol	0.11	0.3	

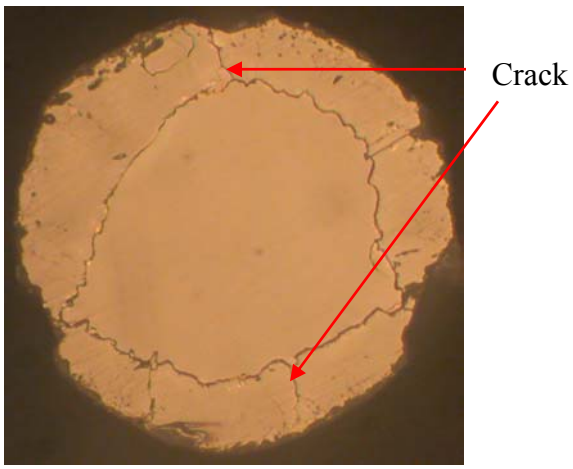

Figure 3-38. The annealed cross section of sample 100R

Figure 3-39. The surfaces on the sides of sample 100R

Additional 0.17 g of 1.3m PVP binder was added to the slurry, followed by ball milling. Another fiber, sample 80S, was dipped. This was one day after the firing of sample 100R. The constituents of the slurry are listed in Table 3-14. The firing profiles of sample 80S were exactly the same as those of sample 80Q, except that the dwelling time at 1600°C was reduced from 30 minutes to 15 minutes. The goal of this change is to reduce the roughness at the core/cladding interface. The annealed cross section of sample 80Q is shown in Figure 3-40, and the surfaces of the sample on its sides in Figure 3-41. Here the results are similar to those of sample 100R: irregular cladding thickness and rough core/cladding interface, apart from that the interface is widened by shinny grains. There are little residuals on cladding surface, and there seems to be only one large crack.

Table 3-14. Constituents of the slurry batch Blend-2.2 (sample 80S)

Sample Name: 80S Slurry Batch: Blend-2.2				
	Components	Weight (g)	Weight %	
Solvent 1	2-propanol	27.33	77.8	
Solvent 2	1-ethoxy-2-peopanol	2.56	7.3	
Dispersant	Polyethylene glycol	0.12	0.3	
Binder	PVP (10k m.w.)	2.27	6.5	14.3
	PVP (1.3m m.w.)	2.73	7.8	
Plasticizer	Polyethylene glycol	0.11	0.3	

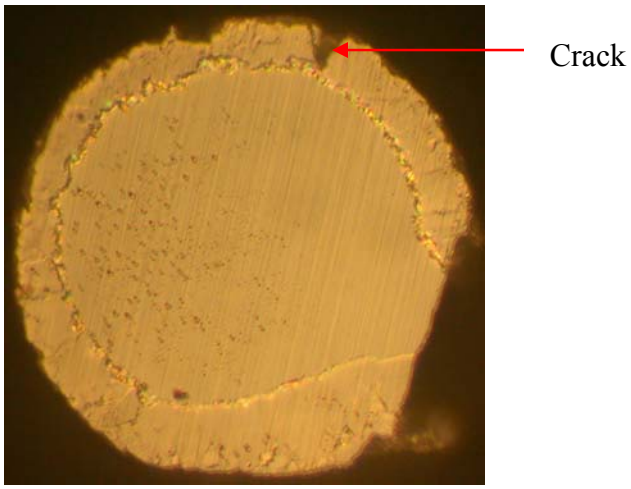

Figure 3-40. The annealed cross section of sample 80S

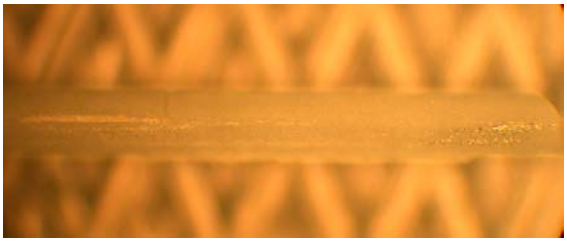

Figure 3-41. The surfaces on the sides of sample 80S

To examine the effect of low molecular weight PVP binder, additional 0.34g of 10k PVP binder was added to the slurry. The slurry was ball milled before dipping. Another fiber, sample 80T, was dipped. The dipping was performed one day after the firing of sample 80S. The constituents of the slurry are listed in Table 3-15. The w. % of 10k PVP, 7.4 %, is again comparable to that of 1.3m PVP, 7.7%. The firing profiles of sample 80T were exactly the same as those of sample 80S. The annealed cross section of sample 80T is shown in Figure 3-42, and the surfaces of the sample on its sides in Figure 3-43. There are a lot of cracks in the cladding; however, the cladding thickness seems to be relatively uniform again. Although the core/cladding interface is still rough, shinny, and granular, yet some portions of the interface are significantly smooth. There are minimal amount of residuals on fiber surface. It seems that the reduction of sintering temperature from 1600°C to 1550°C increase the likelihood of a smooth core/cladding interface. It also appears that the addition of 10k PVP can slightly improve the cladding thickness uniformity and cladding surface smoothness.

Table 3-15. Constituents of the slurry batch Blend-2.3 (sample 80T)

Sample Name: 80T Slurry Batch: Blend-2.3				
	Components	Weight (g)	Weight %	
Solvent 1	2-propanol	27.33	77.1	
Solvent 2	1-ethoxy-2-peopanol	2.56	7.2	
Dispersant	Polyethylene glycol	0.12	0.3	
Binder	PVP (10k m.w.)	2.61	7.4	15.1
	PVP (1.3m m.w.)	2.73	7.7	
Plasticizer	Polyethylene glycol	0.11	0.3	

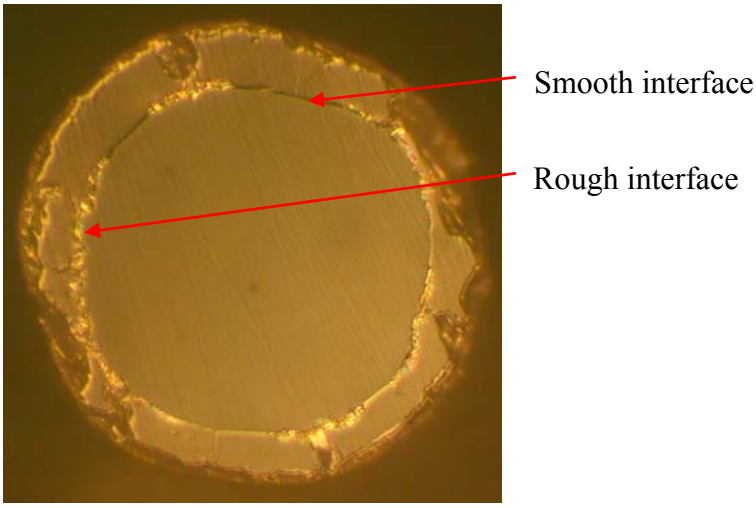

Figure 3-42. The annealed cross section of sample 100R

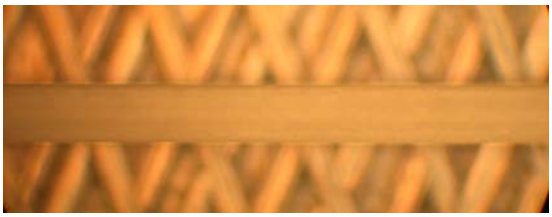

Figure 3-43. The surfaces on the sides of sample 100R

Another fresh batch of slurry blended with four types of powders and dispersed using polyethylene glycol was prepared. One new step in powder preparation was implemented: all powders were dried at 500°C for at least 1 hour before adding to the slurry batch. The goal for this step is to removal the chemically absorbed water on powders, especially on the nanopowders from Aldrich. The slurry was milled with polyethylene glycol as the dispersant in a 4-oz polypropylene bottle half filled with grinding media. The constituents of the slurry are listed in Table 3-16. The powder weight fractions here are the same as those of sample 80Q listed in Table 3-12, but the powder loading was increased from 14.2% to 19.9%, in order to increase the slurry viscosity. The major change in slurry preparation is that only 10k PVP binder was used in order to maintain slurry uniformity. There was no polyethylene glycol added in the binder milling stage as a plasticizer, since the molecular weight of 10k PVP binder is very small by itself, thus there was no need to break down the carbon chains any further.

Table 3-16. Constituents of the slurry batch Blend-3.0 (sample 80V)

Sample Name: 80V Slurry Batch: Blend-3.0			
	Components	Weight (g)	Weight %
Solvent 1	2-propanol	18.18	82.9
Solvent 2	1-ethoxy-2-peopanol	1.43	6.5
Dispersant	Polyethylene glycol	0.19	0.9
Binder	PVP (10k m.w.)	2.13	9.7
Plasticizer	Polyethylene glycol	0	0
Powders (Total: 4.54)	MgO (EM Science)	2.69	59.4
	MgO (Aldrich)	0.67	14.8
	Spinel (Baikalox)	1.07	23.6
	Spinel (Alfa Aesar)	0.10	2.2
Solid Loading = 4.53/(18.18+4.53)=19.9%			

The binder was added in a small amount, about 0.2g, at a time, followed by hand shaking the bottle to dissolve the binder. An interesting phenomenon was observed in this process. The viscosity of slurry, as a result of binder addition, instead of increasing, surprisingly decreases when the binder was added. The viscosity keeps on decreasing until a total of 0.8g of binder was added, and it starts to slowly increase after that. The same phenomenon must have occurred during the slurry preparation for sample 80Q, but it was overlooked at that time. It is believed that the low molecular weight PVP was, in fact, serves as a dispersant rather than a binder here. After each binder addition step, one drop of the slurry was let dried on a microscope glass slide, and the pattern of the dried slurry surface was observed. A network of cracks appeared after a few minutes when the slurry is dry. After a total of 2.13g of binder has been added, the surface cracks ceased to appear on the dried slurry surface. The slurry was binder milled and a fiber, sample 80V, was dipped using this slurry. The firing profiles are shown in Figure 3-44. Here the sintering temperature was reduced to 1550°C in order to lessen the core/cladding interface roughness. The temperature drop in the fast quench stage was also reduced to 250°C with a target temperature of 1300°C instead of 1200°C; the purpose is to minimize the thermal stresses developed during this stage.

The annealed cross section of sample 80T is shown in Figure 3-45, and the surfaces of the sample on its sides in Figure 3-46. The spinel cladding is still relatively thin; the diameter of sapphire fiber is reduced from 150μm to 125μm. The core/cladding interface is both concentric and smooth. There are cracks in the hexagonally symmetrical directions, yet their widths are small, indicating that the degree of cracking is constrained. The residuals on cladding surface are minimal. The fiber surface as seen in Figure 3-46 is both smooth and uniform.

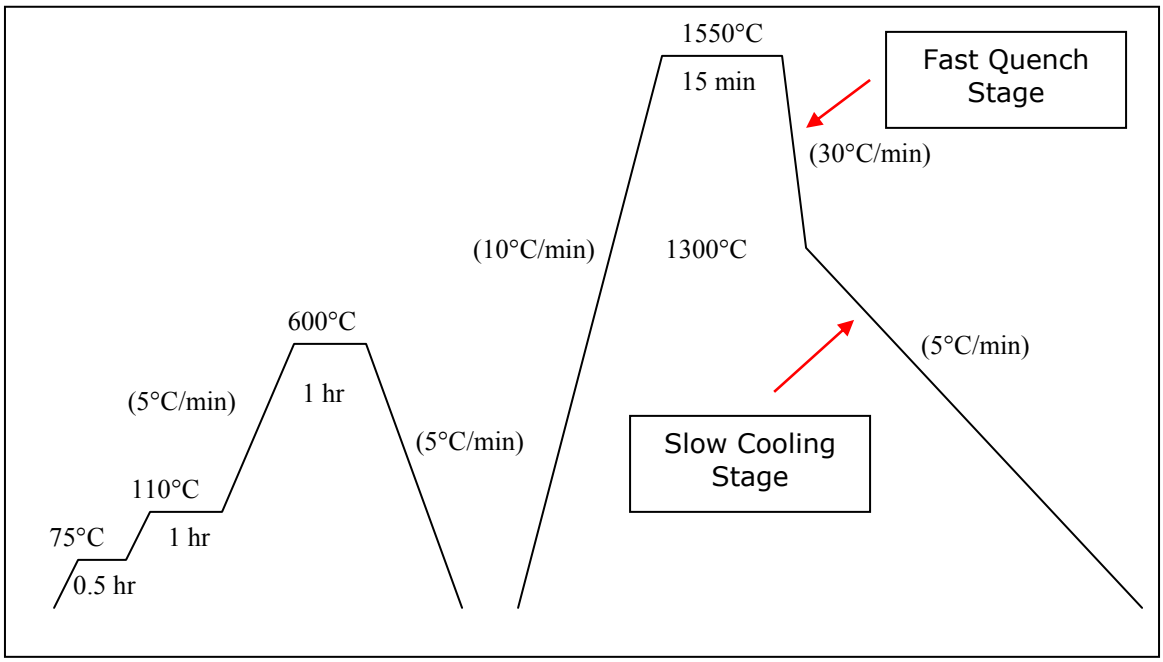

Figure 3-44. The firing profile of sample 80V

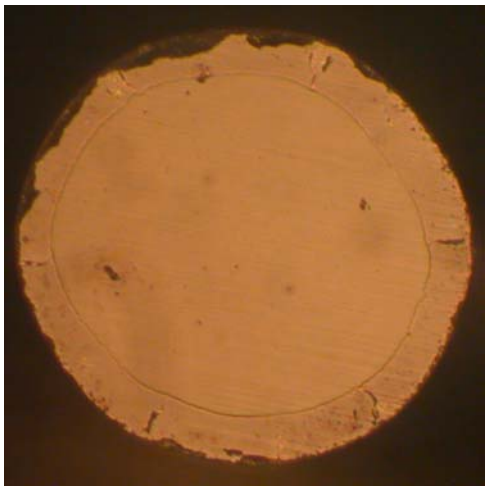

Figure 3-45. The annealed cross section of sample 80V

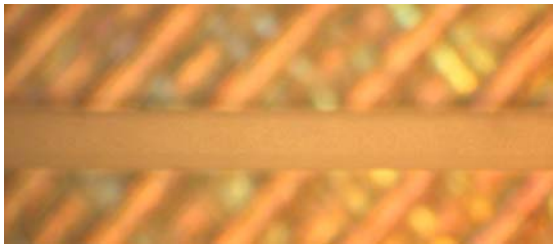

Figure 3-46. The surfaces on the sides of sample 80V

In order to increase the cladding thickness, 0.1 g of 1.3m PVP binder was added to the slurry to increase its viscosity. The slurry was then ball milled. The composition of the slurry is listed in Table 3-17. Here the 1.3m PVP binder is only a very small fraction of the 10k PVP. A fiber, sample 70W, was dipped using this slurry. The dipping was performed one day after sample 80V. The annealed cross section of sample 70W is shown in Figure 3-47, and the surfaces of the sample on its sides in Figure 3-48. Here the spinel cladding is much thicker than that of sample 80V. The cladding thickness is relatively uniform, and the core/cladding interface is concentric and relatively smooth. There are some fine cracks and a lot of voids in the cladding, presumably caused by the 1.3m PVP binder not thoroughly and uniformly dissolved in the slurry.

Table 3-17. Constituents of the slurry batch Blend-3.1 (sample 70W)

Sample Name: 70W Slurry Batch: Blend-3.1				
	Components	Weight (g)	Weight %	
Solvent 1	2-propanol	18.18	82.5	
Solvent 2	1-ethoxy-2-peopanol	1.43	6.5	
Dispersant	Polyethylene glycol	0.12	0.9	
Binder	PVP (10k m.w.)	2.13	9.7	10.2
	PVP (1.3m m.w.)	0.1	0.5	
Plasticizer	Polyethylene glycol	0	0	

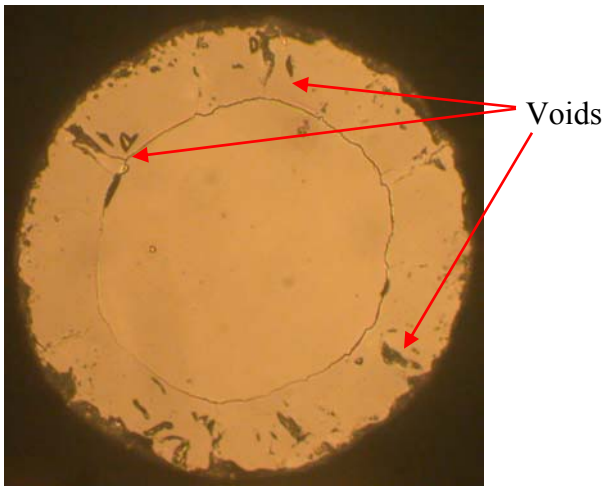

Figure 3-47. The annealed cross section of sample 70W

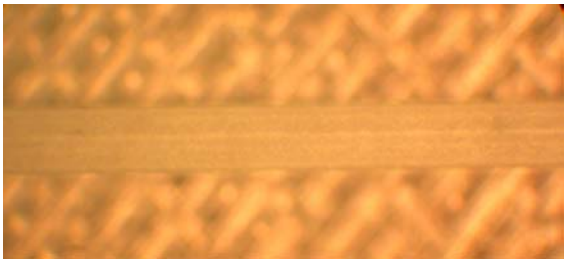

Figure 3-48. The surfaces on the sides of sample 70W

One thing worthy of noting is that the viscosity of the slurry batch Blend-3.1 increases drastically 3 days after being stored in the polypropylene bottle. The slurry looks all gelled together with the grinding media dispersed in it. This hints that the slurry with the current compositions is not stable as a function of time, which could create problems in the repeatability and consistency of the slurry behavior. A varied degree of gelation also appears in many other batches. It is suspected that the combination of polyethylene glycol as a dispersant and PVP as binder is still not suitable.

A fresh batch was prepared using a little more percentage of polyethylene glycol, 1.4 w. %, a lot less both the 10k and 1.3m PVP binder, a total of 1.0 w. %, and a lot higher solid loading, 24.3%. The slurry viscosity was extremely high after dispersion milling, not suitable for dipping. It is assumed that the current slurry composition is not ideal for a relatively high solid loading of 14.3%, thus resulting in very high viscosity, an indication of poor powder dispersion. It is also possible that after a certain maximum solid loading, the viscosity starts to drastically increase regardless a well designed slurry composition.

Table 3-18. Constituents of the slurry batch Blend-3.2

Slurry Batch: Blend-3.2				
	Components	Weight (g)	Weight %	
Solvent 1	2-propanol	28.29	93.1	
Solvent 2	1-ethoxy-2-peopanol	1.4	4.6	
Dispersant	Polyethylene glycol	0.44	1.4	
Binder	PVP (10k m.w.)	0.27	0.9	1.0
	PVP (1.3m m.w.)	0.04	0.1	
Plasticizer	Polyethylene glycol	0	0	
Powders (Total: 9.1)	MgO (EM Science,15µm)	5.38	59.9	
	MgO (Aldrich, 0.013µm)	1.33	14.1	
	Spinel (Baikalox, 3µm)	2.15	24.0	
	Spinel (Alfa Aesar, <1µm)	0.24	2.0	
Solid Loading = 9.1/(28.3+9.1)=24.3%				

Efforts were made to reproduce the sample 80V, but with thicker cladding. All powders were dried at 500°C for 3 hours. First, 2-propanol was mixed with polyethylene glycol in a 150cc beaker. Powders were added to the beaker in the sequence of increasing powder sizes: stating with the powders with the smallest sizes, MgO nanopowders, and ending with the powders with the largest sizes, MgO powders from EM Science. In between each powder addition the slurry was stirred for two minutes to disperse the powders. The slurry was then poured into a 4-oz polypropylene bottle half filed with grinding media. The bottle was then hand shaken followed by ball milling. The binder was added to the slurry in the bottle in a unit of about 0.2g at a time, followed by hand-shaking the bottle for 30 seconds. The slurry after binder addition was then ball milled. The slurry composition is listed in Table 3-19. This slurry composition is almost the same as that of sample 80V. The firing profiles are illustrated in Figure 3-49. Except for the 500°C binder burnout temperature, and the 2°C per minute cooling rate, the profiles are exactly the same as those of sample 80V. A fiber, sample 200hh, was dipped. It was realized during the fiber dipping that if ethanol, instead of 2-propanol, was used to clean the original sapphire fiber surface, the coating formed would not be uniform. The annealed cross section of sample 17ee is shown in Figure 3-50, and the surfaces of the sample on its sides in Figure 3-51. As shown in Figure 3-50, the cladding thickness is quite uniform; the core/cladding interface is both smooth and concentric. There are a few very thin cracks in the cladding, and there are also some residuals on the cladding surface. However, this clad fiber has already shown considerable improvement. The sapphire fiber core was reduced from 150μm to 105μm with light-guiding spinel cladding.

Table 3-19. Constituents of the slurry batch Blend-4.0

Sample Name: 200hh Slurry Batch: Blend-4.0			
	Components	Weight (g)	Weight %
Solvent 1	2-propanol	18.29	82.8
Solvent 2	1-ethoxy-2-peopanol	1.44	6.5
Dispersant	Polyethylene glycol	0.19	0.8
Binder	PVP (10k m.w.)	2.18	9.9
Plasticizer	Polyethylene glycol	0	0
Powders (Total: 4.55)	MgO (EM Science)	2.70	59.3
	MgO (Aldrich)	0.68	14.9
	Spinel (Baikalox)	1.07	23.5
	Spinel (Alfa Aesar)	0.10	2.2
Solid Loading = 4.55/(18.29+4.55)=19.9%			

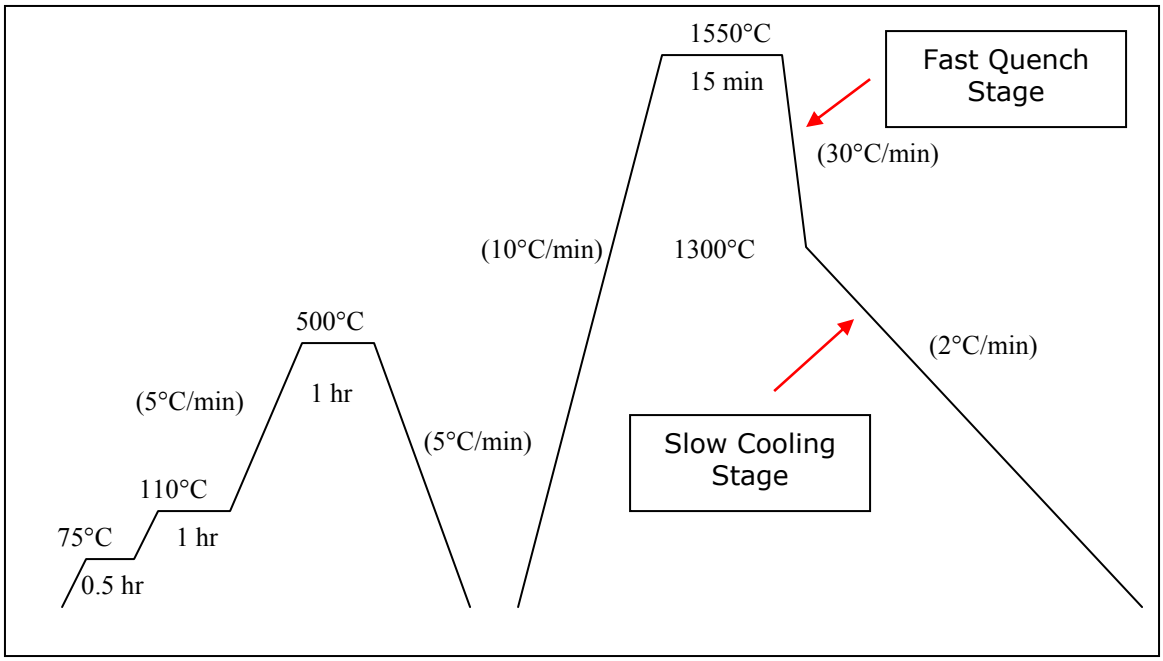

Figure 3-49. The firing profile of sample 200hh

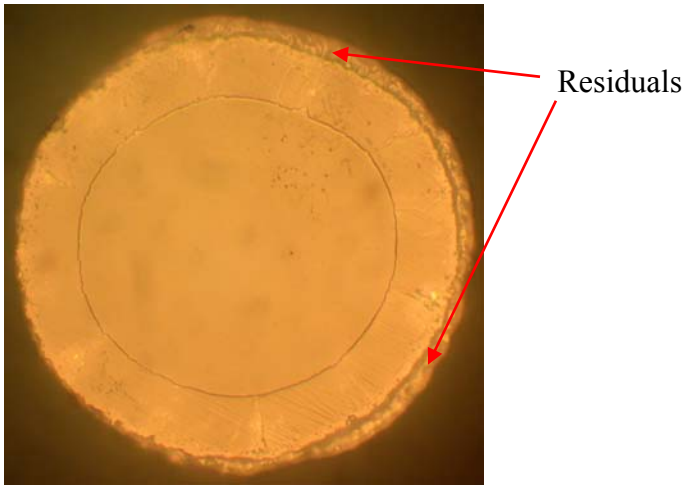

Figure 3-50. The annealed cross section of sample 200hh

Figure 3-51. The surfaces on the sides of sample 200hh

3.2.2.6 Test Menhaden Fish Oil as a Dispersant

Efforts were made to explore different types of dispersant, such as those shown in Table 3-10. Three dispersant candidates, oleic acid, stearic acid, and citric acid, were excluded first, because that after these chemicals were mixed with 2-proponal and ceramic powders, the viscosity of the slurries was very high, and the slurries even gelled together in some cases. The common aqueous dispersant sodium polyacrylate (Darvan 811 from R.T Vanderbilt Company, Inc., Norwalk, CT) was also eliminated because of the 50% water content in the dispersant. Finally, three candidates were chosen for further exploration, Menhaden fish oil (Aldrich), phosphate ester (Triton QS-44 surfactant from The Dow Chemical Company, Midland, MI), and CoatOsil 1211 coating additive from GE Silicones, Friendly, WV). Slurries prepared using these chemicals have reasonably small viscosity. The particle sizes of powders dispersed in these chemicals were measured using variety of techniques; the results will be discussed later. In this section two samples prepared using Menhaden fish oil as dispersant will be discussed.

Several batches of slurry with a range of composition were prepared to examine the effect of Menhaden fish oil as dispersant. The results of one of the batches are discussed here. In dispersant milling stage, Menhaden fish oil was first dissolved in 2-propanol, and the powders were added sequentially starting from the finest MgO powders from Aldrich, and ending with the coarsest powders from EM Science. All powders were dried at 400 °C for several hours and the slurry was ball milled. Afterward, the 10k PVP binder, 1-ethoxy-2-peopanol, and polyethylene glycol were added to the slurry. The slurry composition is shown in Table 3-20. Here the PVP binder amount is significantly smaller, and that of 1-ethoxy-2-peopanol for solvent evaporation control is considerably larger. The solid loading is comparable to those of other slurry batches. The slurry was quite thick after binder milling. It is believed that the large viscosity is caused by imperfect powder dispersion in the slurry. A fiber, sample 17ee, was dipped using this slurry. The coating surface after dipping is not smooth. The firing profiles are illustrated in Figure 3-52. The annealed cross section of sample 17ee is shown in Figure 3-53, and the surfaces of the sample on its sides in Figure 3-54. Because of the large slurry viscosity, a comparatively thick cladding is obtained after only 17 dips.

Table 3-20. Constituents of the slurry batch Fish-B-1

Sample Name: 17ee Slurry Batch: Fish-B-1			
	Components	Weight (g)	Weight %
Solvent 1	2-propanol	21.15	78.6
Solvent 2	1-ethoxy-2-peopanol	5.29	19.6
Dispersant	Menhaden fish oil	0.07	0.3
Binder	PVP (10k m.w.)	0.2	0.7
Plasticizer	Polyethylene glycol	0.2	0.7
Powders (Total: 4.58)	MgO (EM Science)	2.74	59.8
	MgO (Aldrich)	0.65	14.2
	Spinel (Baikalox)	1.09	23.8
	Spinel (Alfa Aesar)	0.10	2.2
Solid Loading = 4.58/(21.15+4.58)=17.8%			

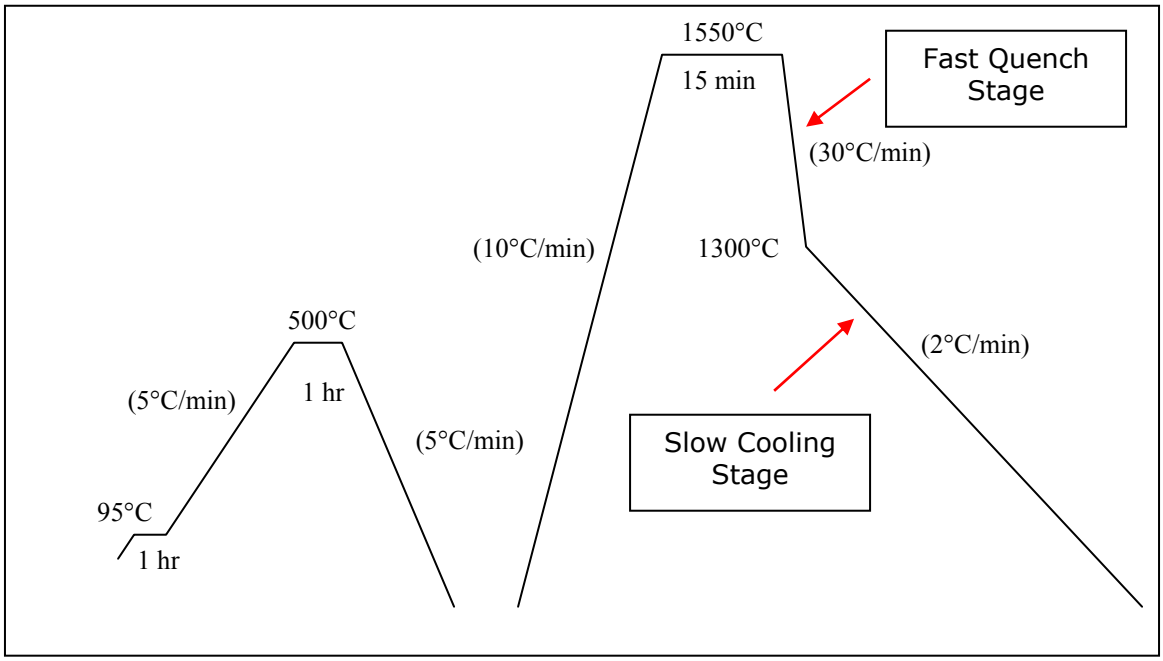

Figure 3-52. The firing profile of sample 17ee

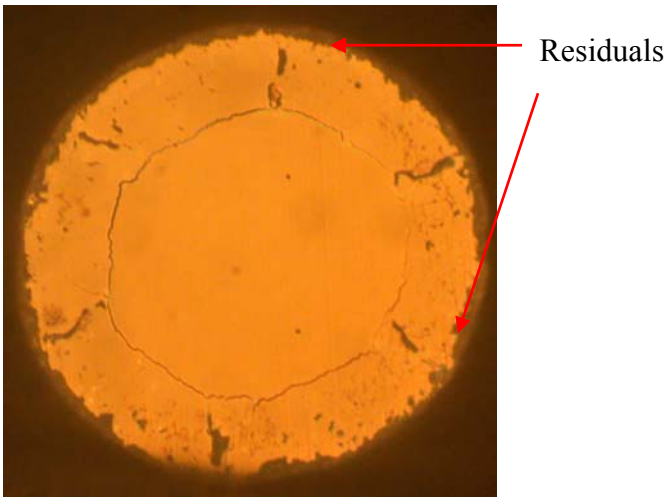

Figure 3-53. The annealed cross section of sample 17ee

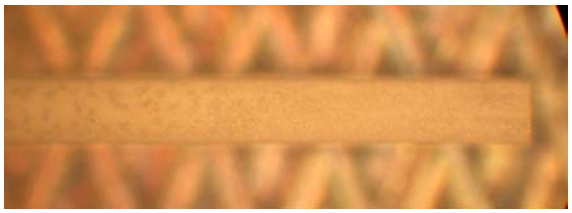

Figure 3-54. The surfaces on the sides of sample 17ee

Even though it is desirable to have smaller number of dips, the high slurry viscosity would likely bring about inferior cladding properties, which are clearly shown in Figure 3-53. There are six hexagonally symmetric cracks in the cladding, and their widths are relatively large. The core/cladding interface is more or less concentric, but it is not very smooth. In general, there are more residuals on the cladding surface, and the cladding surface looks whiter, compared to those samples using polyethylene glycol as dispersant. There are spotty patterns on fiber surfaces, presumably caused by binder deficiency. One thing worthy of noting is that the slurry prepared using fish oil as dispersant does NOT show signs of significant increase in viscosity as a function of time.

Another sample, sample 200kk, with much improved cladding properties is presented here. The slurry composition is listed in Table 3-21. The 10k PVP binder amount is only about half of that for sample 200hh. The firing profiles are illustrated in Figure 3-55. The firing profile of sample 200kk There is major change in the drying and burnout profile, which will be discussed later. The annealed cross section of sample 200kk is shown in Figure 3-56, and the surfaces of the sample on its sides in Figure 3-57.

Table 3-21. Constituents of the slurry batch Fish-B-2

Sample Name: 200kk Slurry Batch: Fish-B-2			
	Components	Weight (g)	Weight %
Solvent 1	2-propanol	23.57	87.4
Solvent 2	1-ethoxy-2-peopanol	2.04	7.6
Dispersant	Menhaden fish oil	0.09	0.3
Binder	PVP (10k m.w.)	1.27	4.7
Plasticizer	Polyethylene glycol	0	0
Powders (Total: 4.60)	MgO (EM Science)	2.73	59.3
	MgO (Aldrich)	0.67	14.6
	Spinel (Baikalox)	1.10	23.9
	Spinel (Alfa Aesar)	0.10	2.2
Solid Loading = 4.60/(23.57+4.60)=16.3%			

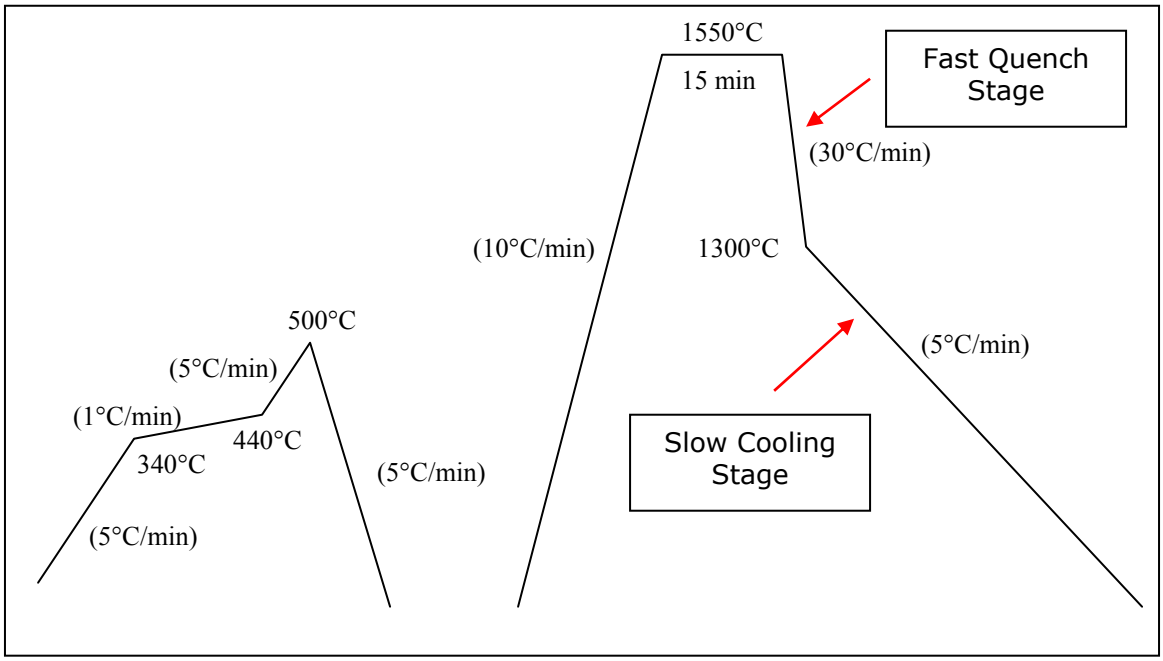

Figure 3-55. The firing profile of sample 200kk

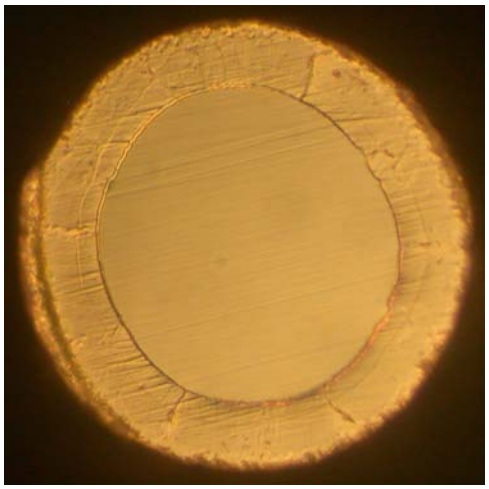

Figure 3-56. The annealed cross section of sample 200kk

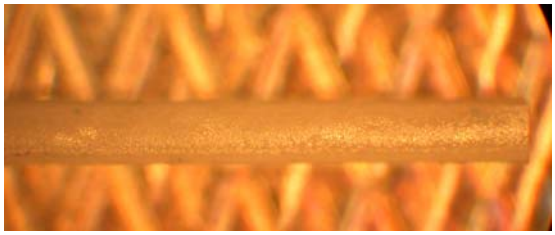

Figure 3-57. The surfaces on the sides of sample 200kk

The results here are very similar to those of sample 200hh, which is prepared using polyethylene as dispersant. The cladding thickness is quite uniform; the core/cladding interface is both smooth and concentric. There are a few very thin cracks in the cladding, and there are also some residuals on the cladding surface. This sample and sample 200hh are the best quality samples manufactured so far.

3.2.2.7 Study of Effectiveness of Dispersant by Particle Size Analysis

3.2.2.7.1 Particle Size Analysis of Spinel Nanopowders from TAL Using the Zetasizer 3000HS from Malvern Instruments

The Zetasizer 3000HS measures particle sizes based on the Brownian motion of the particles in suspension. The system configuration is shown in Figure 3-58. Laser light scattered from the sample cell is detected by a photomultiplier tube oriented at 90° with respect to the laser beam. The angle of the photomultiplier tube can be varied to obtain the spatial distribution of the scattered light. If the particles in suspension were motionless, a classical stationary speckle pattern, where the speckle size and position are

stationary, can be formed as shown in Figure 3-59. The bright patches in the speckle pattern are produced by the constructive interference from ALL the light scattered by ALL the particles. Similarly, the dark patches are generated by the destructive interference from all the light. If the particles undergo Brownian motion, the position and intensity of each speckle will be in constant motion. The rate of speckle fluctuation depends on the particle sizes; the smaller the sizes, the faster are the fluctuation rates. With known viscosity and index of refraction of the solvent, the particle size distribution can be converted from the rates of speckle fluctuation. The sample concentration is also very important in obtaining the correct size data; if the particle concentration is too high, a single laser ray could be scattered multiple times by numerous particles in its path, thus resulting in distortion of the fluctuation rate. Furthermore, the system is design to measure particles with sizes less than about 1μm; for particles above this size limit, the Brownian motion may not be detectable, and the sedimentation of particles may also affect the scattered light intensity. Due to the delicate nature of the size measurement based on Brownian motion, it may require careful experimental design and repeated tests to obtain reliable size data.

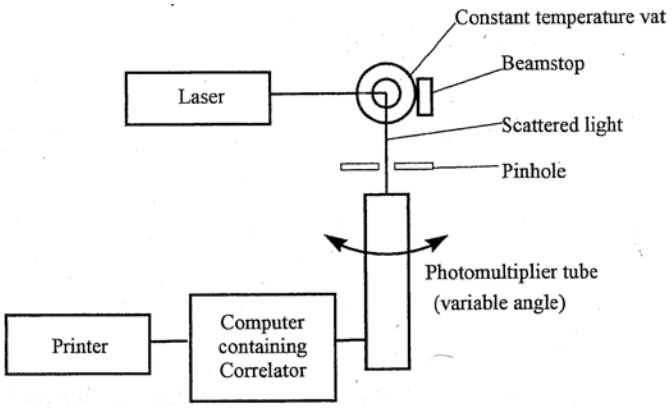

Figure 3-58. The system configuration of Zetasizer 3000HS

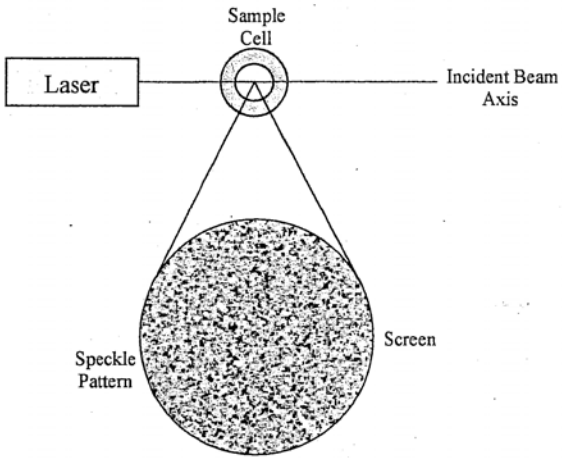

Figure 3-59. Schematic representation of a speckle pattern

3.2.2.7.2 The Size Measurement of spinel nanopowders from TAL (0.050μm) dispersed using Menhaden fish oil, Triton QS-44, and CoatOsil 1211

Since the MgO nanopowder from Aldrich is quite expensive, the lower cost nanopowders from TAL were used to evaluate the performance of Zetasizer 3000HS. The equipment is located in the Environmental department in VT. The nanopowders from TAL were first dried at 500°C for 2.5 hours before mixing. Three batches of samples were prepared: 0.4 w. % fish oil, 0.2 and 0.4 w. % Triton QS-44 in 2-propanol. The solid loading in each batch is 10 w. %. Since the slurry as produced is almost opaque, it needs to be diluted before measurement. 35 μL of the slurry was withdrawn and mixed with 3 c.c. of 2-propanol to reduce its concentration. It is to be noted that this recipe of dilution is arbitrarily chosen, and may not produce the optimal particle concentration. The index of refraction of 2-propanol, 1.377, and its viscosity, 2.3 cp, were input to the equipment as parameters. The duration of each single measurement was set to be 10 seconds. Each batch of sample was measured 30 times in a time period of about 10 minutes. The results are shown in Figure 3-60. Each data point represents the average particle size in each measurement. As can be seen in Figure 3-60, the samples dispersed using Triton QS-44 have larger particle sizes than those of the sample dispersed using fish oil. And the batch with 0.4 w. % Triton QS-44 has smaller sizes compared to those with 0.2 w. % Triton QS-44. It is suspected that, while the exact particle sizes obtained here may not be accurate, the relative trends among the samples may still provide some insight; fish oil seems to be superior to Triton as dispersant. As seen in Figure 3-60, the particle sizes range from 300nm to 600nm among all samples. For the fact that the nominal particle size provided by the manufacturer is only 50nm; these results indicate that the powders are forming large agglomerates in the samples. In the time period of 10 minutes, the particle sizes of all samples increase as a function of time. It is not clear whether the agglomerates are really growing in size so quickly or the results are generated by unknown experimental anomaly.

The 0.4 w. % fish oil sample was sonicated for 25 seconds and then measured again; the results are shown in Figure 3-61. It can be seen that the agglomerate sizes decrease for about 60nm to 90nm after 25 seconds of sonication. This implies that the large agglomerates are broken up by sonication. The sample was further diluted with 2-propanol; the exact amount of dilution was not recorded. As shown in Figure 3-61, as a result of dilution, the agglomerate sizes increase, and there is a rapid increase of particle size as a function of time after dilution, from 400nm to 900nm in 10 minutes.

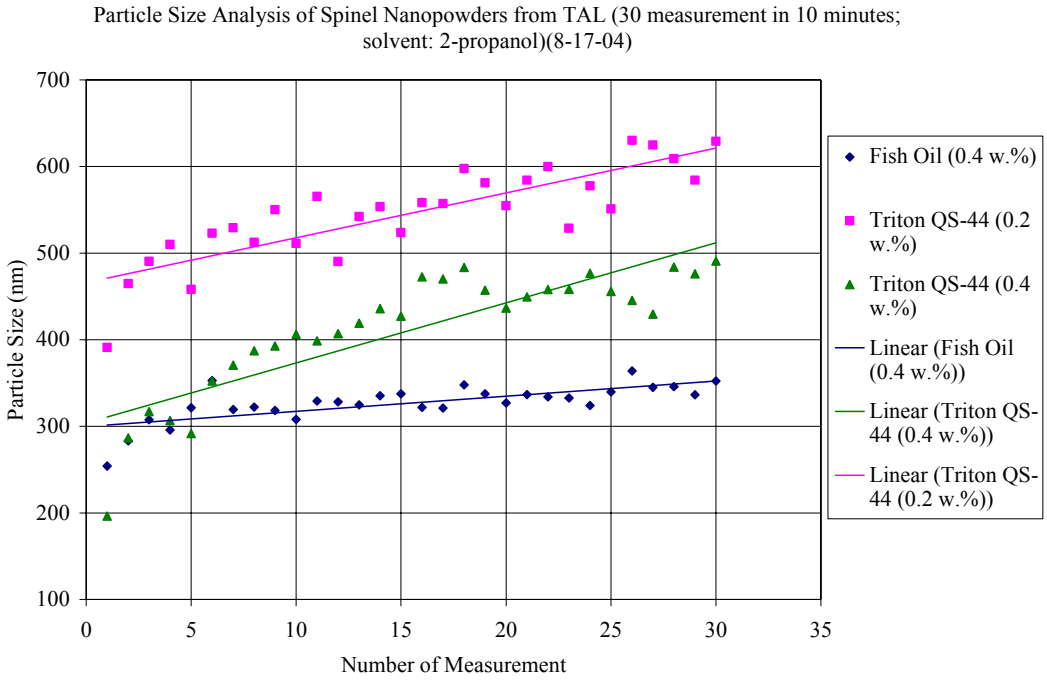

Figure 3-60. Particle size analysis of spinel nanopowders from TAL.

It was later realized that, to prevent multiple scattering of laser light, the sample has to be diluted to a level that the count rate of the photomultiplier tube falls between 10k and 500k. In this level the sample is almost transparent. The particle size is supposed to increase as the sample is diluted, and it would reach a plateau when the count rate falls into the above level. In the current sample, before sonication and dilution (the dark blue diamond in Figure 3-61), the average count rate is 2800K. The subsequent sonication does not affect count rate. The count rate after dilution is 360K, just accidentally fall right into the required level.

The diluted sample was sonicated for another 30 second and re-measured. As seen in Figure 3-61, instead of decreasing, the sizes increase with an even large rate of increasing as a function of time. These results seem confusing at this moment, and in later discussion, this abnormality is contributed to possible variation in the power of sonication.

Three new batches of samples were prepared; 0.4 w. % fish oil, 0.3 and 0.6 w. % CoatOsil 1211 in 2-propanol. The 0.4 w. % fish oil sample has the same composition as the fish oil sample tested on August 17. No Triton samples were examined in this attempt. The solid loading in each batch is also 10 w. %. The samples were ball milled for 27.5 hours after mixing. Similarly, 35 µL of the slurry was withdrawn and mixed with 3 c.c. of 2-propanol to reduce its concentration. The results are shown in Figure 3-62. For the 0.4 w. % fish oil ample, the agglomerate size slowly increases from 200nm to 250nm in 10 minutes; these sizes here are about 100nm smaller than those of the fish oil sample measured on August 17. The photomultiplier tube count rate of the current fish oil sample

is 2250k, and that of the other sample tested on August 17 is 2800k; both of them are too large to obtain accurate size numbers. The 0.3 and 0.6 w. % CoatOsil samples have comparable agglomerate sizes of about 340nm. According to the trends here, it seems that fish oil is also superior to CoatOsil as dispersant in its ability of breaking up large agglomerates.

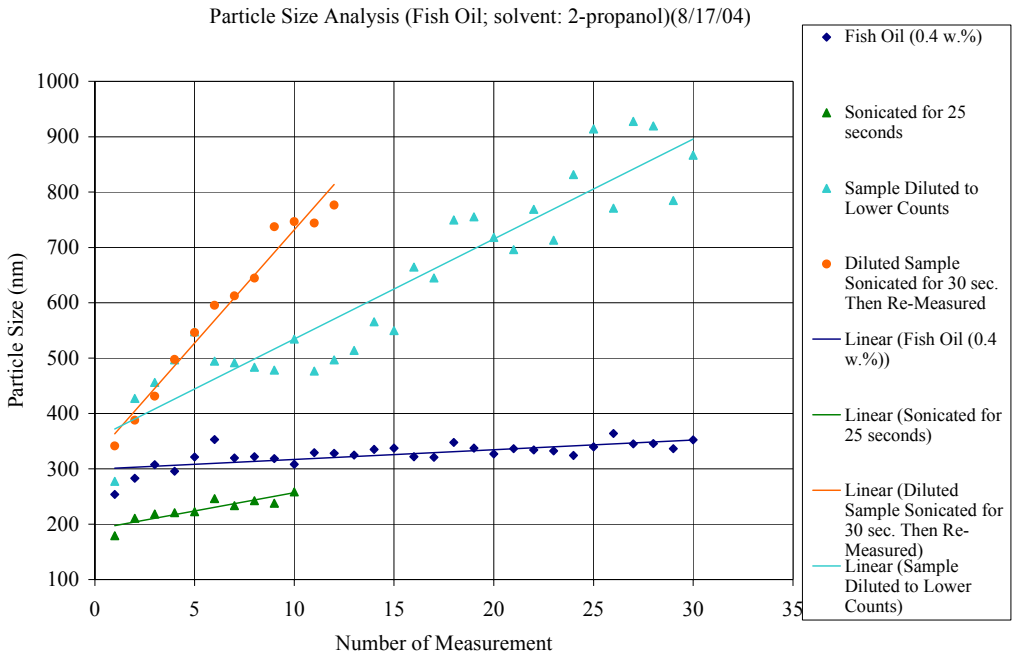

Figure 3-61. Particle size analysis of spinel nanopowders from TAL using fish oil as dispersant

Another batch of sample with 0.3 w. % CoatOsil was prepared by adding 35 µL of the slurry into 3 c.c. of 2-propanol. This new 0.3 w. % CoatOsil sample, together with the 0.6 w. % CoatOsil sample and the 0.4 w. % sample tested earlier were all sonicated for 30 seconds and re-measured. The results are shown in Figure 3-63. The agglomerate sizes of both CoatOsil samples decrease for about 70nm after sonication. On the contrary, the sizes of the fish oil sample increase for about 60nm after sonication. The agglomerate sizes of all samples are very close after sonication, about 260nm.

The behavior of the samples with fish oil after sonication is very inconsistent, sometimes the sizes increase, and at other times they increase. It is suspected that this is due to the power setting of the ultrasonic bath. It was not realized until some time later that the adjustable knob on the equipment is for power adjustment, not for time adjustment. As a result, the power of sonication may be different for different samples. It is assumed that very weak sonication, instead of breaking up large agglomerates as expected, may in fact promote agglomeration in fish oil samples.

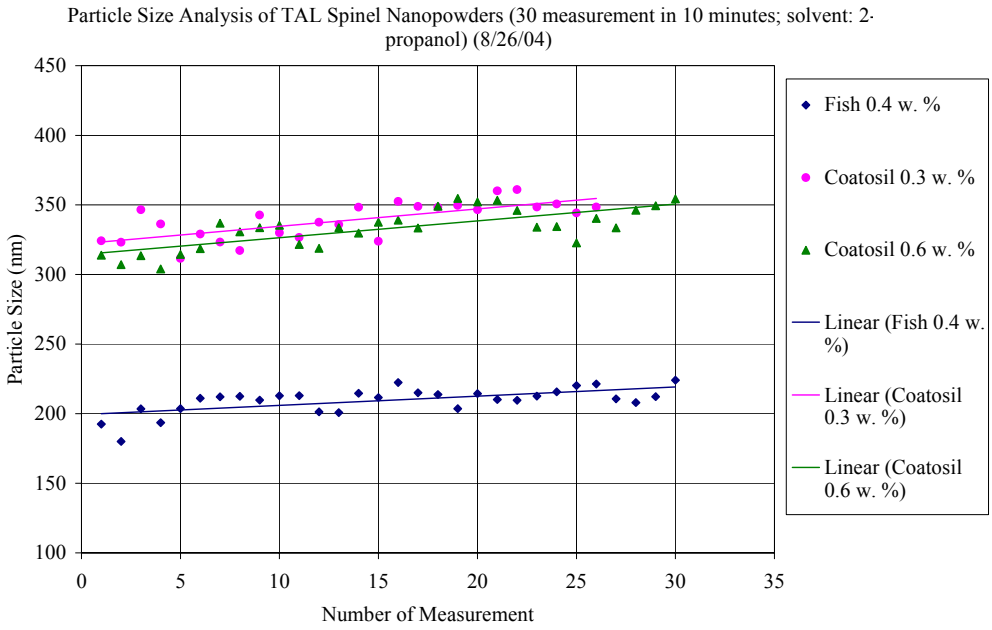

Figure 3-62. Particle size analysis of spinel nanopowders from TAL

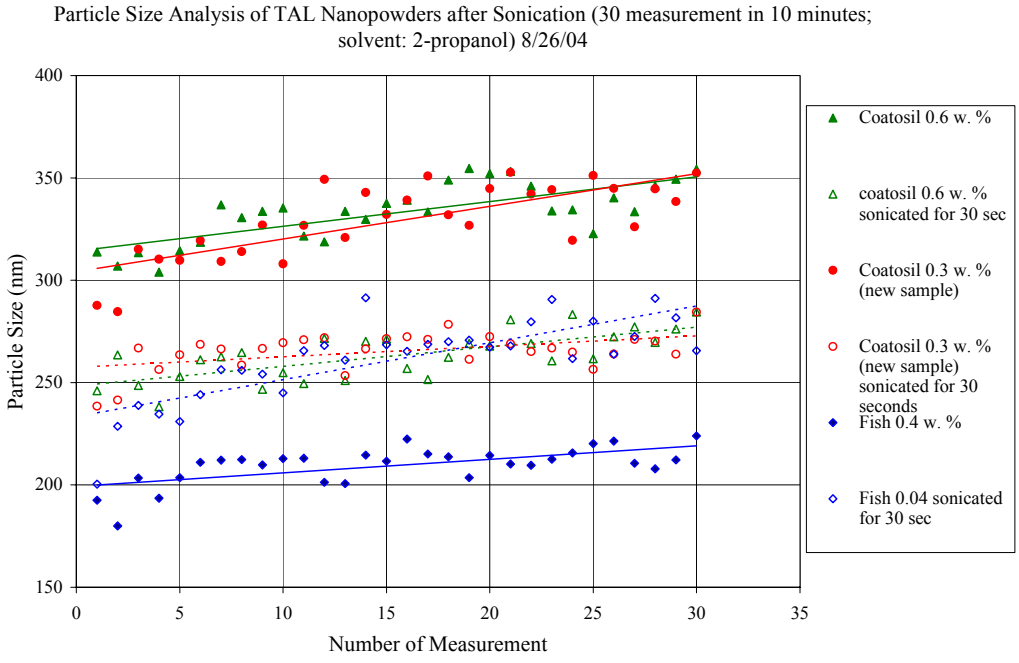

Figure 3-63. Particle size analysis of spinel nanopowders from TAL after sonication

To explore further the stability of slurry as a function of time, the samples prepared on August 17 with 0.4 w. % Triton QS-44 and 0.4 w. % fish oil were re-measured. Similarly, 35 µL of the slurry was diluted with 3 c.c. of 2-propanol to reduce its concentration. The results are shown in Figure 3-64. For the Triton batch, the agglomerate sizes increase for an amount of 300nm after 16 days of storage in a polypropylene bottle. In many of these measurements, the polydispersity index, an indication of the width of particle size distributions, is 1. This suggests that the agglomerates in the sample are highly polydispersed with very wide size distributions. In sharp contrast, the agglomerate sizes of the fish oil sample, after 16 days, not only show no signs of increasing, they actually decrease by about 40nm. At the end of the test, the count rate of the fish oil sample is 2500k, and that of the Triton sample is 2700k. These results hint that the sample with fish oil is more stable than that with Triton as a function of time; the particles in the Triton sample easily form soft agglomerates that can be easily broken up by sonication. On the contrary, the sizes of the already small agglomerates in fish oil sample only reduce a little by sonication.

Both sample were diluted by replacing 2.9c.c of the suspension with 2-propanol. After dilution, the photomultiplier tube count rates dropped to 370k for the Triton sample, and to 136k for the fish oil sample. The final count rates for both samples are well within the required level. The agglomerate sizes for both samples increase for about 50nm after dilution. It is believed that the current data most accurately reflect the true sizes of agglomerates in each sample.

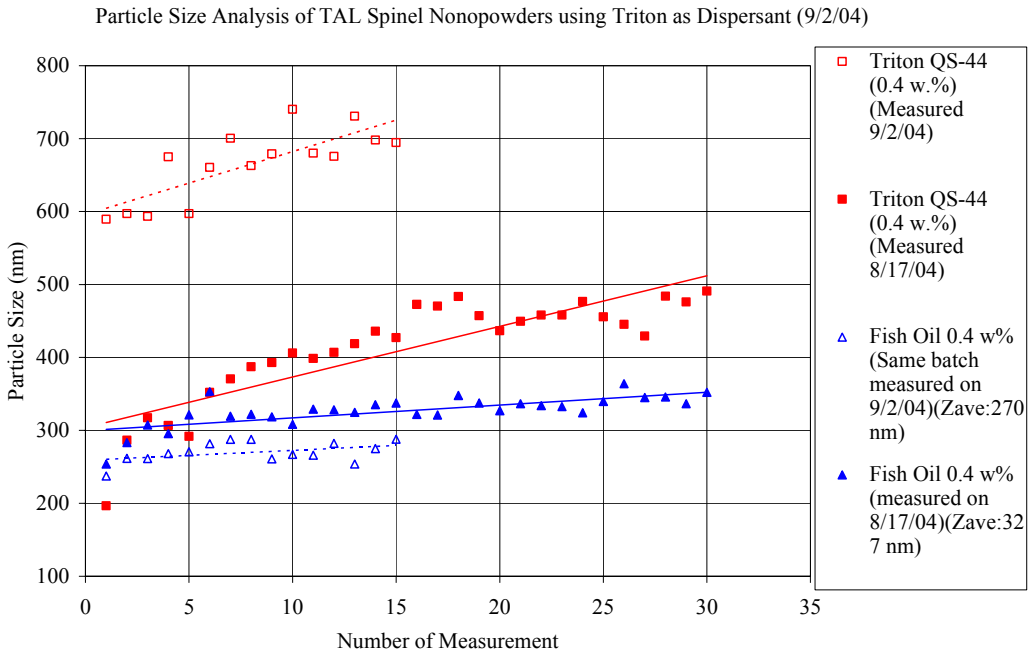

Figure 3-64. Particle size analysis of spinel nanopowders from TAL

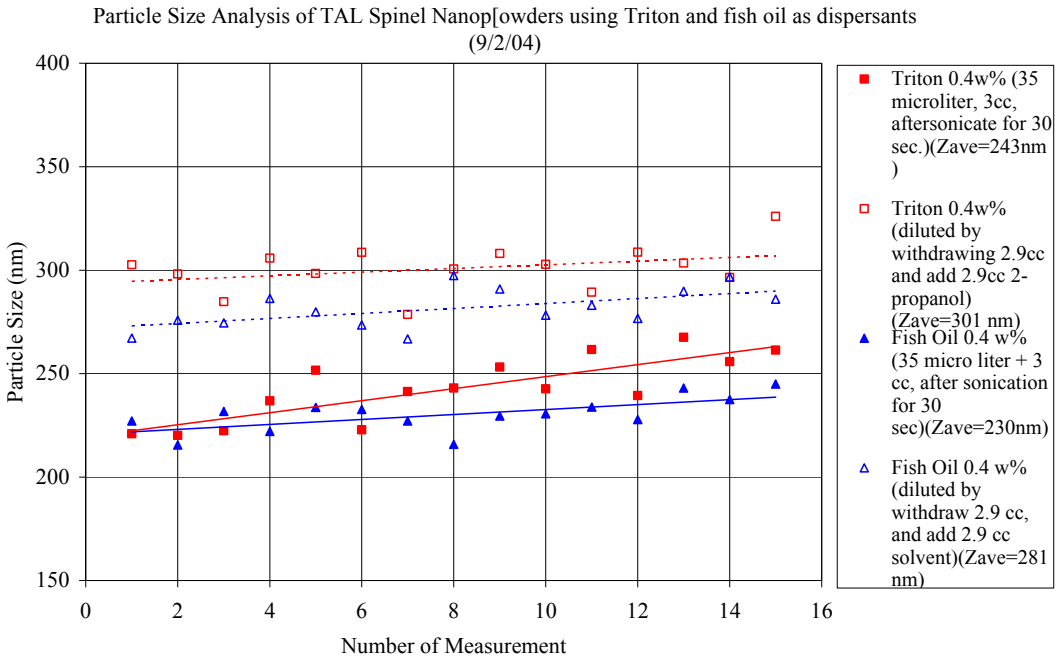

Figure 3-65. Particle size analysis of spinel nanopowders from TAL

To explore the suspension stability of CoatOsil samples, the sample prepared on August 26 with 0.3 w. % CoatOsil was re-measured. Similarly, 35 µL of the slurry was diluted with 3 c.c. of 2-propanol to reduce its concentration. The results are shown in Figure 3-66. Similar to the fish oil cases, the sample prepared using CoatOsil also shows no signs of size increase after 7 days of storage; in fact, the agglomerate sizes measured here are about 18nm smaller than those measured initially. The sample was further diluted by replacing 2.9c.c of the suspension with 2-propanol. After dilution, the photomultiplier tube count rates dropped from 2600k to 512k, and the agglomerate sizes increase from 321nm to 353nm. The suspension was further diluted by replacing 50% of the suspension with 2-propanol, as a result the count rate dropped further to 283k, and the agglomerate size is almost the same after the 50% dilution. This indicate that the particle concentration has reaches the desired level where reproducible size data can be obtained. Furthermore, in about 5 minutes, the agglomerate sizes show no sign of increasing.

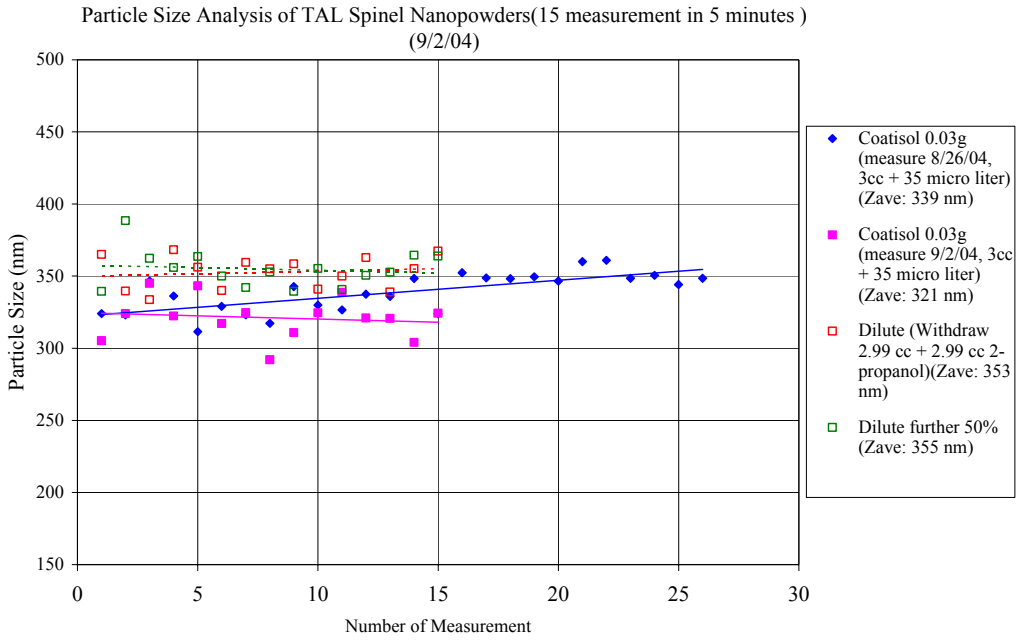

Figure 3-66. Particle size analysis of spinel nanopowders from TAL

3.2.2.7.3 Particle Size Analysis of MgO nanopowders from Aldrich Using Zetasizer with Menhaden Fish Oil and CoatOsil as dispersant

After the confidence on the data obtained using Zetasizer has been established using the spinel nanopowders from TAL, it is a good time now to measure the MgO nanopowders from Aldrich, which is one of the powder components used to prepare the clad sapphire fibers.

Two batches of samples were prepared with 0.4 w. % CoatOsil 1211 and 0.5 w. % Menhaden fish oil as dispersant. The solid loading was 10 w. % for both samples. The samples were ball milled for 21 hours. Before measurement, 35 µL of the slurry was mixed with 3 c.c. of 2-propanol, and the sample was further diluted by replacing 2.9c.c of the suspension with 2-propanol. The sample was measured 30 times in about 10 minutes. The data gathering time for each measurement was set to be 10 seconds. The results are shown in Figure 3-67. The photomultiplier tube count rates for the two measurements are 190k. The average agglomerate size is 412nm, and there is little sign of size increase in 10 minutes.

The 10-second data gathering time for each measurement was an arbitrarily chosen time to obtain preliminary size data, and it is not long enough to obtain size data with high

resolution. Therefore, the sample was measured again using the parameters "Auto Period" and "Auto Mode" in the equipment setting. In this setting it takes about 10 minutes for each single measurement. The results of the measurement using "Auto Period" and "Auto Mode" are shown in Figure 3-68(a). Here the volume percentage of the powders as a function of agglomerate size is plotted. The photomultiplier tube count rate was 189k, and the polydispersity index was 0.299. As can be seen in Figure 3-68(a), there are three distinctive size distributions; the first one centers at 42.8nm with a volume percentage of only 1%, and the second one at 440nm with 83 v. %, and the last one at 707nm with 16 v. %. As mentioned earlier, the powder size provided by the manufacturer is only 13nm. It is believed that the nano powders form agglomerates with a variety of size distributions as illustrated in Figure 3-68(a).The average agglomerate size is 401nm. This size is quite close to the average sizes of 412nm obtained using a 10-second measurement period.

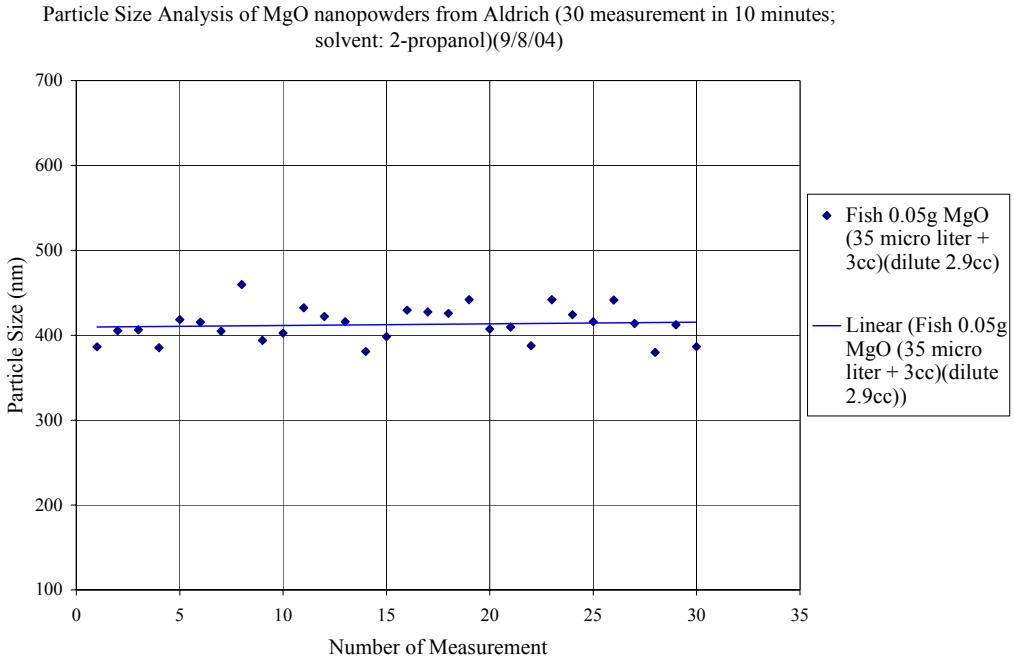

Figure 3-67. Particle size analysis of MgO nanopowders from Aldrich dispersed using fish oil.

The sample was sonicated for 30 seconds and re-measured. The count rate was 212k, and the polydispersity index was 0.031. The results are shown in Figure 3-68(b). In this figure there are only two size distributions, one at 271nm with 81 v. %, and the other at 405nm with 19 v. %. The average agglomerate size is 258nm. After sonication, the size peaks existing before sonication are shifted to smaller peak locations. It is assumed that the larger soft agglomerates are broken apart by sonication and form smaller agglomerates. The same sample was measured again one hour after sonication, and the results are shown in Figure 3-69. The count rate was 208k, and the polydispersity index was 0.245. There is only one broader size distribution with an average agglomerate size of 264nm.

This distribution is quite similar to the one measured immediately after sonication, with a slight size increase of 6nm. It is suspected that in the time period of 1 hour there is no appreciable re-agglomeration of the powders in the suspension.

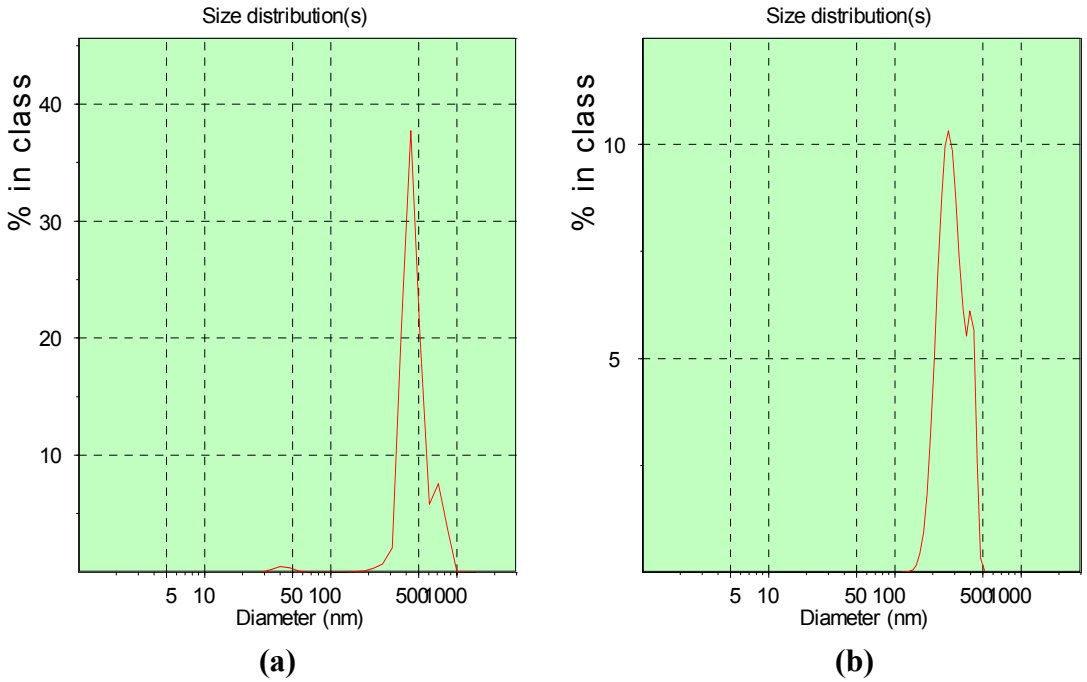

Figure 3-68. Particle size analysis of MgO nanopowders dispersed using fish oil (a) before, and (b) after 30 seconds of sonication

The results of the sample dispersed using 0.4 w. % CoatOsil 1211 are shown in Figure 3-70. Here the sample was measured 45 times in about 20 minutes. Before measurement, 35 µL of the slurry was mixed with 3 c.c. of 2-propanol, and the sample was further diluted by replacing 2.9c.c of the suspension with 2-propanol. The data gathering time for each measurement was 10 seconds, and the count rate is 385k. The average agglomerate sizes are 357nm. The size slightly increases for about 17nm in 20 minutes. The sample was re-measured again using the "Auto Period" and "Auto Mode", and the volume fractions of agglomerates are plotted as a function of size in Figure 3-71. As shown in Figure 3-71(a), before sonication, there is one particle size peak at 393nm, and the average size is 359nm. The polydispersity index was 0.268.

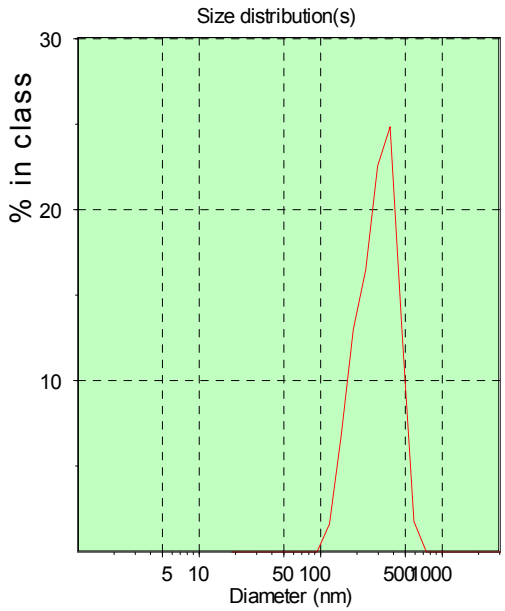

Figure 3-69. Particle size analysis of MgO nanopowders from Aldrich dispersed using fish oil, one hour after sonication.

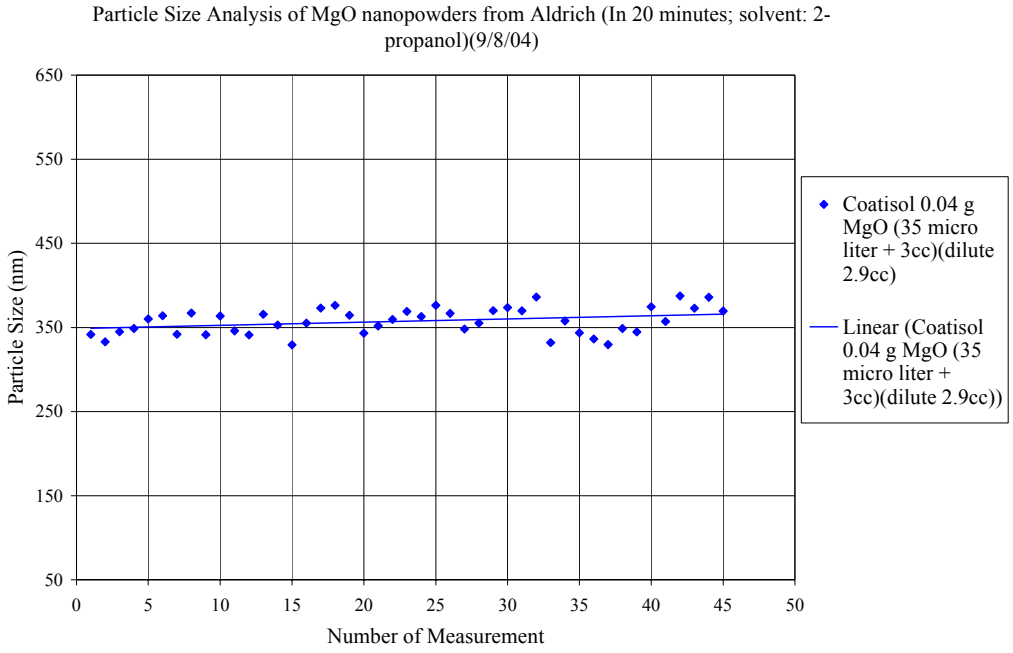

Figure 3-70. Particle size analysis of MgO nanopowders from Aldrich

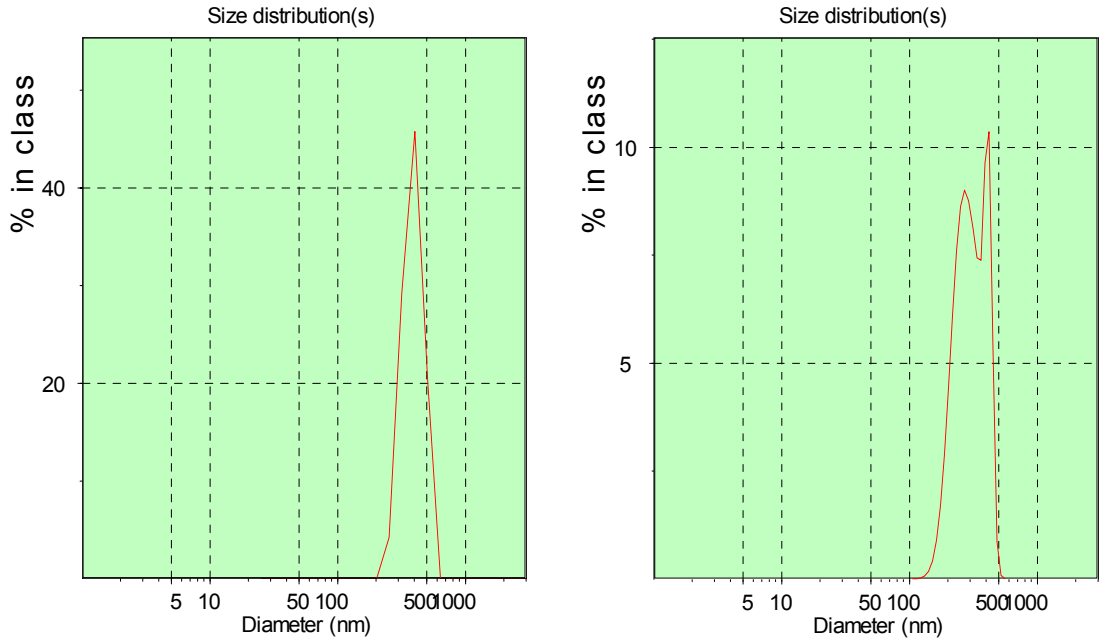

Figure 3-71. Particle size analysis of MgO nanopowders dispersed using CoatOsil 1211 (a) before, and (b) after 30 seconds of sonication

After 30 seconds of sonication, as shown in Figure 3-71(b), another peak at a smaller size, 271nm, develops with 69 v. %. Another peak is located at 404nm, very close to the one before sonication, 393nm. The average size is 259nm. The polydispersity index is 0.038. These results again agree with the assumption that larger agglomerates were broken up by sonication into smaller agglomerates. The sample was re-measured 20 minutes after sonication, the results show that there is one size peak with an average agglomerate size of 262nm, very close to the one immediately after sonication, 259nm.

In this attempt two MgO nanopowder (from Aldrich) samples were prepared with higher concentrations of CoatOsil 1211, 0.8 w. % and 1.2 w. %. The solid loading was 10 % in each sample. The samples were ball milled. Similarly, before measurement, 35 µL of the slurry was diluted with 3 c.c. of 2-propanol, and the concentration was further diluted by replacing 2.9c.c of the suspension with 2-propanol. The results are shown in Figure 3-72. The 0.8 w. % sample was tested twice, and the 1.2 w. % sample was tested one. In each test fifteen measurements were take in five minutes. Also shown in Figure 3-72 are the results of the 0.4 w. % sample measured on September 2. The average agglomerate size for the 0.8 w. % sample is 456nm, and that for 1.2 w. % is 425nm. The average agglomerate size for the 0.4 w. % sample tested on September 2 is 359nm. The results indicate that the increase of CoatOsil concentration from 0.4 w. % to 0.8 and 1.2 w. % does not decrease the agglomerate sizes as anticipated. And the average size of the 1.2 w. % sample is even smaller than that of the 0.8 w. % sample. The 0.8 w. % sample was re-measured using the “Auto Period” and “Auto Mode”. The results are shown in Figure 3-73(a). There is a highly localized peak at 451nm. The count rate was 305k and the polydispersity index was 0.164. The results after 30 seconds of sonication are shown in

Figure 3-73(b). The size drastically decreases to a highly localized peak at 246nm. The count rate was 290k and the polydispersity index was 0.632. It is not clear why such a localized size distribution can have such a large polydispersity index.

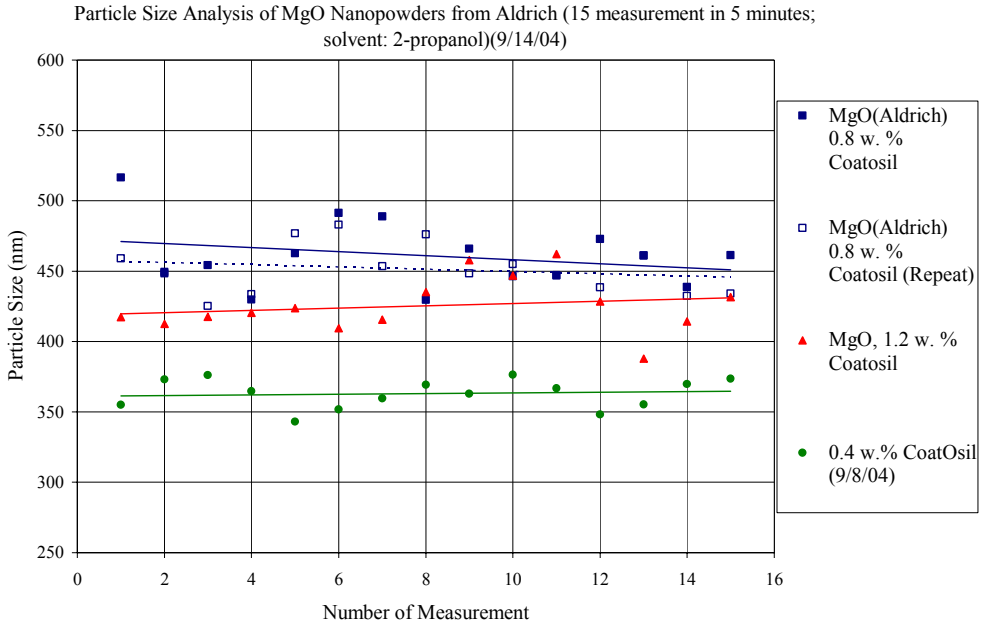

Figure 3-72. Particle size analysis of MgO nanopowders from Aldrich

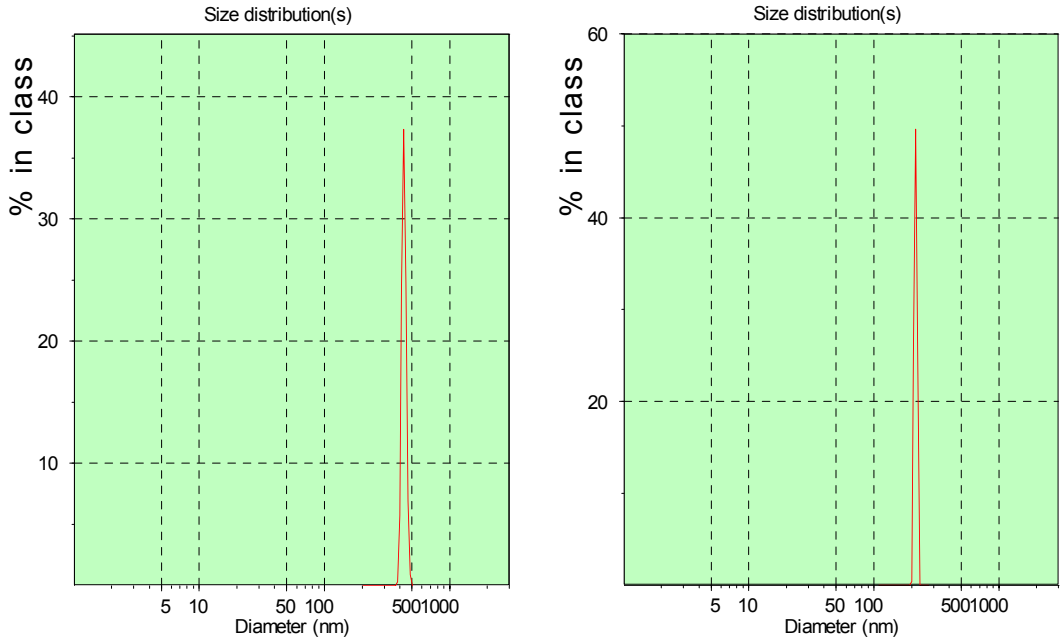

Figure 3-73. Particle size analysis of MgO nanopowders dispersed using CoatOsil 1211 (a) before, and (b) after 30 seconds of sonication

The 1.2 w. % sample was also re-measured using the "Auto Period" and "Auto Mode". The results are shown in Figure 3-74(a). There are two peaks, one located at 427nm with 77 v. % and the other at 705nm with 23 v. %. The average size is 424nm, and the polydispersity is 0.187. The sample was also sonicated for 30 seconds, and the results are shown in Figure 3-74(b). There are also two peaks in the size distribution. However, the peaks are located in much smaller sizes, one at 274nm with 67 v. %, and the other at 58.3nm with 33 v. %.

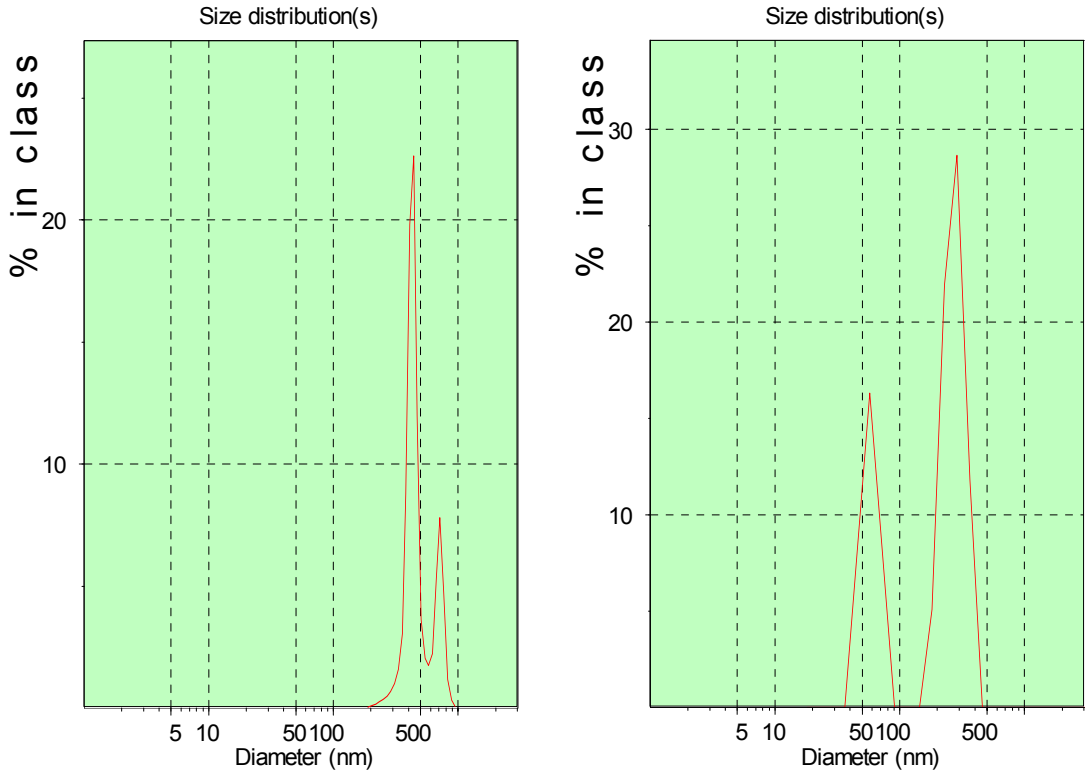

Figure 3-74. Particle size analysis of MgO nanopowders dispersed using CoatOsil 1211 (a) before, and (b) after 30 seconds of sonication

3.2.2.7.4 Use a graticule with 10μ grid to estimate the particle sizes of the MgO powders from EM Science and the spinel powders from Baikalox under an optical microscope

As mentioned earlier, the Zetasizer can only measure particles with sizes of less than 1μm. Therefore, other means are needed to determine the particle sizes of the other two types of powders, MgO from EM Science and spinel from Baikalox. In this section the results of the particle size measurement using a graticule with scale 1mm long in 0.01mm (10μm) divisions are discussed. The graticule (01B21217, NE28-21mm, 1mm/100Pts) was purchased from Pyser-Sgi Ltd. in UK.

Two batches of MgO samples were prepared with 0.4 and 0.8 w. % CoatOsil 1211 dispersant. The solid loading was 10 w. % for each sample. The periods of ball milling of the samples were not recorded. Four drops of the slurry were diluted with 3.6g of 2-propanol before measurement. The pipettes used for slurry transportation are the fine-tip disposable transfer pipettes from VWR International (Cat. #: 14670-330). Four drops of the slurry have a volume of about 85µL. One drop of slurry was dispensed on the graticule for observation under an optical microscope. Two graticule samples were prepared and observed for each batch of slurry. Several pictures were taken from one graticule sample. The representative results are shown in Figure 3-75(a) to (d). Figure 3-75(a) and (b) show the representative pictures for 0.8 w. % CoatOsil slurry, sample 1 and sample 2, respectively. Figure 3-75(c) and (d) show the representative pictures for 0.4 w. % CoatOsil slurry, sample 1 and sample 2, respectively. As shown in the pictures, it is clear that the two samples with 0.4 w. % CoatOsil form larger agglomerates on the graticule than those with 0.8 w. % CoatOsil. Image processing was performed on Figure 3-75(a) to enhance the visibility of powder particles. The results are shown in Figure 3-76. As mentioned earlier, the total length of the scale is 1mm with 100 divisions, so each division is 0.01mm (10µm) long. The yellow bars are 2.7µm wide. All the particles seem to be less than the width of the bar, so all the particles are less than 2.7µm. The smallest particles are about 1µm. A rough estimation puts the average particle size at about 1.7µm.

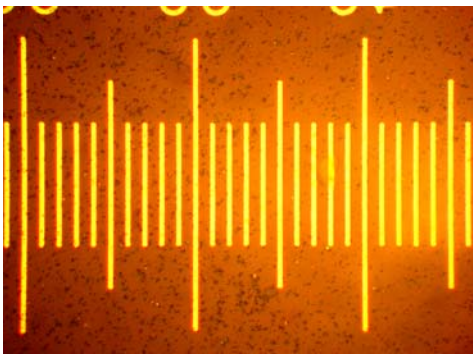

(a) 0.8 w. % CoatOsil, sample 1

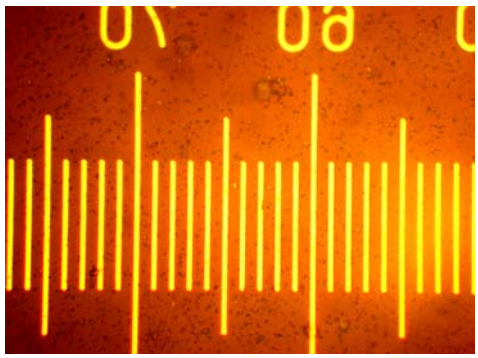

(b) 0.8 w. % CoatOsil, sample 2

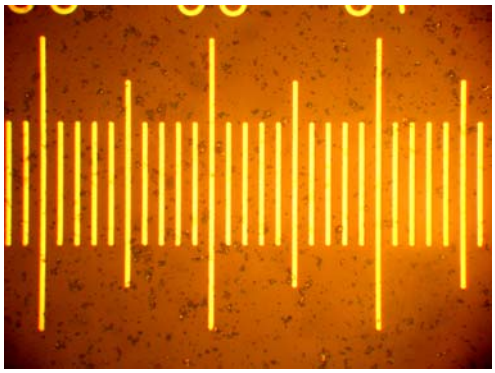

(c) 0.4 w. % CoatOsil, sample 1

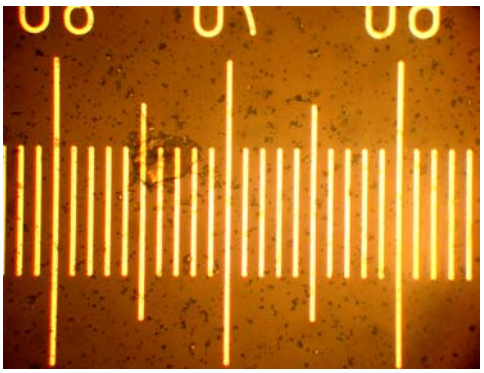

(d) 0.4 w. % CoatOsil, sample 2

Figure 3-75. The particle analysis of MgO powders from EM Science using a graticule under an optical microscope.

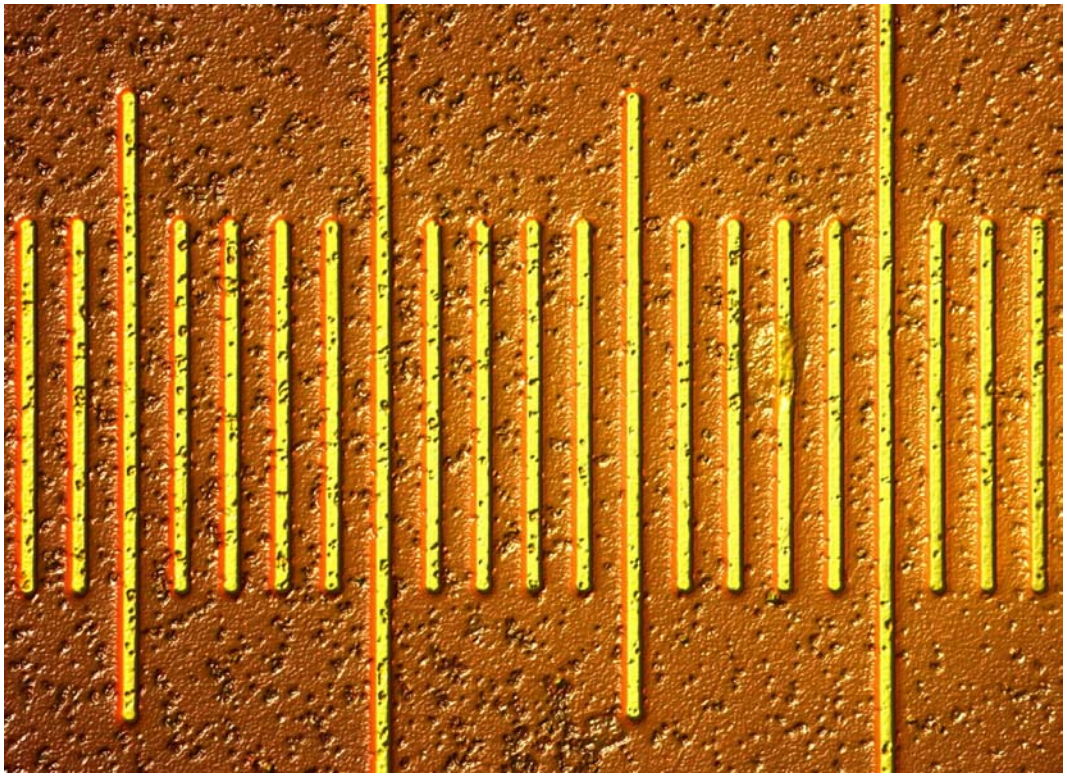

Figure 3-76. MgO powders from EM Science with 0.8 w. % CoatOsil

Two batches of spinel samples were prepared with 0.5 and 1.0 w. % CoatOsil 1211 dispersant. The solid loading was 10 w. % for each sample. The results are shown in Figure 3-77(a) to (d). Figure 3-77(a) and (b) show the representative pictures for 1.0 w. % CoatOsil slurry, sample 1 and sample 2, respectively. Figure 3-77(c) and (d) show the representative pictures for 0.5 w. % CoatOsil slurry, sample 1 and sample 2, respectively. It is obvious from the pictures that the samples with 1.0 w. % CoatOsil have very large agglomerates. And the samples with 0.5 w. % CoatOsil possess relatively small agglomerates in Figure 3-77(d) and finely dispersed particles in Figure 3-77(c). It appears that, with an excessive amount of dispersant and relatively finer and lighter particles, the dispersant tends to coagulate together and drag the fine particles with it, thus resulting in powder agglomerates.

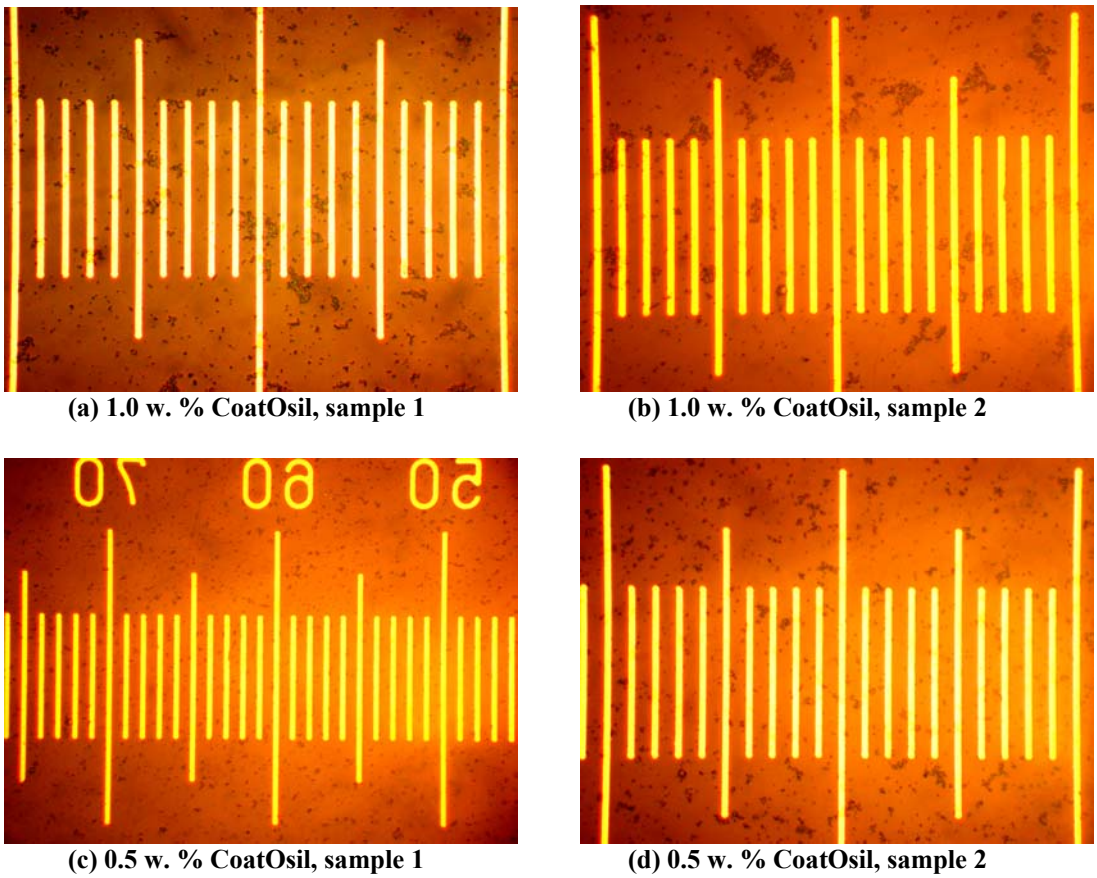

(a) 1.0 w. % CoatOsil, sample 1 **(b) 1.0 w. % CoatOsil, sample 2**

(c) 0.5 w. % CoatOsil, sample 1 **(d) 0.5 w. % CoatOsil, sample 2**

Figure 3-77. The particle analysis of spinel powders from Baikalox using a graticule under an optical microscope

Figure 3-77 (c) is image processed to enhance the particle visibility. The results are shown Figure 3-78. By comparing the particle size with the width of the bar, which is 2.7µm, all particles are about less than half of the size of the bar, which is 1.3µm. Many of the particles are in the range or less than ¼ of the width of the bar, which is 0.7µm. A rough estimation puts the average particle at 0.5nm.

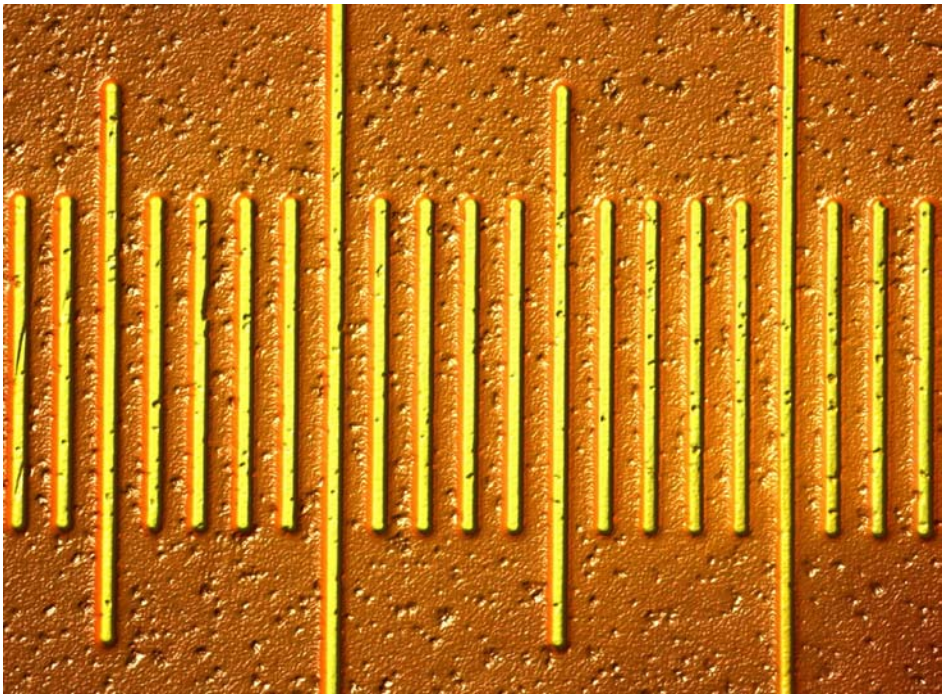

Figure 3-78. Spinel powders from Baikalox with 0.5 w. % CoatOsil

3.2.2.7.5 Sedimentation Tests to Estimate the Optimal amount of CoatOsil 1211 as Dispersant on the MgO Powders from EM Science and the Spinel Powders from Baikalox

If the powders in solvent are not fully dispersed, large agglomerates could form. In a sedimentation test, these large agglomerates settle relatively faster and with larger sediment volume, i.e., smaller packed-bed density. So the criterion for good powder dispersion in a sedimentation test is small sediment volume and long settling time. The MgO powders from EM Science and the spinel powders from Baikalox were tested to estimate the optimal amount of CoatOsil 1211 as dispersant.

Three series of settling tests were initiated. The solid loading for all samples are 10 w. %. The first series consisted of two batches of MgO samples with 0.4 and 0.8 w. % CoatOsil and two batches of spinel samples with 0.5 and 1.0 w. % CoatOsil. The ball milling time for the samples were not recorded. The second series consisted of two batches of MgO samples with 1.2 and 1.6 w. % CoatOsil and two batches of spinel samples with 1.5 and 2.0 w. % CoatOsil. All samples were balled milled. The last series consist of three batches of MgO samples with 0, 0.2, and 0.4 w. % CoatOsil and one batch of spinel sample with 2.5 w. % CoatOsil. All samples were ball milled. During the testing, 10c.c. of each sample was poured into a 10ml cylinder, whose opening was sealed with Parafilm and a rubber band to prevent the solvent from evaporation.

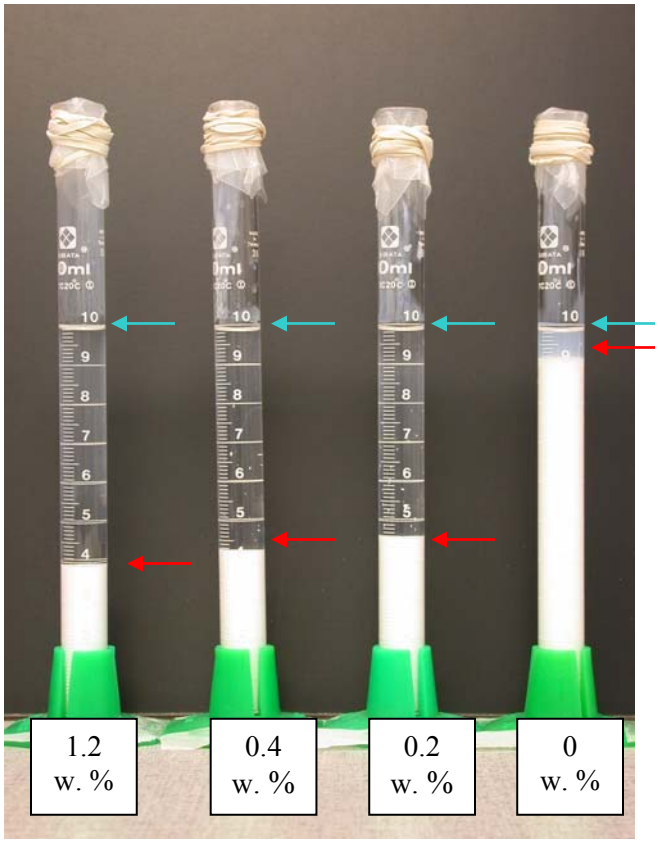

Figure 3-79. The settling test of MgO powders from EM Science using CoatOsil 1211 as dispersant. In each sample 1.0g of the powders are mixed with 10.0g of isopropyl alcohol. From right to left: no dispersant, 0.2 w. % dispersant, 0.4 w. % dispersant, and 1.2 w. % dispersant. All samples have been tested for at least 22 days, except for the 1.2 w. % sample, which has been tested for 24 days.

3.2.2.7.5.1 MgO Samples

The experimental setup for four of the MgO batches with 0, 0.2, 0.4, and 1.2 w. % CoatOsil are shown in Figure 3-79. Each cylinder was filled with 10c.c of the solution at the beginning of the test as marked by the blue arrows in the figure. The red arrows indicate the sediment bed-packing volumes of the samples. All samples in the figure have been tested for 22 days, except for the 1.2 w. % sample, which has been tested for 24 days. The sediment volumes as a function of time for all seven MgO samples are shown in Figure 3-80. There is inconsistency in the results with the two 0.4 w. % samples. The first sample prepared settled more rapidly than the second. The cause for this inconsistency is not clear at this moment. The sample with no CoatOsil settles very slowly compared to the sample with even a very small amount of CoatOsil, 0.2 w. %. After 520 hours of testing, the sediment volumes of the samples with 0, 0.2, and 0.4 (September 24 sample) w. % are still slowly decreasing; it is not sure whether, with long enough test time, the final sediment volumes of these samples would reach the levels of other samples with higher CoatOsil contents. The samples with relatively high CoatOsil amounts, i.e., 0.8, 1.2, and 1.6 w. %, all settle rapidly to similar sediment volumes.

From Figure 3-79, in the cylinder containing 0 w. % CoatOsil sample, the solution above the sediment/solvent interface at 9c.c. is milky, indicating that there are some fine particles suspended in the solution. As mentioned earlier, the criterion for good dispersion is small sediment volume and longer settling time. Since the testing time here is not long enough for the 0, 0.2, and 0.4 w. % samples to fully settle, it is not certain which sample has the smallest sediment volume. On the other hand, judging from the settling rate of each sample, the addition of CoatOsil greatly increase the settling rates, implying that large agglomerates are formed as a result of the addition of CoatOsil. Therefore, CoatOsil 1211, instead of serving as dispersant as expected, most likely acts as flocculant in the solution. It is suspected that CoatOsil causes the aggregation of fine suspended particles, and the floc settles to the bottom of the cylinder in a much faster rate than the sample without any CoatOsil.

Based on the Stoke's Law, the agglomerate sizes can be calculated using the settling rates. For spherical particles in a viscous fluid in the Reynold's region, the constant particle settling rate resulting from the force balance between the gravitational force and the fluid dragging force can be expressed as

$$v_s = \frac{g\, d_p{}^2 \left(\rho_p - \rho_f\right)}{18\,\mu} \qquad (1)$$

where v_s is the constant particle settling rate in cm/sec, g the gravitational constant in cm/sec^2 (980 cm/sec^2), d_p the particle diameter in cm, ρ_p and ρ_f the densities of the particle and the fluid in g/cm^3 respectively (3.6 g/cm^3 fro both MgO and spinel, 0.785 g/cm^3 for 2-propanol), and finally μ the fluid viscosity in poise (2.3x10^{-2} poise for 2-propanol). As seen from Figure 3-80, the samples with higher CoatOsil concentrations, 0.8, 1.2, and 1.6 w. %, have almost the same settling rate at the first 18 hours of the test; they settle for 4.43 cm in 18 hours as represented by the first set of data points. With proper values of all the parameters substituted, Equation (1) can be expressed as

$$\left(\frac{4.43}{18\times 60\times 60}\right)\left(\frac{cm}{\sec}\right) = \frac{980\left(\frac{cm}{\sec^2}\right) d_p{}^2 \left(cm^2\right)(3.6-0.785)\left(\frac{g}{cm^3}\right)}{18\times 2.3\times 10^{-2}\left(\frac{g}{cm\times \sec}\right)}. \qquad (2)$$

The agglomerate diameter calculated from the above equation is 0.24μm. This agglomerate size is much smaller than expected, since the particle size estimated from the optical microscopy shown in Figure 3-76 is 1.7μm. As can be seen from Figure 3-80, the sample with no CoatOsil added settles very slowly, for about 0.93cm in about 526 hours. From Equation (1) the calculated particle size is only 0.02μm (20nm!). One possible cause of the size inconsistency is the non-spherical particle shapes. However, from Figure 3-76 the shape of particles seems to be not very deviated from spheres. So at this moment no explanation can be provided for this inconsistency.

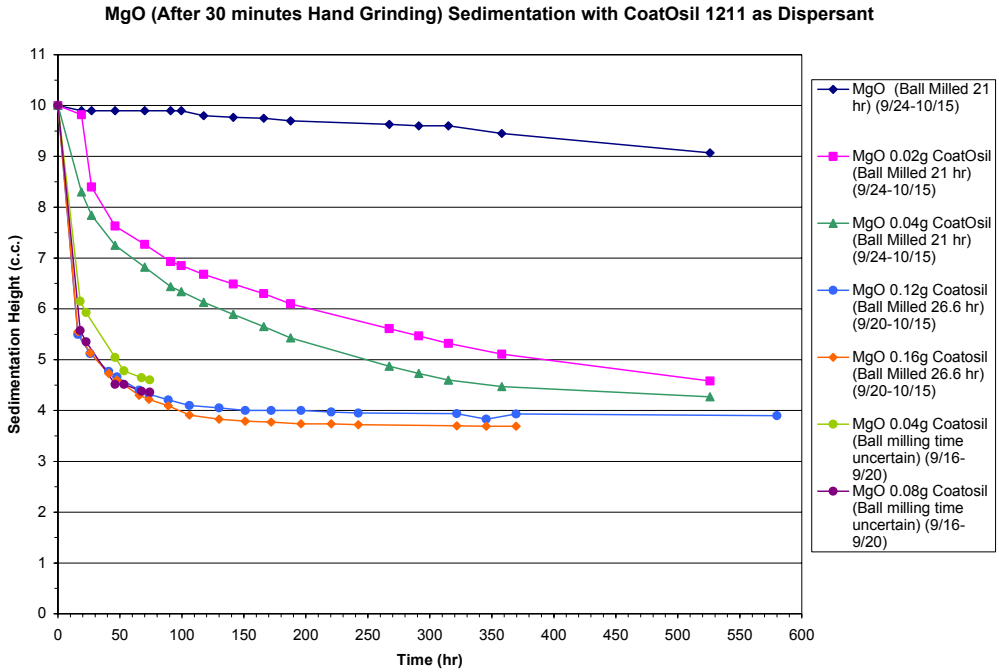

Figure 3-80. All seven MgO samples dispersed with CoatOsil 1211

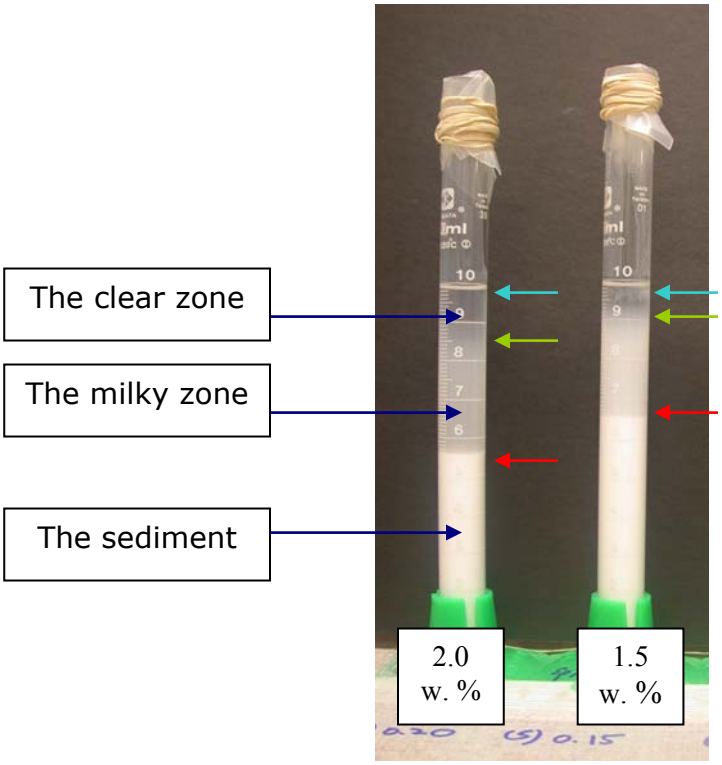

Figure 3-81. The settling test of spinel powders from Baikalox using CoatOsil 1211 as dispersant. In each sample 1.0g of the powders are mixed with 10.0g of isopropyl alcohol. From right to left: 1.5 w. % dispersant, and 2.0 w. % dispersant. The samples have been tested for16 hours.

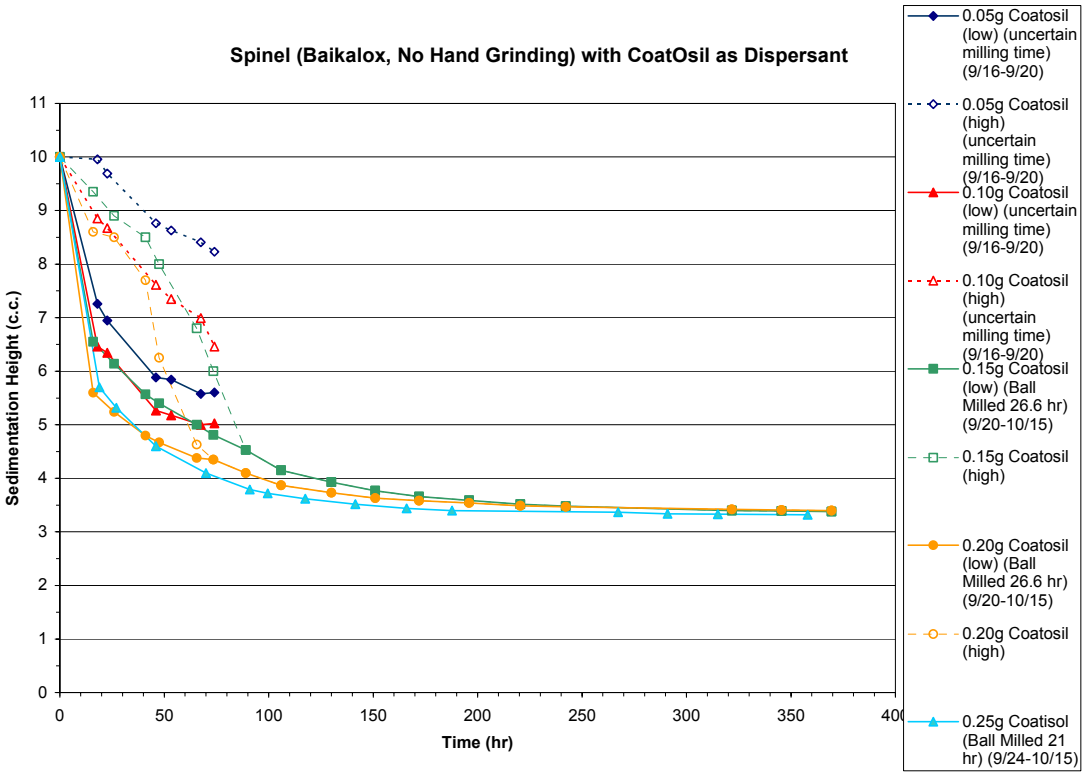

Figure 3-82. All five spinel samples dispersed with CoatOsil 1211. The full markers represent the sediment/solution interfaces and the hollow markers of the same colors the milky-solution/clear-solution interfaces in the samples. The CoatOsil amounts are 0.5, 1.0, 1.5, 2.0, and 2.5 w. %.

3.2.2.7.5.2 Spinel Samples

The experimental setup for two of the spinel batches with 0.15 and 0.20 w. % CoatOsil are shown in Figure 3-81. The samples have been tested for16 hours. As shown in the figure, in contrast to most of the MgO samples, there exists another less well defined interface between the zone of milky solution and the zone of clear solution as marked by the green arrows. Also, the degree of cloudiness in the milky zone is greater than here compared to the 0 w. % CoatOsil MgO sample in Figure 3-79. These results imply that there is a larger amount of spinel fine particles suspended in the milky zone here. Also can be seen in the figure is that the milky zone in the 1.5 w. % sample is more cloudy than that of the 2.0 w. % sample. This suggests that there are more fine particles suspended in the milky zone in the 1.5 w. % sample. The addition of more CoatOsil reduces the number of fine particles by agglomerating them together.

Both the levels of the sediment/solution interface and the milky-zone/clear-zone interface were recorded as a function of time. And the results are shown in Figure 3-82 for all five spinel samples. The CoatOsil amounts are 0.5, 1.0, 1.5, 2.0, and 2.5 w. %. The filled markers represent the sediment/solution interfaces and the hallow markers of the same

colors the milky-zone/clear-zone interfaces in the samples. The two interfaces in each sample merge at a certain time during the test. The rough general trends shown in Figure 3-82 are that the larger the amount of CoatOsil, the faster the settling rates of both the sediment zone (the filled markers) and the milky zone (the hollow markers). It is believed that CoatOsil also serves as flocculant in spinel solution. More CoatOsil renders larger flocs to be formed, and they settle with larger settling rates. In all samples the sediment settling rates are faster at the beginning of the test, and they get slower and slower as a function of time. On the contrary, the milky solution settling rates are slower at the beginning of the test and get faster later, resulting in curves concaving downwards. No explanation is available at this moment regarding these phenomena. For the three samples with the higher amounts of CoatOsil, 1.5, 2.0, and 2.5 w. %, the final sediment heights are almost the same after 370 hours of test.

The agglomerate sizes of two samples, 0.5 and 2.0 w. %, were calculated using the Stoke's Law. As shown in Figure 3-82, for the sample with 0.5 w. % CoatOsil, the sediment settles for 2.74cm in 18 hours, and the milky zone settles for only 1.24cm in 46 hours. The particle sizes calculated using the Stoke's Law are 0.19μm for the sediment and 0.08μm for the milky solution. For the 2.0 w. % CoatOsil sample, the sediment settles for 2.74cm in 18 hours, and the milky zone settles for 1.24cm in 46 hours. The calculated diameters using Stoke's Law are 0.25μm for the sediment and 0.11μm for the milky zone. These sizes are also smaller than the size estimated from optical microscopy, 0.5μm from Figure 3-78. Since CoatOsil was added to all samples as flocculant, the actual particle sizes of the spinel powders should be even smaller than the calculated values. It is believed that the Stoke's Law can not be applied to particle agglomerates due to the structure of the agglomerates.

3.2.2.8 Measurement of Numerical Aperture and Estimate of Mode Volume in Clad Sapphire Fiber

In order to assess the effectiveness of the spinel cladding in reducing the number of guided modes in the sapphire fiber, an apparatus was assembled to measure the numerical aperture (NA) of a sapphire fiber before and after cladding. It is expected that the use of claddings (coatings) on sapphire fibers will reduce the number of electromagnetic modes that propagate in the fiber. Minimization of the number of propagating modes will permit the use of optical interferometry and fiber Bragg gratings with sapphire fibers, which in turn will facilitate the development of pressure sensors using sapphire fibers.

Optical fibers can be characterized by a parameter called the numerical aperture, which is a measure of the range of solid angles over which light incident on the input end of the fiber can be captured and transmitted by the fiber. As the modal volume (the number of propagating modes that the fiber can support) is decreased, the numerical aperture of the fiber decreases. Therefore, a change of numerical aperture can be correlated to a change in modal volume of a fiber.

For an ideal (no scattering at the core-cladding interface) step-index multimode fiber, the numerical aperture of the fiber depends only upon the refractive indices of the core and cladding:

$$NA = \sqrt{n_{co}^{2} - n_{cl}^{2}}\,,$$

Equation 4

where n_{co} is the refractive index of the fiber core, and n_{cl} is the refractive index of the cladding. Based on the c-axis refractive index of sapphire fiber (1.768) and the refractive index of magnesium aluminate spinel, a numerical aperture of 0.40 would be predicted for the spinel-clad sapphire fiber.

In the apparatus used to measure numerical aperture, the collimated light output by a helium neon laser is reflected by a mirror towards the end of a sapphire fiber at an angle θ with respect to the longitudinal axis of the fiber, as illustrated in Figure 3-83. Any light captured by the fiber is guided to the other end of the fiber, where an optical power meter measures the power output by the fiber. The mirror is adjustable so that the angle θ of light incident upon the fiber is variable. In this way, the light power captured by the fiber as a function of input angle of incidence may be measured, and from this, the numerical aperture may be calculated. Figure 3-84 is a photograph of the experimental set-up.

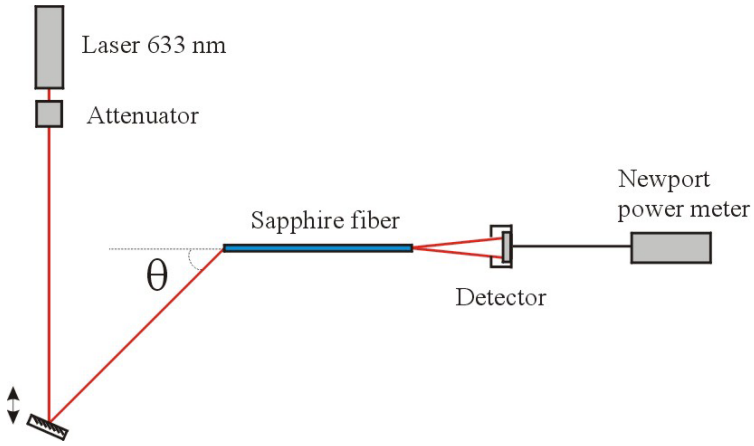

Figure 3-83. Schematic of Experimental Set-Up for Measurement of NA

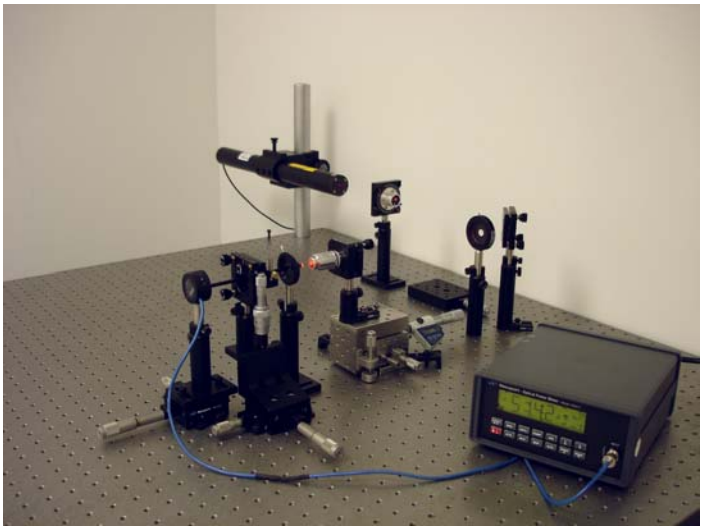

Figure 3-84. Photograph of Set-up for Measurement of NA

Two identical six-inch long samples of 125 μm diameter sapphire fiber (obtained from Photran, Inc.) were used to evaluate the effect of the spinel cladding on the optical performance of the sapphire fiber. First, one of the sapphire fibers was polished before coating, and the numerical aperture of the fiber was measured using the set-up illustrated above. Using the Telecommunication Industry Association's Fiber Optic Test Procedure (FOTP) criteria for measurement of numerical aperture, the maximum angle acceptance for the fiber is chosen to be that angle at which the output power falls to 10% of the maximum power.[12]

Figure 3-85 shows the variation in optical power accepted by the unclad sapphire fiber as a function of input angle. From the plot, the angle θ_c which the power falls to 10% is estimated to be 36°. By the definition of numerical aperture,

$$NA = \sin \theta_c \qquad \textbf{Equation 5}$$

the NA of the unclad sapphire fiber was found to be approximately 0.59.

[12] "Optical Fibers -- Part 1-43: Measurement Methods and Test Procedures -- Numerical Aperture," (FOTP)-177, TIA-455-177-B, Telecommunication Industry Association (TIA), Arlington, VA.

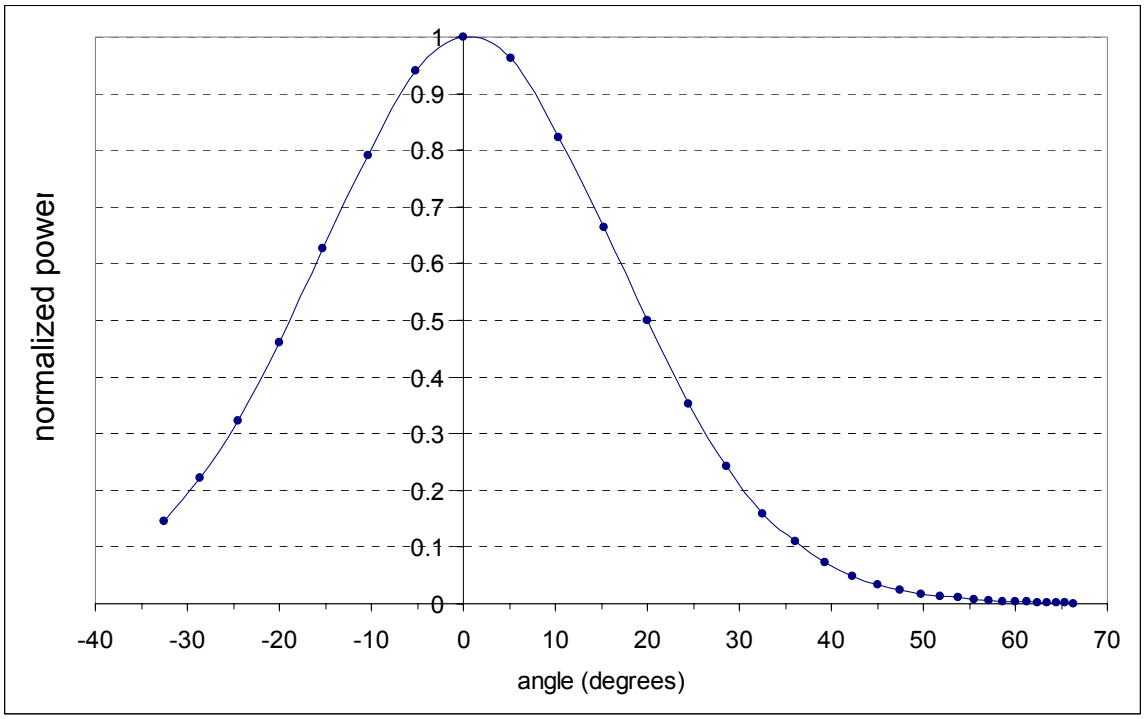

Figure 3-85. Plot of the normalized output power for unclad sapphire fiber as a function of angle of incidence of input light.

The second 6 inch sapphire fiber was then coated by dipping the sapphire fiber into the slurry consisting of 0.68 g of MgO powders from Aldrich, 1.21 g spinel powders from Baikalox, and 2.73 g MgO powders from EM Science. All powders were dried at 500°C for 1 hour before slurry preparation. The slurry was prepared by mixing 20.9 g of 2-propanol with 150 µL of menhaden fish oil (Aldrich) in a 4-oz polyethylene bottle filled with 133 g ¼-inch grinding media. The oxide powders were added to the slurry immediately after being taken out from the oven. The slurry was then ball milled for 17.5 hours at 104 rpm. After ball milling, 2.2 g polyvinylpyrrolidone (PVP) and 2.1 g 1-methoxy-2-propanol were added to the slurry followed by 6 hours of ball milling.

Before dipping, the sapphire fiber was cleaned and soaked in 2-propanol for 15 minutes. Finally, the fiber was dipped in the slurry 100 times before firing, using a dipping speed of 0.11 inch per second. The heating profile of the dipped fiber is shown in Figure 3-86 below. The fiber was fired in air below 600°C and in nitrogen above 600°C. The nitrogen was admitted to the oven 15 minutes into the 600°C dwell step.

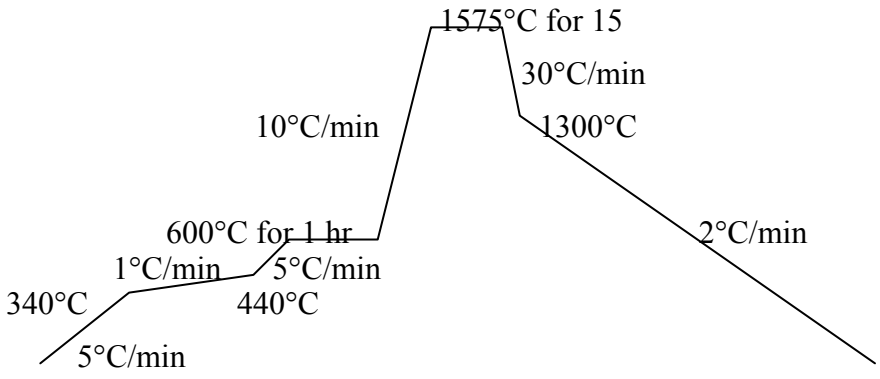

Figure 3-86. Heating profile used to process magnesium aluminate spinel coating on fiber for numerical aperture test.

The measurement setup was then used to measure the numerical aperture for this clad fiber. As Figure 3-87 shows, the acceptance angle was reduced to approximately 2°. Applying the definition above, the NA of the clad sapphire fiber is found to be approximately 0.3.

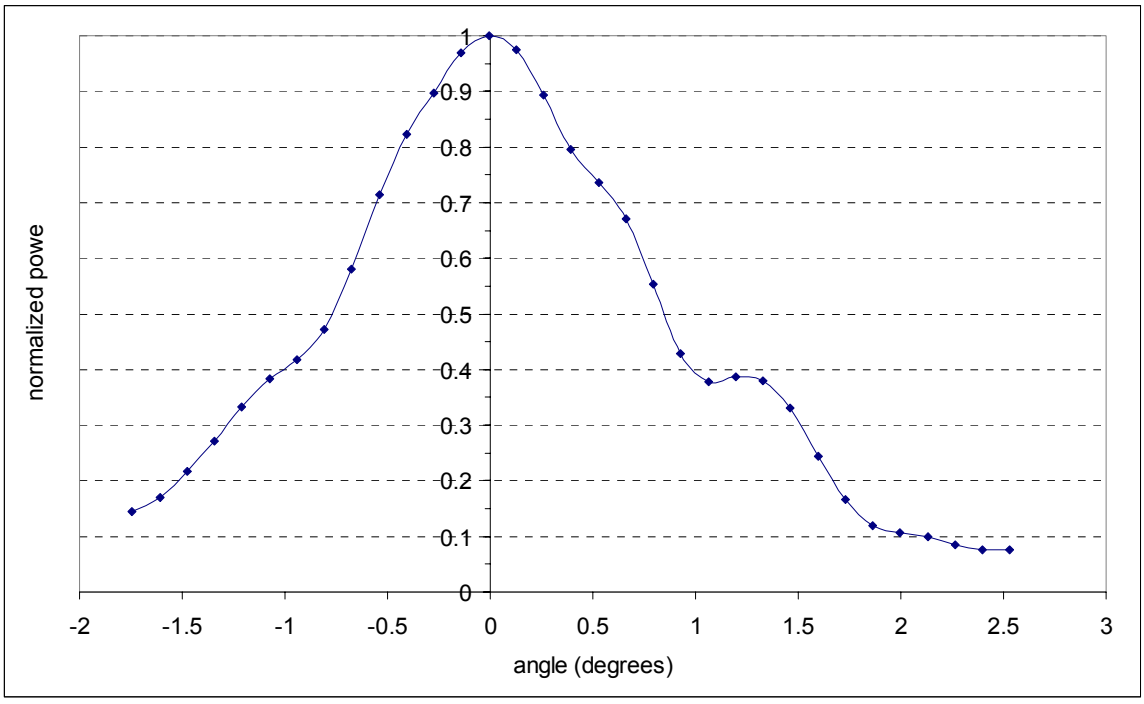

Figure 3-87. Plot of the normalized output power for clad sapphire fiber as a function of angle of incidence of input light.

This value is in order of magnitude lower than that predicted by Equation 4. The reason for this is unknown and still under investigation, but a leading hypothesis is that a rough interface between the core and cladding in the coated fiber (seen in some of the photographs in the previous section) causes more scattering and stronger losses in higher-order modes rather than lower modes, thereby reducing the numerical aperture. Figure 3-88 combines the data from Figure 3-85 and Figure 3-87 onto a single semi-log plot. From the figure, it's clear that the transmission is strongly attenuated in the clad fiber, with the peak output (at 0°) about 15 dB down from that of the unclad fiber.

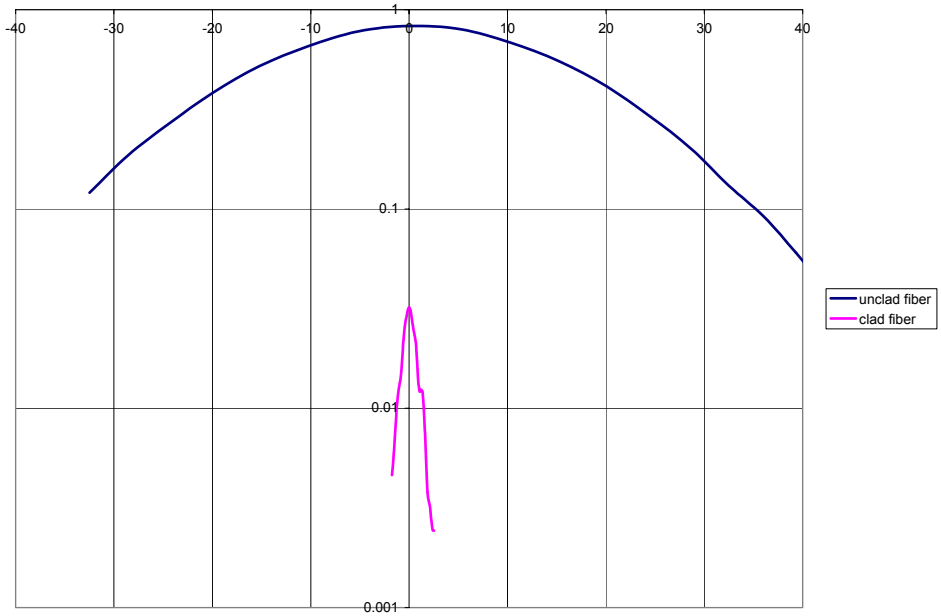

Figure 3-88. Comparison of far-field intensity distributions for unclad and clad sapphire fiber, on semi-log plot.

3.2.2.8.1 Calculation of Mode Volume

From electromagnetics theory, the number of electromagnetic modes guided by a step index multimode fiber may be estimated from the geometric and optical properties of the fiber. The number of guided modes N is given by

$$N = \frac{16 \cdot a^2}{\lambda^2} \cdot NA^2$$

Equation 6

where a is the radius of the core of the fiber, and λ_0 is a wavelength of light used to measure the numerical aperture.

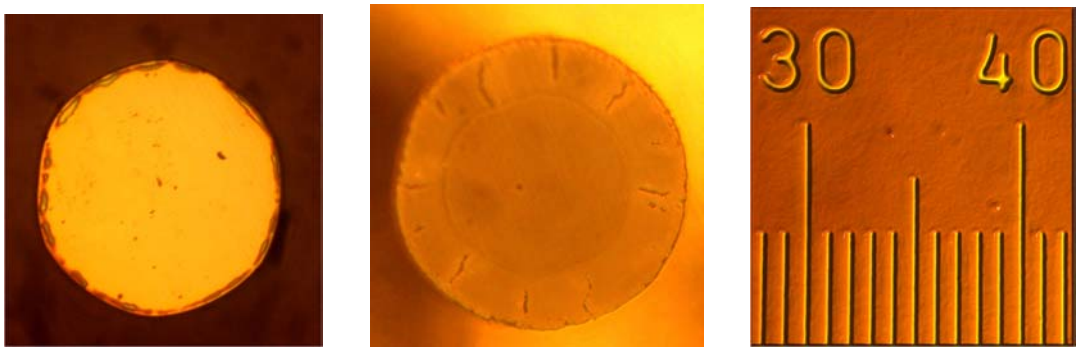

Figure 3-89. Photomicrographs of (a) unclad sapphire fiber, (the) clad sapphire fiber, and (see) graticule at same magnification as (a) and (b). Each division in (c) is ten micrometers.

From photomicrographs of the polished ends of the unclad and clad sapphire fibers (Figure 3-89), the core diameters of the fibers were measured. The diameter of the unclad fiber was measured to be 122 μm; the outside diameter of the clad fiber was found to be 137 μm, with a core diameter of 86 μm. Using these measurements for the unclad sapphire fiber, the number of guided modes propagating in the fiber is estimated to be approximately 52,000. In contrast, the number of guided modes for the clad sapphire fiber is estimated to be 66.

The reduced mode volume in the clad fiber was also confirmed by examining the far-field intensity distribution of the clad sapphire fiber. Figure 3-91 shows the far-field radiation pattern output by the clad sapphire fiber. To obtain this image, the output of a helium neon laser was focused on to the end of the clad sapphire fiber using a 60x microscope objective, with a NA of 0.65, as shown in Figure 3-90. A CCD array, connected to a computer-based image acquisition system, was positioned approximately six inches from the output end of the fiber. The intensity distribution of the far-field pattern shows a few maxima consistent with interference from a few (less than 100) propagating modes. For comparison, Figure 3-92 shows the far-field pattern from a graded index multimode fiber with a 100 μm core, which supports the propagation of thousands of modes.

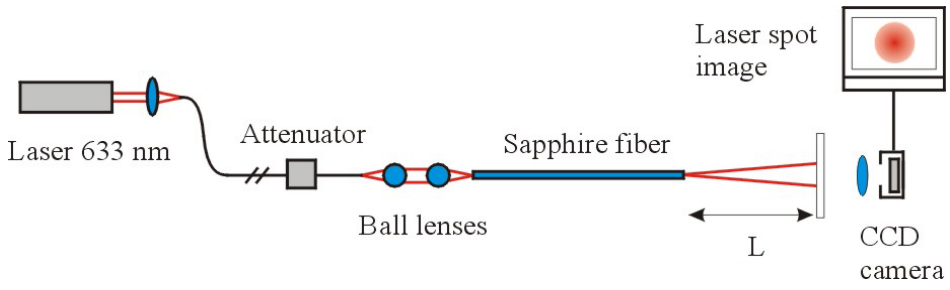

Figure 3-90. Set-up for imaging far-field intensity distribution from sapphire fiber.

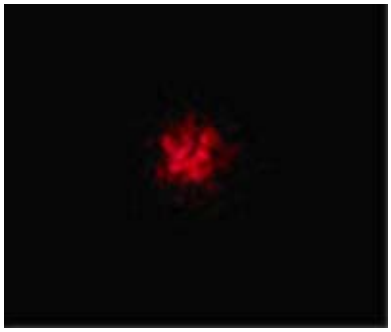

Figure 3-91. Far Field Radiation Pattern from Output of Clad Sapphire Fiber

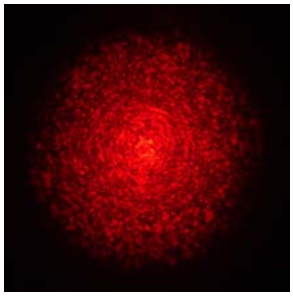

Figure 3-92. Far-Field Radiation Pattern Output by a 100 μm Core, Graded Index Multimode Fiber

3.2.2.9 Sapphire Sensor Development by Index Modulation

Techniques for local (on a small spatial scale) modification of the refractive index of a sapphire fiber in order to generate in-line (i.e. in the fiber) sensors were investigated. Two specific approaches were considered: periodic modification of the index to form grating structures in the fiber (both fiber Bragg gratings and long period gratings), and short (< 1 mm) step changes in index to form intrinsic Fabry-Perot interferometers (IFPIs).

Grating-based sensors and Fabry-Perot sensors have been extensively researched in traditional glass optical waveguides such as optical fibers. Optimal function of the sensors requires single-moded waveguides; in multimode waveguides, the response of the sensor to each guided mode is different, due to differing phase constants of each guided mode when it interacts with the sensor structure. The total sensor response is a superposition of the responses of all of the modes to the sensor structure; the overlapping responses tend average out, washing out the total sensor response.

One solution to the problem is to restrict the launch conditions of the light injected into the waveguide, so that only a small number of modes are excited in the fiber. This

approach has been used successfully in the past with straight, inflexible sapphire rods.[13] However, since bends or splices or connectors in the fiber can cause a redistribution of power into a larger number of modes, this strategy is limited in practice to applications were bends, splices, and connectors can be avoided. This limitation is the motivation for the development of high-temperature claddings for sapphire fiber in order to reduce the mode volume of the sapphire fiber.

3.2.2.9.1 Fiber Bragg gratings sensors

Fiber Bragg gratings (FBG) have several attributes that make them attractive for sensor systems. In particular, large numbers of FBG elements may be concatenated in order to achieve sensing along a single fiber. A number of schemes for interrogation of serially multiplexed FBGs have been developed.

Fabrication of FBGs in glass fibers relies upon the photosensitivity of germania-doped silica. The formation of FBGs is usually classified according to three distinct dynamic mechanisms. Type-I photosensitivity corresponds to a monotonic increase in the amplitude of refractive index modulation from exposure of a germania-doped silica core to intense UV radiation of the appropriate wavelength. Generation of color centers associated with UV-induced effects in the GeO_2 dopant is responsible for the refractive index modulation. Since color centers can be annealed by heat treatment, Type I FBGs are not stable at high temperatures, and can be erased at relatively low temperatures, approximately 200°C.

Protracted exposure of Type-I gratings to UV radiation will result in partial or complete erasure, followed by a large negative refractive index change. The resulting grating is classified as a Type-IIA grating (sometimes called Type III). It is assumed that the refractive index change with exposure time results from two local reactions. The first produces some defects or chemical species that lead to the positive index change; the second is slower than the first, and produces negative index change through structural reorganization. This structural reorganization is known as compaction of fiber.

Type-IIA photosensitivity can lead a refractive index change to about $1x10^{-3}$ or even higher. A noticeable erasure is observed at temperature above 500°C.

Type-II gratings are distinct from other grating types. They are formed under very high, single-pulse fluences (>500mJ/cm^2). Unlike Type-I and Type-IIA gratings, Type-II gratings can be obtained by using a high-power excimer laser. It is apparent that there is a threshold at pulse energy density of about 650mJ/cm^2. When pulse energy is below the threshold, refractive index changes linearly. But refractive index change increases dramatically above this threshold. When the pulse energy is higher than 1000mJ/cm^2, the refractive index change will begin to saturate.

---

[13] A. Wang, S. Gollapudi, R.G. May, K.A. Murphy, and R.O. Claus, "Advances in Sapphire-Fiber-Based Intrinsic Interferometric Sensors," *Optics Letters*, 11/1/92, Vol. 17, No. 21.

It is believed that Type-II photosensitivity is caused by the result of damage at the core-cladding interface. Type-II photosensitivity can lead to a refractive change as high as 1%. Type-II gratings show good stability to high temperature, withstanding temperatures as high as 800°C. Due to the damage at the interface of fiber core and cladding, the fiber becomes fragile at the writing point. This may be a potential problem if the sensor is not protected.

Fiber Bragg gratings have only recently been demonstrated in sapphire fibers.[14] These were achieved by the exposure of sapphire fibers with the output of a 800 nm femtosecond Ti: sapphire laser through a phase mask. The index modulation in this case is associated with multi-phonon ionization. Use of a femtosecond laser appears to be critical to achieve threshold fluence for ionization without heating the fiber with long pulse widths.

3.2.2.9.2 Sapphire Intrinsic Fabry-Perot Interferometric Sensors

As explained in Section 3.2.1.1.2, in-line, or intrinsic, Fabry-Perot interferometric sensors have several features that make them attractive for measurement of physical quantities at discrete points along an optical fiber. Due to the low insertion loss of a typical IFPI sensor, many IFPI sensors can be concatenated on a single fiber without suffering significant penalty to the optical loss budget of the sensor system. Since the sensor is interferometric, high sensitivity is possible with appropriate designs, and a number of sensor interrogation methods for interferometric sensors may be applied to read out the IFPI sensors. Virginia Tech's Center for Photonics Technology has demonstrated the use of optical time domain reflectometers (OTDR) to demultiplex three IFPI sensors. Several groups, including Prime Research, have investigated the use of digital signal processing to deconvolve individual sensor responses from the spectral output of an optical fiber with multiplexed IFPI sensors.

During the Phase I research reported here, Prime Research investigated the fabrication of IFPI cavities in sapphire fibers. Since sapphire fibers do not exhibit the same sensitivity to UV radiation that germania-doped silica fibers do, a UV laser was not used in these studies. Instead, magnesium oxide was bulk diffused into unclad sapphire fibers over short (< 1mm) longitudinal segments of the fiber, in order to locally modify the refractive index over that length and define an intrinsic Fabry-Perot cavity.

Two configurations were attempted to the fabrication of sapphire IFPI sensors. In the first configuration, magnesium oxide (in a magnesium aluminate spinel slurry) was applied to the surface of a sapphire fiber over a short (< 1 mm) length of the fiber. The coated fiber was then fired in a furnace in order to promote diffusion of the magnesium oxide into the sapphire fiber, in the hopes of reducing the refractive index over the short coated segment, forming an IFPI cavity.

[14] D. Grobnic, S.J. Mihailov, C.W. Smelser, and H. Ding, "Sapphire Fiber Brag Grading Sensor Made Using Femtosecond Laser Radiation for Ultrahigh Temperature Applications," IEEE Photonics Technology Letters, Vol. 16, No. 11, Nov. 2004, pp 2505 – 2507.

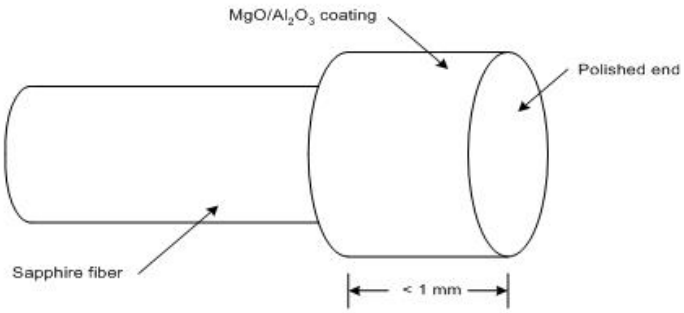

Figure 3-93. Geometry of completed sapphire IFPI sensor.

To construct a sensor of this first configuration, one end of a length of unclad 125 μm diameter sapphire fiber (typically 4 inches in length) was dipped into a magnesium aluminate spinel slurry so that the coating was built up over a few millimeters of the end of the fiber. The fiber was masked with polyimide tape (a few millimeters were left uncovered at the end of the fiber), so that a distinct transition could be achieved between the coated fiber and the uncoated fiber. After a suitable number of layers of spinel had been applied to the fiber, the tape mask was carefully removed, and the partially coated fiber was fired in a furnace according to the schedule shown in Figure 3-86. The fiber was then removed from the furnace, and the coated end was polished to an optically smooth finish perpendicular to the axis of the fiber, through the use of a polishing wheel using diamond polishing media. The initial polish was conducted using coarse media until the length of the coated section of the fiber was less than 1 mm, as shown in Figure 3-93. Upon completion of this process, the length of the sapphire fiber was measured using calipers to be 48 mm long, and from Figure 3-94, the coated section of the fiber was estimated to be approximately 488 μm in length.

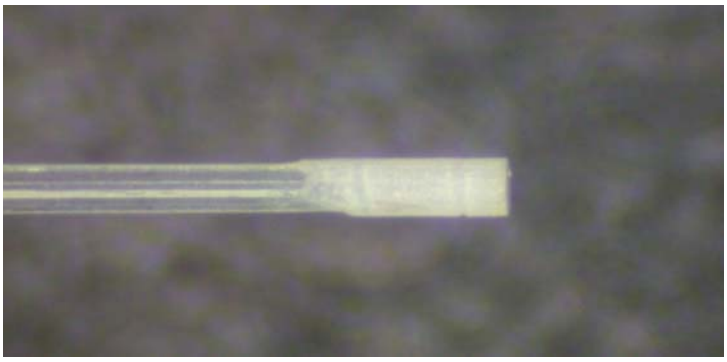

Figure 3-94. Photomicrograph of completed (fired) coating on end of sapphire fiber.

To evaluate the treated fiber and determine if an IFPI cavity was formed within the sapphire fiber, the experimental setup illustrated in Figure 3-95 was employed. The Micron Optics Component Test System (CTS) si720 is a swept laser spectrometer which was configured to analyze the spectral reflection from the sapphire fiber as its internal laser was swept from 1520 nm to 1570 nm. A single-mode fiber (SMF) patch cord was used to connect the CTS to the sapphire fiber. The far end of the patch cord from the CTS was terminated in a FC/APC fiber optic connector polished at 8° angle. The end of the sapphire fiber that was not modified to form the IFPI was also polished at 8° angle. The angled ends on the fibers are used to reduce the finesse of the Fabry-Perot cavity that may be formed between the sapphire fiber and SMF patch cord, to reduce the strength of any interferometric fringes formed in the air gap between the fibers. A three axis micropositioner was used to align the sapphire fiber input end to the fiber end in the FC/APC connector.

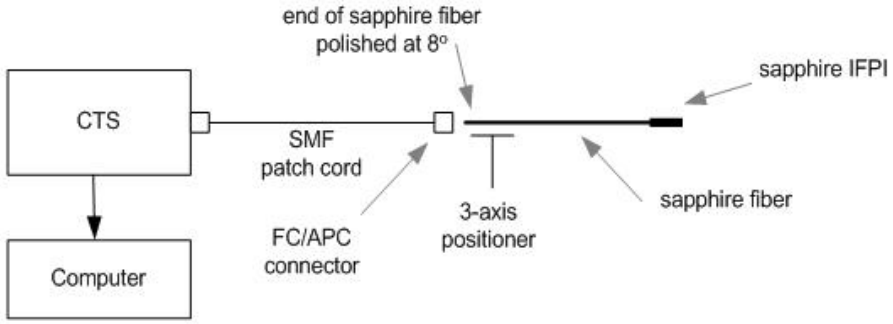

Figure 3-95. Experimental setup used to evaluate sapphire IFPI sensor. "CTS" is a Micron Optics Component Test System si720.

The spectral output obtained from the sapphire fiber is reproduced in Figure 3-96. The spectrum is a complicated signal, with several frequencies apparent. In order to facilitate interpretation of the output, the signal was Fourier transformed, with the results shown in Figure 3-98. The result shows a strong frequency content associated with a wave number of 71 nm^{-1}, in addition to other peaks at lower frequencies. The 71 nm^{-1} wave number describes a spectral waveform with a wavelength of 14 pm. Using the expression relating the geometry of a Fabry-Perot cavity to its spectral output, the physical length L of the cavity is given by

$$L = \frac{\lambda^2}{2 \cdot n \cdot \Delta\lambda},$$

Equation 7

where n is the c-axis refractive index of sapphire, $\Delta\lambda$ is the wavelength of 14 pm, and λ is chosen to be the wavelength at the center of the CTS scan (1545 nm). Upon substitution of these values into the equation, the physical length of the cavity associated with this

peak is found to the 48 nm, which agrees nicely with the measured length of the sapphire fiber. Therefore, the peak found at a wave number of 71 nm^{-1} is associated with fringes resulting from the Fabry-Perot cavity formed by the length of sapphire fiber.

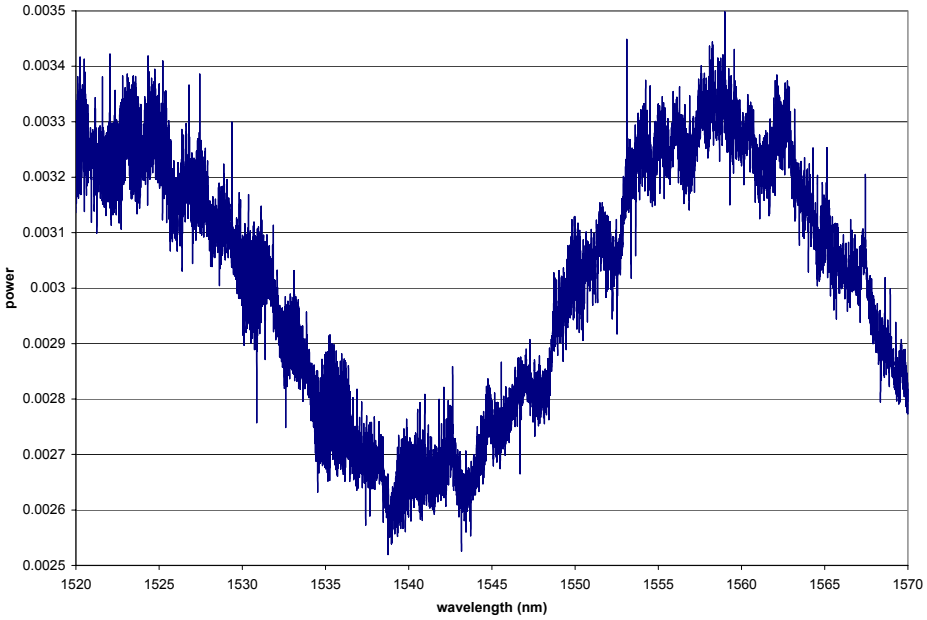

Figure 3-96. Spectral output of sapphire fiber with IFPI cavity, as measured by the CTS.

In order to analyze the lower frequency peaks, the Fourier spectrum is expanded to show the lower frequencies in Figure 3-98. Three additional peaks are seen in the spectrum from zero to 6 nm^{-1}. The lowest of these, with a wave number of 0.02 nm^{-1}, is associated with fringes with a period of 50 nm, which is clearly the waveform with the largest amplitude in Figure 3-96. Using Equation 7 again, this period is associated with a cavity of optical path length of 24 μm. This cavity was due to a 24 μm gap between the sapphire fiber end and the fiber end in the FC/APC connector; due to an inability to rotate the fibers to align the angled fiber ends to a parallel state, the air gap was present and responsible for this peak in the Fourier spectrum.

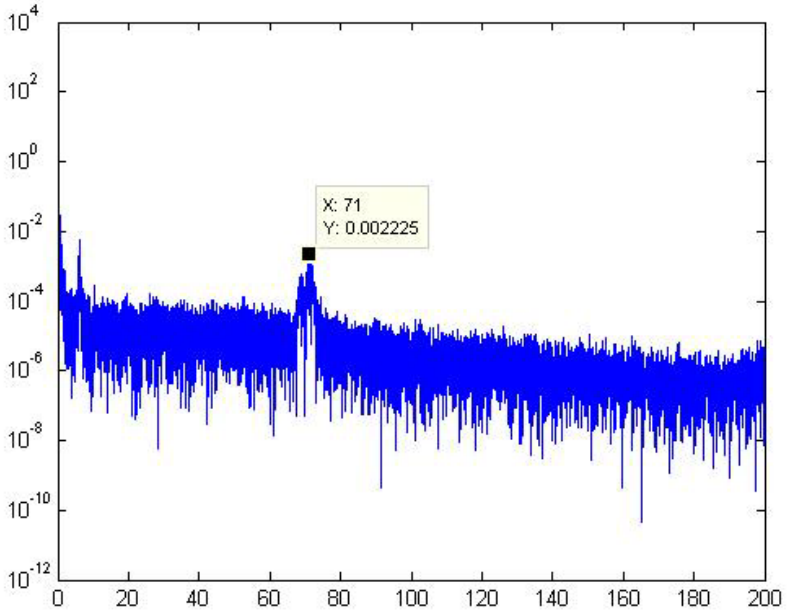

Figure 3-97. Fourier transform of data in Figure 3-96.

The second peak in Figure 3-98 is associated with a fringe of period 2.17 nm. Using the equation for the Fabry-Perot output, this fringe should be generated by a cavity with an optical path length of 550 μm. If we assume that this cavity is the IFPI cavity resulting from diffusion of magnesium oxide into the sapphire fiber, then the local refractive index should be 1.723, and the resulting physical cavity length would be 550 μm/1.723, or 319 μm. This calculated value for the physical cavity length is approximately 150 μm less than the estimate for the coated section of the fiber obtained from Figure 3-94.

The origin of the third peak is as yet unclear. With a wave number of 6 nm^{-1}, the associated fringe period is 0.16 nm, which yields an estimated cavity optical path length of 7.45 mm. No physical features were observed in the fiber corresponding to this length, or to a length of 4.22 mm, which is found by dividing the optical path length by the refractive index of sapphire. Tests are continuing in order to analyze this sapphire IFPI sample, in addition to others that are being fabricated.

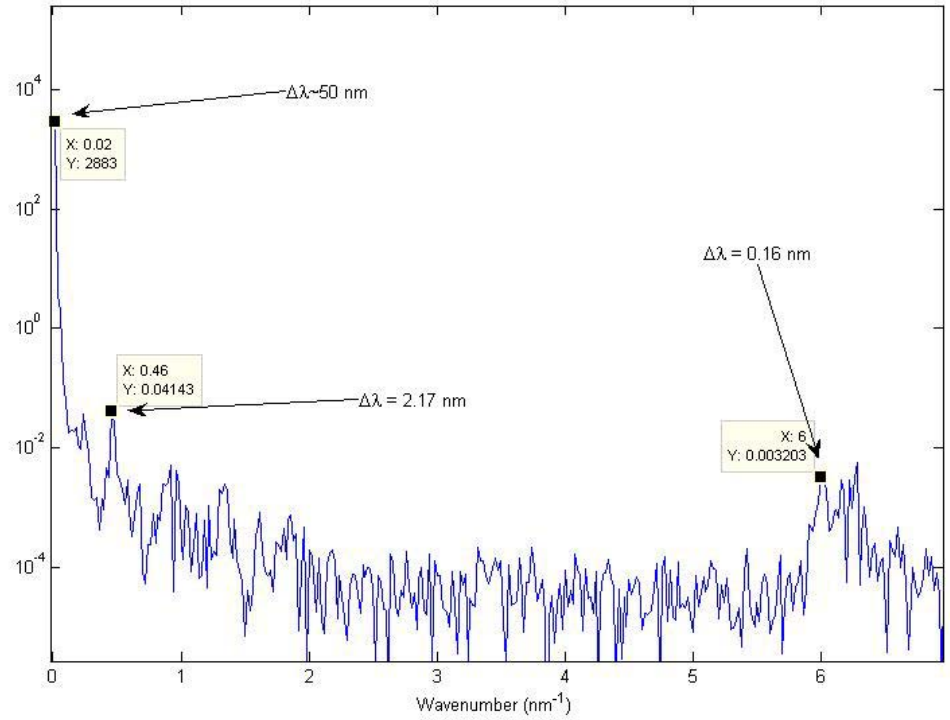

Figure 3-98. Zoomed view of the low frequency portion of Figure 3-97.

The second approach that was investigated in Phase I for fabrication of IFPI cavities in sapphire fibers is illustrated graphically in Figure 3-99. A magnesium alumina spinel coating is applied to a sapphire fiber in the usual way by dipping; however, this coating is not fired in a furnace. Instead, the fiber is fixed on a motorized rotary stage so that it can be rotated around the axis of the fiber. While the fiber rotates, the output of a CO2 laser is focused to a point on the surface of the spinel coating. As the fiber rotates, this focal point traces out a circumferential band on the coating. The intent is to heat the coating only in this circumferential band, resulting in a short band of magnesium oxide diffusion into the sapphire, to form an IFPI cavity of short length. One advantage of this approach over the previous one, in which the end of the sapphire fiber was polished to form one and of the IFPI cavity, is that IFPI cavities could be formed serially along the fiber.

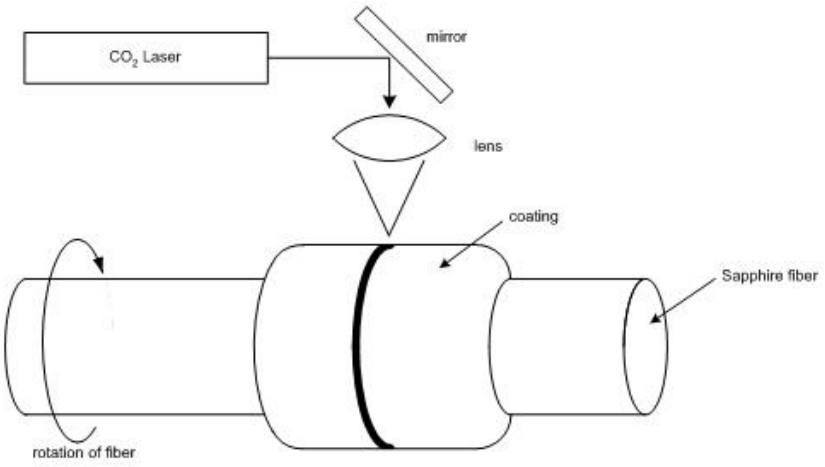

Figure 3-99. Experimental setup for selective firing of spinel coating to form IFPI in sapphire fiber.

Figure 3-100 is a photograph of the apparatus set up in the laboratory to heat the coated fibers using a carbon dioxide laser. The fiber was mounted in a can place, which in turn was mounted on a step or motor shaft. In the photograph, the beam delivery optics of the CO2 laser is seen in the upper right; the fiber is seen to incandescent due to the heating in process.

Work on this approach continues to date. Critical parameters that are being determined include optimal rotational rates, laser output power, and period of irradiation.

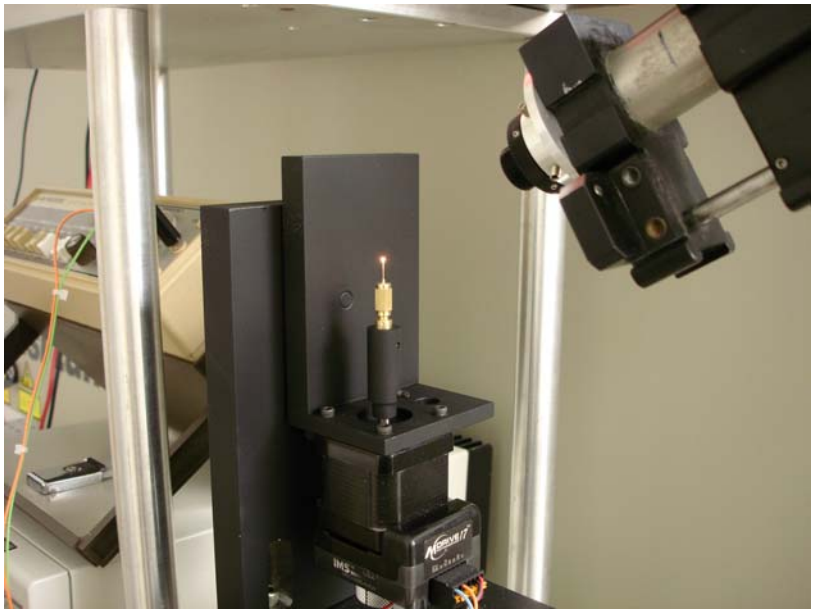

Figure 3-100. Photograph of fixture to rotate coated sapphire fiber while the radiating fiber by output of CO_2 laser.

3.2.3 High-temperature Sensor Tests

A temperature sensor was designed and constructed to demonstrate a use of sapphire fibers for making measurements at high temperature. In the sensor design, changes in temperature result in a change in the length of a sapphire fiber, and the length change is detected interferometrically. For this test, the sensor was evaluated up to 775° C.

Optical sensors fabricated using sapphire fiber have some benefits in comparison with silica-based glass fiber sensors, in particular suitability for use over a long times in high temperatures and chemically harsh environments. However, unclad sapphire fibers are highly multimoded, making application of interferometry for sensitive measurements difficult. Existing sapphire displacement sensors are generally based on intensity modulation from transmission losses through gaps created by two fibers. Intensity modulation methods often achieve relatively low resolution in comparison to interferometry method, due to signal corruption by noise.

The design presented here attempts to combine the positive attributes of sapphire material with an interferometry type of displacement measurement. The design

- creates a Fabry-Perot interferometer cavity using sapphire and silica fibers
- use thermal expansion of sapphire fiber to measure high temperature
- separates and thermally isolates the interferometer cavity and part of sapphire fiber at high temperature

The sensor design is shown in Figure 3-101. A superluminescent diode (SLD) outputs light of peak wavelength 1533 nm, which is coupled into a silica fiber with core size 9.5 um. After passage to a 2 x 2 coupler the light is guided to the other end of the fiber, which is fixed in a zirconia ferrule with a flat polished surface. The ferrule is attached to a stage with three-dimensional linear and angle control. In our experiments we used a single crystal sapphire fiber (manufactured by Photran, Inc.) with total length of 145 mm and diameter of 127 um, and with the c-axis aligned along the fiber axis. The sapphire fiber was threaded through three ferrules: the end of the fiber farthest from the silica fiber was fixed (clamped) to a ferrule and secured in place using a high-temperature epoxy. The inner bores of the remaining two ferrules were size to be slightly larger than the sapphire fiber diameter, so that the fiber was free to translate longitudinally in the ferrules. Using micropositioners, the silica fiber end was positioned to face the sapphire fiber's free end, in order to create a Fabry-Perot cavity. The length of the cavity is changed as result of thermal expansion of sapphire fiber, or by moving silica fiber in the mechanical stage.

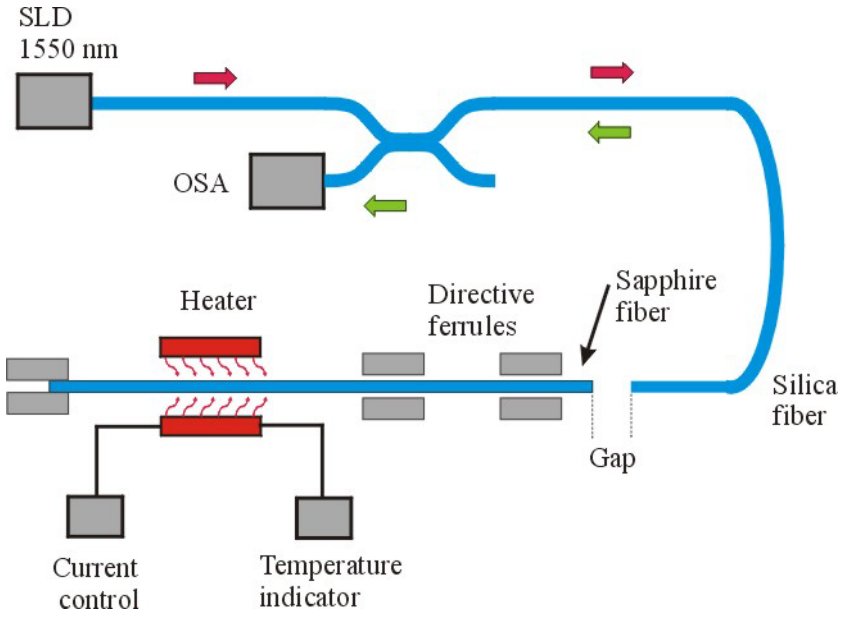

Figure 3-101. Schematic of temperature sensor using sapphire fiber. "SLD" is a superluminescent diode, and "OSA" is an optical spectrum analyzer.

Simple calculations were undertaken to determine the appropriate starting length of the cavity. Single-crystal sapphire fiber has a thermal coefficient of linear expansion of $\alpha = 8.8\text{x}10^{-6}\ ^{\circ}\text{C}^{-1}$ parallel to the c-axis. According to the relation for thermal expansion

$$\Delta L = \alpha L_0 (T_2 - T_1)$$

Equation 8

$\Delta L = 196\ \mu\text{m}$ for $L_0 = 33\ mm$ and interval of temperatures from $25^{\circ}C$ to $700^{\circ}C$.

To change the temperature of the sapphire fiber, we fabricated a miniature electrical heater by wrapping heat tape around an alumina tube. A thermocouple was placed inside to monitor the temperature, and a variable current transformer was used to adjust the temperature by controlling the current to the heat tape. The length of the heater was 33 mm. The heater and the sapphire fiber are shown in Figure 3-102, and the experimental set-up, including the miniature heater, is shown in Figure 3-103.

An Anritsu Optical Spectrum Analyzer (OSA) was used to detect fringes from the Fabry-Perot cavity. The gap size (separation between the sapphire fiber end and the silica fiber end) was calculated using the formula

$$d = \frac{\lambda_1 \lambda_2}{2(\lambda_2 - \lambda_1)},$$

Equation 9

where λ_1 and λ_2 are the peak wavelength as of two adjacent maxima in the interference spectrum of the sensor.

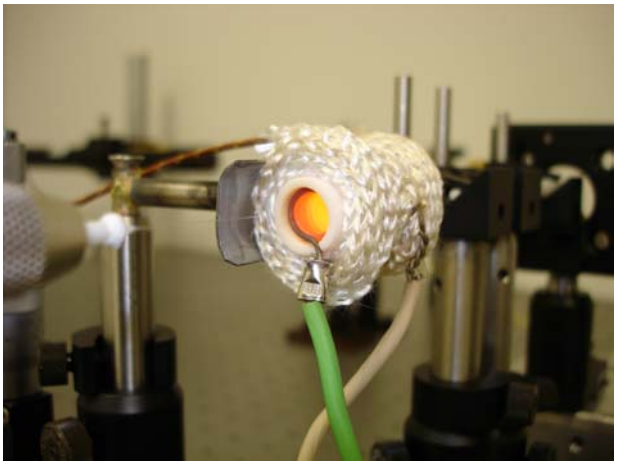

Figure 3-102. Miniature electrical heater.

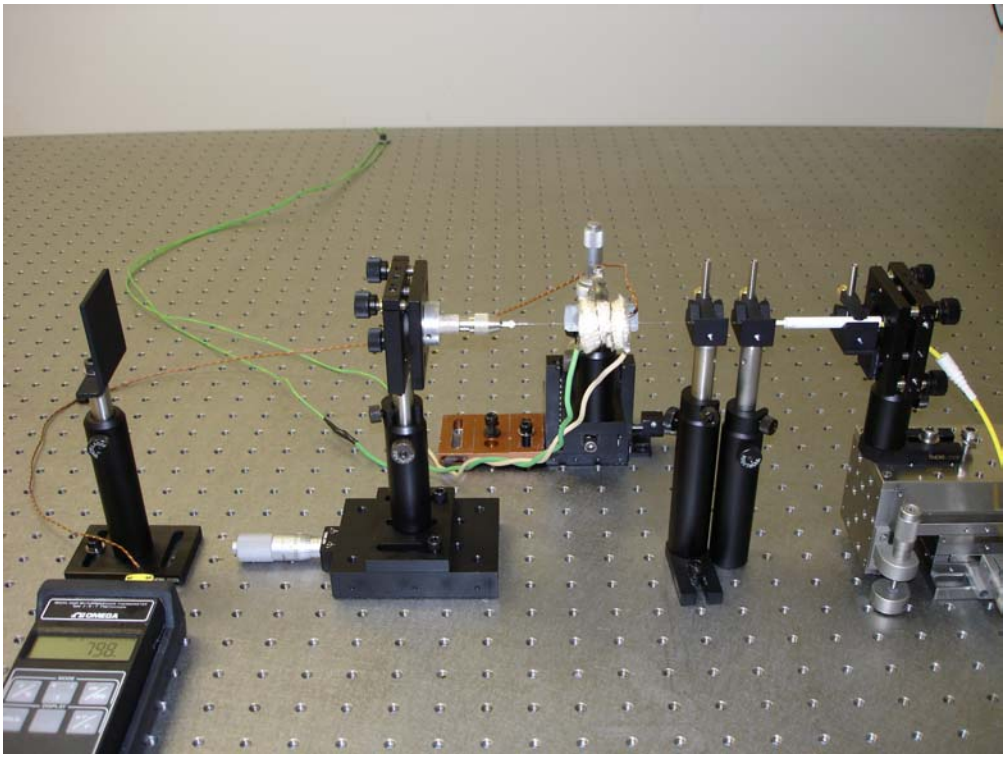

Figure 3-103. Experimental set-up for temperature sensor tests.

Some examples of the fringes for different temperatures are shown in Figure 3-104.

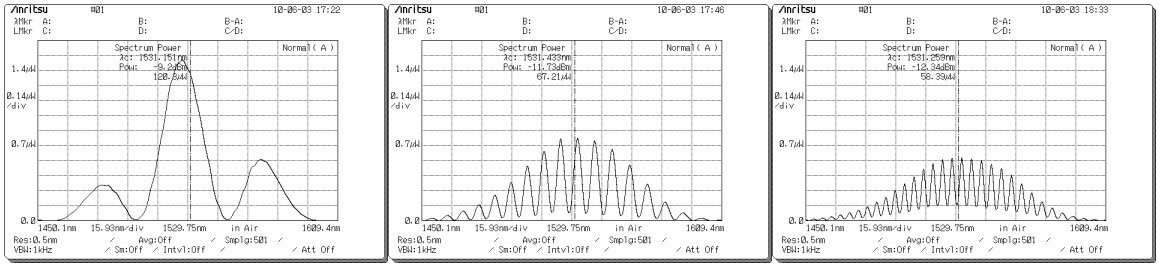

(a) (b) (c)

Figure 3-104 . Interference fringes for different temperatures.

(a) 750˚C, (b) 400˚C, and (c)24˚C

In the experiments, we set up the heater at maximum temperature, and then made a gap size correspond to two interference fringes indicated on OSA. The current of the heater was reduced. Then we waited for the temperature to lower until it became stable. To measure the fiber's temperature, we used a thermocouple placed in the center of the heater.

The results of the described measurements are indicated in Figure 3-105. Experimental data is presented by dots on the graph, and the linear fit by the solid line. The graph demonstrated that gap size linearly depends on temperature. The spread of values in experimental data is due to two reasons. The heater is not completely thermally isolated, and therefore the turbulence of air passing through the heater due to convection results in the fiber temperature being slightly unstable. Another reason is based on determining the peaks of the interference fringes manually. When the number of fringes are big or very small an error in the determination of the peak wavelength increases.

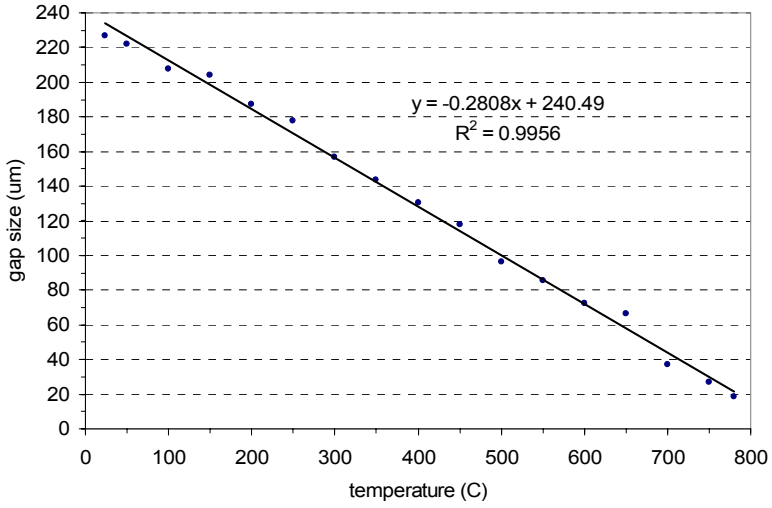

Figure 3-105. Measured calibration curve for sapphire sensor

4 RESULTS AND DISCUSSION

4.1 Assessment of Results

Based on the input from Babcock & Wilcox engineers, three specific locations were identified as primary candidates for sensor development in this program: the furnace water wall, secondary superheater tubes, and burners. Specific measurands of interest in these locations are temperature, pressure, and strain. Sensor research during the Phase II effort will target the development of sensors for the measurement of these parameters in the specific locations, using the requirements identified by Babcock & Wilcox in Table 3-1, Table 3-2, andTable 3-3. Sensor systems developed during the program will adopt communications protocols recommended by B&W, such as OLE for Process Control (OPC), as well as the recommended communication architectures, such as Fieldbus.

Laboratory tests were performed on several fiber optic sensor configurations, including interferometric (extrinsic and intrinsic Fabry-Perot interferometer), gratings (fiber Bragg gratings and long period gratings), and microbend sensors. The sensors were configured as temperature, pressure, or displacement sensors, as appropriate for the sensor method. The sensor performance was characterized in terms of sensor resolution, with the results tabulated in Table 4-1.

Sensor type	Interrogator	Tested range	Resolution
EFPI	Micron Optics CTS	200° C	2.5°C (1.25% FS)
IFPI	Micron Optics CTS	300° C	1.1° C (0.4% FS)
FBG	Micron Optics CTS	500° C	0.17°C (0.04% FS)
LPG	Anritsu OSA	80 psi	4.4 psi (5.5% FS)
Microbend	Computer DAQ	0.05 μm	25 μm (0.2% FS)

Table 4-1. Results from sensor evaluation

Methods for applying magnesium aluminate spinel coatings to sapphire fibers to function as optical claddings were researched. Magnesium alumina spinel is well-suited for cladding of sapphire fibers due to its high melting temperature, refractive index slightly less than that of sapphire, and coefficient of thermal expansion closely matched to that of sapphire. Application of spinel coatings involves dipping the sapphire fiber in a slurry of spinel and magnesium oxide powders, firing the slurry on the fiber, and then sintering the coating to densify it on the fiber.

An investigation was undertaken in which certain parameters such as the firing profiles, the slurry dipping procedures, the atmosphere of firing, the particle sizes of the powders, and a slurry compositions were systematically varied. Results indicate that a smooth interface between the sapphire core and spinel cladding can be achieved through a carefully tailored firing procedure in argon atmospheres. In addition, it was found that the core diameter of the sapphire fiber can be reduced by a specified amount through the addition of a specified proportion of magnesium oxide in the slurry. We have

successfully fabricated spinel clad sapphire fibers with reduced cored diameters and smooth core/cladding interface with promising light guiding properties.

In the second half of the Phase I program, specific investigations directed to improvement of the magnesium aluminate spinel cladding included

- Incorporation of nanopowders into the slurry.
- Use of a "mixed solid spheres" model to increase the powder packaging density in the coating when combining MgO and $MgAl_2O_4$ (spinel) powders.
- Measured the particle sizes of each type of powders.
- Separated dispersion milling from binder milling to prevent agglomeration of powders.
- Explored different dispersants, and measured the optimal dispersant amounts using sedimentation tests.
- Performed TGA measurement on polyvinylpyrrolidone (PVP) binder to determine its burnout temperature.

Measurements of numerical aperture performed on a clad sapphire fiber were an order of magnitude lower than values predicted analytically from the refractive indices of the fiber and cladding. The reason for this is unknown and still under investigation, but a leading hypothesis is that a rough interface between the core and cladding in the coated fiber causes more scattering and stronger losses in higher-order modes rather than lower modes, thereby reducing the numerical aperture. Comparisons between the signal strengths transmitted by the clad fiber and the unclad fiber indicate high attenuation in the clad fiber. Understanding the reasons for this will be a high priority in Phase II.

Modification of sapphire fibers by doping with impurities was investigated, with a goal of creating fiber Bragg gratings or intrinsic fabric Perot interferometer sensor elements in sapphire fibers. Creation of an IFPI cavity in 125 μm diameter sapphire fiber was attempted by bulk diffusion of magnesium oxide into short (less than 1 mm) segments of sapphire fiber. The complex spectrum that resulted showed evidence of four cavities in the fiber: one was clearly due to the entire length of the sapphire fiber, and one was clearly due to the gap between the sapphire fiber and the spectrometer's silica fiber pigtail. Of the two remaining cavities, one could not be correlated with any features in the sapphire fiber, while the other appeared to be associated with the Fabry-Perot cavity resulting from the diffusion of MgO. These results, while not conclusive, are convincing enough to warrant continued investigation.

4.2 Plans for Phase II

4.2.1 Sensor design

Based on experimental evaluations of candidate sensor designs concluded at the end of the first year, and employing the set of requirements for supercritical boiler plant instrumentation determined in the first year of the program, a sensor suite will be finalized. The sensor suite will comprise a set of different sensor applications for

monitoring of different processes within the plant. A requirements document will be generated for each sensor application in the suite.

For each sensor application, a final sensor design configuration will be identified. Each sensor design configuration will consist of an optomechanical design for the probe, an optoelectronic signal conditioner to interface in the probe to an electronic control system or data acquisition system, and a specialized high-temperature optical cable to interconnect the probe to the signal conditioner. Requirements for the cable design (optical and mechanical properties) will be determined for each sensor configuration.

Prototype sensors for each of the sensor design configurations will be fabricated, and then laboratory tested in environments representative of the field tests planned for the third year of the program. In addition, sapphire fibers required for the sensors will be fabricated. The sapphire fibers will be tested and evaluated for mechanical and optical performance at high temperature.

Fabrication of sensor systems and high-temperature fiber will continue into the third year the program, leading to field tests in a Babcock and Wilcox powerplant.

4.2.2 Designed experiments for optimizing processing of clad sapphire fiber

The Taguchi method is a technique for designing and performing experiments where the output depends on many factors, without tediously and uneconomically running the experiment using all possible combinations of values of those factors. By systematically choosing certain combinations of variables it is possible to separate their individual effects.

In the current project, a sapphire fiber is dip-coated in the slurry prepared using a variety of oxide powders and additives including dispersant and binder. In the high-temperature firing step, the magnesium oxide particles in the coating diffuse into the sapphire fiber and form the spinel cladding surrounding the fiber. A goal of this project is to fabricate mechanically strong spinel cladding with an optically smooth cladding/core interface. Many factors, including the type and amount of dispersant and binder, weight ratio of the magnesium oxide and spinel powders in the slurry, coating speed and number of dips, and the final firing profile, affect the outcome. It is difficult and tedious to sort out the individual effect of each factor without a systematically designed set of experiments. It is ideal in this situation to implement the Taguchi method to design the proper experimentation. Prof. Gary Pickrell at Virginia Tech guided the establishment of the Taguchi process for this portion of the program.

After careful review of the system of interest, it was decided to implement the “L18 Orthogonal Array” which consists of eighteen experiments with seven 3-level factors and one 2-level factor. The L18 array is shown in Table 4-2 below. Each of the eighteen rows

represents one coated sapphire fiber sample prepared using the corresponding factor and level in each column.

The performance of each clad fiber is judged using the following six criteria:

1. Optically smooth cladding/core interface;
2. Proper relative index of refractions between the sapphire core and the spinel cladding that can support light propagation;
3. A mechanically strong spinel cladding with the least amount of cracking;
4. Uniform cladding thickness along the whole length of the fiber;
5. Smooth and crack free surface of coated fibers after drying, binder burnout, and final firing.

			Columns					
EXPT NO	**1**	**2**	3	4	5	6	7	8
1	**1**	**1**	1	1	1	1	1	1
2	**1**	**1**	2	2	2	2	2	2
3	**1**	**1**	3	3	3	3	3	3
4	**1**	**2**	1	1	2	2	3	3
5	**1**	**2**	2	2	3	3	1	1
6	**1**	**2**	3	3	1	1	2	2
7	**1**	**3**	1	2	1	3	2	3
8	**1**	**3**	2	3	2	1	3	1
9	**1**	**3**	3	1	3	2	1	2
10	**2**	**1**	1	3	3	2	2	1
11	**2**	**1**	2	1	1	3	3	2
12	**2**	**1**	3	2	2	1	1	3
13	**2**	**2**	1	2	3	1	3	2
14	**2**	**2**	2	3	1	2	1	3
15	**2**	**2**	3	1	2	3	2	1
16	**2**	**3**	1	3	2	3	1	2
17	**2**	**3**	2	1	3	1	2	3
18	**2**	**3**	3	2	1	2	3	1

Table 4-2. L18 array (2^1x3^7) orthogonal array

The eight factors and their designated levels are listed in Table 4-3 below. The levels are tentative and may be changed in the future if necessary.

Factor number	Factor	Number of Levels	Level		
			1	2	3
1	Type of dispersant	3	Fish oil	Darvan 811,	PVP
2	Amount of dispersant	3	0.1 w.%	0.5 w.%	0.9 w.%
3	Amount of binder (PVP) added	3	3 w.%	5 w.%	10 w.%
4	Weight ratio of powders (MgO : spinel)	3	3:1	4:1	5:1
5	Ultrasonic step	3	None	30 seconds	60 seconds
6	Dipping speed	3	0.1 inch/sec	0.15 inch/sec	0.3 inch/sec
7	Numbers of dips	3	50	100	150
8	The firing profile	2	Profile 1	Profile 2	

Table 4-3. Tentative factors and the levels of each factor

Each criterion will be discussed in details in the following paragraphs.

1. Optically smooth cladding/core interface

The quality of this response is to be judged by three criteria:

1.1 The concentricity of the cladding/core interface, that is, the degree of deviation of the interface from a perfect circle, is examined. First, the average distance between the interface and the center of the fiber is calculated, and a circle with a radius equal to the average distance is drawn overlapping the interface as shown in Figure 4-1. Finally, the root mean square difference between the circle and the interface in the radial direction at each unit segment of the interface is calculated.

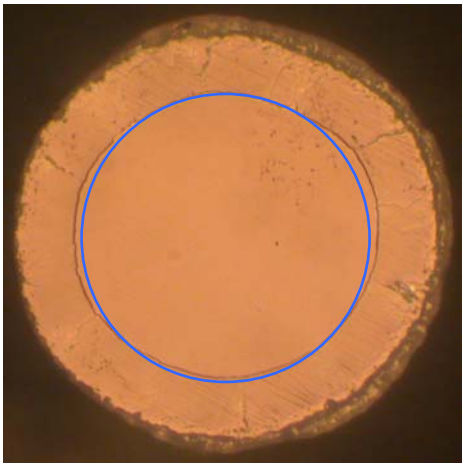

Figure 4-1. Determination of concentricity.

1.2 The second criterion is related to the smoothness of the interface itself. The procedures can best be illustrated by using a clad fiber with a typical rough interface as shown in Figure 4-2. In this figure, besides six large cracks with approximate hexagonal symmetry in the cladding, a zigzag core/cladding interface is clearly visible. The lower left corner of the core/cladding interface in Figure 4-2 is zoomed as shown in Figure 4-2. In order to measure the degree of smoothness of the interface, a running average of the interface is drawn along the interface as shown in Figure 4-2 as a, dotted blue curve, which can be drawn by naked eyes quite close to the accurate running average curve mathematically derived. The rigorous derivation of this curve will not be provided here as this moment. At each small unit segment on the curve, a line perpendicular to the curve shown as the dotted arrows in Figure 4-2 is drawn to intersect the core/cladding interface, and the root mean square difference between the curve and the interface is calculated as an indication of the degree of roughness of the interface.

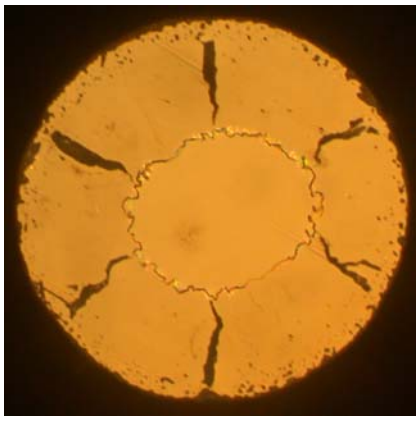

Figure 4-2

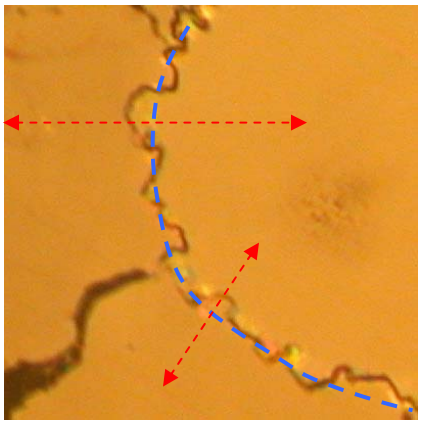

Figure 4-3

1.3 Another type of rough interface is shown in Figure 4-4, where granular, shiny, and thick sections of the interface occur in an otherwise smooth contour of the interface. Figure 4-4 is a local zoom at the upper left portion of the core/cladding interface in Figure 4-2. To evaluate the smoothness of the interface, the lengths of the widest sections are measured, and then the average width of the interface is calculated at each unit section of the interface. Both parameters are used to evaluate the smoothness. There are other occasions of the clad fibers where the entire interface is thick and granular; in these cases the same procedures described here can be implemented.

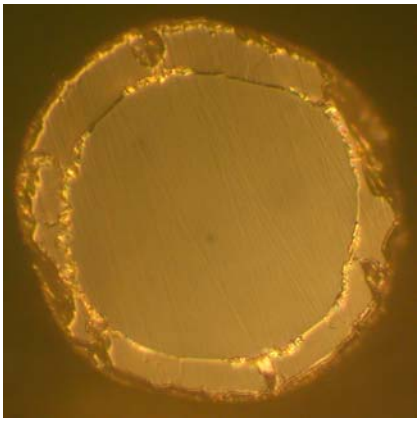

Figure 4-4

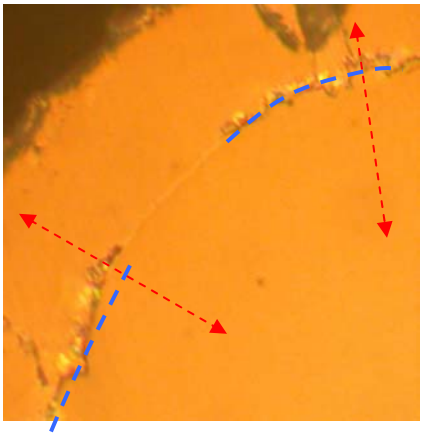

Figure 4-5

2. Proper relative index of refractions between the sapphire core and the spinal cladding that can support light propagation

Instead of directly measuring the indices of the spinel cladding and that of the sapphire core, the light guiding quality of clad fibers 6 inches long are examined by measuring the attenuation and the numerical aperture (NA) of the clad fibers. Both ends of the fibers are polished using diamond papers with abrasive sizes down to 0.5μm. The attenuation and NA of the original sapphire fibers without cladding are measured as the reference of comparison.

3. A mechanically strong spinel cladding with the least amount of cracking

Methods to quantitatively determine the mechanical strength of the clad fibers have not yet been implemented. However, the cracking in the cladding can be evaluated by both the lengths and the widths of the cracks. The methods are illustrated in Figure 4-6, in which the lower right crack in the clad fiber shown in Figure 4-2 is magnified. In this figure the unit length of the crack, L, is depicted a segment of blue line parallel to the crack, and the width of the crack, W, is depicted as the segment of red line perpendicular to the length of the crack. The degree of cracking of this segment of the crack is then designated as $L \times W$. All other segments of all cracks in the cladding are measured in the same way, and the sum of all $L_i \times W_i$ are calculated as the degree of cracking in the cladding for this sample.

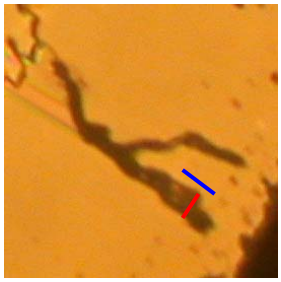

Figure 4-6

4. Uniform cladding thickness along the whole length of the fiber

Transverse cross sections every 1 inch along the clad fiber are examined to determine the uniformity of the spinel cladding along the fiber. In each cross section, the thickness of cladding is determined by the average of the cladding thickness calculated in 8 locations as shown in Figure 4-7, where each pair of diagonally opposed directions are connected with a broken red line.

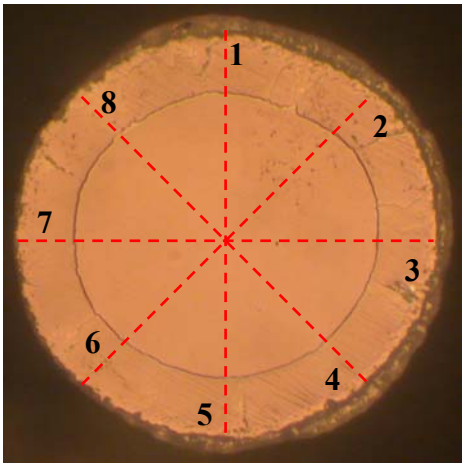

Figure 4-7

5. A smooth and crack free surface of coated fibers after drying, binder burnout, and the final firing

The surface of the coated fiber is examined after each stage of drying, binder burnout, and the final high-temperature firing. The procedures of examining the cracking in the cladding from the transverse cross section of the fiber are used here to examine the surface cracking on the surface of clad fibers.

Each clad sapphire fiber is ranked as either “best”, “good”, “fair”, “bad”, or “worst” in each of the criteria stated above. The ranking is then substituted into the existing software program to calculate the response table in which the effect of each individual factor is plotted.

The Taguchi method is a critically important method to clarify the effect of each factor in preparing the spinel clad sapphire samples. By adjusting each factor according to the results from the Taguchi array, clad samples with optimal optical and mechanical properties can be fabricated.